

11126

392351

270 p

NASA Contractor Report 195430

# NiAl and NiAl-Based Composites Directionally Solidified by a Containerless Zone Process

Steven M. Joslin  
*The University of Tennessee at Knoxville*  
*Knoxville, Tennessee*

February 1995

Prepared for  
Lewis Research Center  
Under Grant NAG3-876



National Aeronautics and  
Space Administration

(NASA-CR-195430) NiAl AND  
NiAl-BASED COMPOSITES DIRECTIONALLY  
SOLIDIFIED BY A CONTAINERLESS ZONE  
PROCESS Ph.D. Thesis (Tennessee  
Univ.) 264 p

N95-19792

Unclas

G3/26 0039662

**NiAl AND NiAl-BASED COMPOSITES DIRECTIONALLY SOLIDIFIED  
BY A CONTAINERLESS ZONE PROCESS**

A Dissertation  
Presented for the  
Doctor of Philosophy  
Degree

The University of Tennessee, Knoxville

Steven M. Joslin

December 18, 1994

## ACKNOWLEDGMENTS

I would like to thank my advisor, Dr. B.F. Oliver, for patience, support, and guidance that has reached beyond the scope of this research. I would also like to thank Dr. C.R. Brooks for his friendship, as well as many helpful discussions and meticulous reviews of this and other manuscripts. I also thank Dr. P.K. Liaw, Dr. A. Mathews, and Dr. J.H. Schneibel for their participation and many contributions.

I am very grateful for the support, both financial and technical, from NASA Lewis Research Center, Cleveland, OH. I am especially grateful to Dr. R.D. Noebe and Dr. J.D. Whittenberger for their contributions and guidance.

I would like to thank my co-workers, D.R. Johnson, Mrs. X.F. Chen, R. Reviere, and T.S. Newport for many interesting and helpful discussions concerning just about everything. I especially thank Mrs. Chen for her contributions regarding transmission electron microscopy; I am truly indebted to her. I also would like to express my appreciation to R. Johnson, D. Fielden, B.L. McGill, L. Smith, M. Ensor, M. Rogers, R. Bellamy, M. Neal, G. Jones, and T. Long. Without the support staff, this work would not have been possible.

## ABSTRACT

A containerless electromagnetically levitated zone (CELZ) process has been used to directionally solidify NiAl and NiAl-based composites. The CELZ processing results in single crystal NiAl (HP-NiAl) having higher purity than commercially pure NiAl grown by a modified Bridgman process (CP-NiAl). The mechanical properties, specifically fracture toughness and creep strength, of the HP-NiAl are superior to binary CP-NiAl and are used as a base-line for comparison with the composite materials subsequently studied.

Two-phase composite materials (NiAl-based eutectic alloys) show improvement in room temperature fracture toughness and 1200 to 1400 K creep strength over that of binary HP-NiAl. Metallic phase reinforcements produce the greatest improvement in fracture toughness, while intermetallic reinforcement produces the largest improvement in high temperature strength.

Three-phase eutectic alloys and composite materials were identified and directionally solidified with the intent to combine the improvements observed in the two-phase alloys into one alloy. The room temperature fracture toughness and high temperature strength (in air) serve as the basis for comparison between all of the alloys.

Finally, the composite materials are discussed in terms of dominant fracture mechanisms observed by fractography.

## TABLE OF CONTENTS

<b>PART I: LITERATURE REVIEW</b> .....	1
1. INTRODUCTION .....	2
2. PROPERTIES OF NICKEL ALUMINIDE .....	2
2.1 Physical Properties .....	2
2.2 Elastic Properties .....	10
2.3 Slip Systems .....	14
2.4 Yield Strength .....	16
2.5 Critical Resolved Shear Stress .....	19
2.6 Ductile-Brittle Transition Temperature .....	21
2.7 Ductility and Fracture Toughness .....	26
2.8 Creep Strength .....	27
3. ALLOYING ADDITIONS .....	31
3.1 Substitutional Alloy Additions .....	32
3.2 Interstitial Alloy Additions .....	39
3.3 Grain Refinement .....	42
3.4 Dislocation Density Effects .....	43
4. MULTI-PHASE ALLOYING .....	46
REFERENCES .....	48
<b>PART II: SCOPE AND PURPOSE</b> .....	56
<b>PART III: EXPERIMENTAL PROCEDURE</b> .....	62
1. INTRODUCTION .....	63
2. CONTAINERLESS ELECTROMAGNETICALLY LEVITATED ZONE PROCESS (CELZ) .....	68
3. BEND TESTING .....	73
4. MICROSCOPY .....	74
5. ELEVATED TEMPERATURE TESTING .....	76
REFERENCES .....	77
<b>PART IV: NIAL RESULTS</b> .....	79
1. INTRODUCTION .....	80

2. EXPERIMENTAL PROCEDURE .....	81
3. RESULTS .....	81
3.1 Processing .....	81
3.2 Microstructure .....	89
3.3 Purity .....	90
3.4 Yield Strength and CRSS .....	92
3.5 Fracture Toughness and Ductility .....	99
3.6 Creep Strength .....	101
4. SUMMARY .....	103
REFERENCES .....	105
<b>PART V: TWO-PHASE COMPOSITE ALLOYS</b> .....	<b>109</b>
1. LITERATURE REVIEW .....	110
1.1 Introduction .....	110
1.2 NiAl-9Mo .....	111
1.3 NiAl-40V .....	115
2. EXPERIMENTAL PROCEDURE .....	120
3. NiAl-Mo SYSTEM .....	126
3.1 Processing .....	127
3.2 Microstructure .....	129
3.3 TEM Observations .....	138
3.4 Mechanical Properties .....	138
3.4.1 Fracture Toughness .....	138
3.4.2 Elevated Temperature Properties .....	144
4. NiAl-40V .....	148
4.1 Processing .....	148
4.2 Microstructure .....	149
4.3 TEM Observations .....	153
4.4 Mechanical Properties .....	153
4.4.1 Fracture Toughness .....	153
4.4.2 Elevated Temperature Properties .....	155
5. DISCUSSION .....	156
5.1 Microstructure .....	156
5.2 Fracture Toughness .....	158
5.3 Elevated Temperature Properties .....	160
5.4 Comparison With Other Two-Phase Composites .....	161
6. SUMMARY .....	165
REFERENCES .....	168

<b>PART VI: POLYPHASE IN-SITU COMPOSITES</b> .....	171
1. INTRODUCTION .....	172
2. EXPERIMENTAL PROCEDURE .....	175
2.1 Processing .....	176
2.2 Microstructure and Mechanical Property Testing	177
2.3 Differential Thermal Analysis and X-Ray Diffraction Analysis	178
3. MICROSTRUCTURES .....	180
4. FRACTURE TOUGHNESS .....	185
5. ELEVATED TEMPERATURE PROPERTIES .....	186
6. DIFFERENTIAL THERMAL ANALYSIS (DTA) .....	189
7. SUMMARY .....	193
8. CAVEATS CONCERNING MICROSTRUCTURAL OBSERVATIONS ...	196
REFERENCES .....	198
<b>PART VII: FAILURE ANALYSIS</b> .....	200
1. INTRODUCTION .....	201
2. FRACTURE MECHANISMS .....	202
3. EXPERIMENTAL PROCEDURE .....	203
4. MICROSTRUCTURAL OBSERVATIONS .....	206
4.1 NiAl-Mo Alloys .....	206
4.1.1 NiAl(0.1Zr)-9Mo Eutectic .....	206
4.1.2 NiAl-9Mo Eutectic .....	211
4.1.3 NiAl(0.1Zr)-12Mo and NiAl(0.1Zr)-15Mo	213
4.1.4 Summary of NiAl-Mo Alloys .....	215
4.2 NiAl-40V Eutectic .....	216
4.3 NiAl-15Zr-15V .....	223
4.4 NiAl-12Nb-36V .....	226
4.5 NiAl-Nb-Mo Alloys .....	229
4.5.1 NiAl-13.6Nb-18Mo .....	229
4.5.2 NiAl-5Nb-10Mo .....	231
4.5.3 NiAl-3Nb-10Mo .....	234
5. BRIDGING CONTRIBUTION TO FRACTURE TOUGHNESS .....	236
6. DISCUSSION .....	243

REFERENCES .....	246
VITA .....	249



## LIST OF FIGURES

FIGURE		PAGE
1.	The CsCl (B2) crystal structure of $\beta$ -NiAl and possible slip vectors on {110} planes. ....	3
2.	The Ni-Al phase diagram in atomic percent. ....	5
3.	Variation in lattice parameter with composition for NiAl. ....	5
4.	Effective diffusion coefficient versus atomic percent nickel. ....	8
5.	Microalloying affect on room temperature ductility of NiAl <110> and <111> single crystals. ....	9
6.	Relationship between hardening rate and alloying element size. ....	9
7.	Elastic constants of NiAl as a function of temperature, composition, and orientation. ....	12
8.	Fractional density of dislocations in "hard" single crystal Ni-48Al a/o after deformation as a function of temperature. ....	15
9.	Yield stress as a function of temperature. ....	17
10.	Critical resolved shear stress for single and polycrystalline NiAl. ....	22
11.	The ductile-brittle transition temperature for hard and soft oriented NiAl single crystals. ....	23
12.	The steady-state flow stress for NiAl as a function of strain rate and temperature. ....	25
13.	Typical creep data for NiAl, showing power law behavior at strain rates above $10^{-8}$ . ....	28
14.	The effects of various elements on the mechanical properties of NiAl. ....	35
15.	Arrhenius representation of the yield stress for polycrystalline NiAl and tensile ductility as a function of inverse temperature. ....	37
16.	Diffusion coefficient as a function of Fe content in NiAl. ....	38

17.	Mobile dislocation density -vs- fracture behavior in NiAl. ....	45
18.	Schematic illustration of a modified Bridgman apparatus. ....	64
19.	Composition of the freezing solid as a function of distance traveled under normal and zone melting conditions. ....	66
20.	Process control schematic. ....	69
21.	Melt record for NiAl-15Zr-15V. ....	71
22.	Typical melt record for binary HP-NiAl. ....	82
23.	As-processed single crystal HP-NiAl grown from a polycrystalline precursor, orientation near <123>. ....	84
24.	As-processed single crystal HP-NiAl grown from a <110> CP-NiAl seed crystal. ....	84
25.	Compressive stress-strain curves for HP-NiAl, CP-NiAl, and NiAl-0.2Mo single crystals. ....	93
26.	Yield strength in compression as a function of temperature for <001> HP-NiAl. ....	98
27.	Fracture toughness of NiAl single crystals as a function of orientation. ....	102
28.	The Ni-Al-Mo ternary isotherm at 1073 K. ....	113
29.	Room temperature fracture toughness for NiAl-Mo alloys. ....	116
30.	Ni-Al-V phase diagrams. ....	118
31.	Typical melt record for NiAl(0.1Zr)-9Mo. ....	121
32.	Typical melt record for NiAl-40V. ....	122
33.	As-processed ingots of NiAl-40V and NiAl(0.1Zr)-9Mo. ....	124
34.	As-processed microstructure of NiAl-9Mo, transverse section, unetched. ....	130
35.	As-processed microstructure of NiAl(0.1Zr)-9Mo, transverse section, unetched. ....	130

36.	As-cast microstructure of NiAl(0.1Zr)-9Mo precursor ingot, transverse section, unetched. . .	131
37.	As-processed microstructure of NiAl-9Mo showing rings of variable rod spacing and density due to variation in growth conditions. ....	131
38.	Schematic illustration of the development of the ring pattern observed in NiAl-9Mo ingots. ...	132
39.	Deeply etched NiAl(0.1Zr)-9Mo ingot. ....	134
40.	Longitudinal microstructure of NiAl(0.1Zr)-9Mo.	134
41.	Longitudinal section of NiAl(0.1Zr)-9Mo showing severe banding. ....	135
42.	Microstructure of eutectic regions in NiAl(0.1Zr)-12Mo and NiAl(0.1Zr)-15Mo, transverse sections, unetched. ....	137
43.	TEM micrograph and diffraction pattern of NiAl-9Mo. ....	139
44.	TEM micrographs of NiAl(0.1Zr)-9Mo taken near the fracture surface of a bend bar. ....	139
45.	Microstructure at the root of the notch in NiAl(0.1Zr)-12Mo and NiAl(0.1Zr)-15Mo bend bars.	142
46.	Compressive yield strength as a function of temperature for NiAl-based composites. ....	145
47.	Compressive flow stress-strain rate behavior for several NiAl-based composites at 1300 K. ....	145
48.	Typical transverse microstructure of NiAl-40V showing cellular growth. ....	150
49.	Typical longitudinal microstructure of NiAl-40V showing cellular growth front. ....	150
50.	Longitudinal microstructure of NiAl-40V showing minor banding and severe banding due to changes in the local growth conditions. ....	151
51.	Longitudinal section of NiAl-40V showing precipitation of NiAl within large single phase V regions. ....	152

52.	TEM micrograph and diffraction pattern of NiAl-40V. ....	154
53.	Transverse microstructures of NiAl-34Cr and NiAl-15.5Ta. ....	162
54.	Performance plot of the two-phase eutectic alloys. ....	163
55.	The specific performance plot showing the combination of density compensated 1300 K strength and room temperature fracture toughness. ....	164
56.	The crystal structure of Ni <sub>2</sub> AlZr, Heusler-type phase. ....	173
57.	Trnasverse microstructures of NiAl-15Zr-15V and NiAl-12Nb-36V. ....	181
58.	Schematic phase diagrams for the Ni-Al-Zr-V and NiAl-Nb-V systems. ....	181
59.	Phase boundary angles in NiAl12Nb-36V indicating the similarity of the surface energies between the three phases. ....	183
60.	The 1300 K compressive strength as a function of strain rate for three-phase alloys. ....	187
61.	Results of DTA for NiAl-15Zr-15V. ....	190
62.	The Zr-V phase diagram. ....	190
63.	The Ni-Al-Zr isotherm at 1073 K. ....	192
64.	Performance plot and specific performance plot for three-phase alloys. ....	195
65.	Typical transverse microstructure of NiAl(0.1Zr)-9Mo showing dislocations in the NiAl matrix. ....	207
66.	The fracture surface of NiAl(0.1Zr)-9Mo. ....	209
67.	The fracture surface of NiAl-9Mo. ....	212
68.	Failure by combined axial extension and shearing of the Mo rods. ....	214
69.	TEM As-processed NiAl-40V. ....	217

70.	TEM Uniform dislocation tangles in NiAl and coarse slip bands in V in NiAl-40V after bend testing. ....	218
71.	Types of dislocation distribution in the V-matrix of NiAl-40V. ....	220
72.	TEM Micrographs taken near the fracture surface of a NiAl-40V bend specimen. ....	220
73.	Secondary cracking in NiAl-40V observed on the surface of as-polished bend specimens showing evidence of crack bridging and crack renucleation. ....	221
74.	Fractographs taken from NiAl-40V bend specimens.	224
75.	The fracture surface of NiAl-15Zr-15V. ....	225
76.	The fracture surface of NiAl-12Nb-36V. ....	227
77.	Fracture surface of NiAl-13.6Nb-18Mo. ....	230
78.	Surface of NiAl-13.6Nb-18Mo bend specimen. ....	232
79.	Low magnification micrograph showing secondary cracking in NiAl-13.6Nb-18Mo. ....	232
80.	Secondary crack at the surface of a NiAl-5Nb-10Mo bend specimen. ....	233
81.	The fracture surface of NiAl-5Nb-10Mo. ....	235
82.	Fracture surface of NiAl-3Nb-10Mo. ....	235

## LIST OF TABLES

TABLE	PAGE
1. Elastic constants for NiAl at room temperature. ..	11
2. $\langle 001 \rangle \{110\}$ CRSS for commercial purity NiAl. ....	20
3. Fracture toughness of CP-NiAl. ....	42
4. Purity levels in HP and CP NiAl. ....	91
5. Yield strength data for binary NiAl at 300 K. ....	94
6. Room temperature CRSS data (MPa) for NiAl. ....	96
7. Room temperature fracture toughness. ....	100
8. Summary of mechanical property data for binary eutectic alloys. ....	114
9. Growth conditions for two-phase eutectic alloys.	120
10. Interstitial impurity content. ....	136
11. Results of screening tests for binary eutectics.	140
12. Summary of 1300 K creep strength. ....	147
13. Summary of two-phase alloys. ....	163
14. Processing conditions for three-phase alloys. ...	176
15. Volume fraction of phases for polyphase alloys.	184
16. Room temperature fracture toughness, $K_{Ic}$ . ....	185
17. 1300 K true compressive yield strength at 1% true strain. ....	188
18. Parameters used in the small scale bridging (SSB) model. ....	238
19. SSB model results using data in Table 18. ....	241

PRECEDING PAGE BLANK NOT FILMED

1. The first part of the paper is a general introduction to the topic of the study. It discusses the importance of the research and the objectives of the study.

## **PART I: LITERATURE REVIEW**

The literature review in this paper is divided into two main sections. The first section discusses the theoretical background of the study, while the second section discusses the empirical research that has been conducted in this area. The theoretical background section starts with a discussion of the basic concepts of the study, such as the definition of the variables and the relationships between them. It then moves on to a discussion of the different theories that have been developed to explain the phenomena being studied. The empirical research section starts with a discussion of the different methods that have been used to study the phenomenon, and then moves on to a discussion of the results of the different studies. The results are then compared and contrasted with the theoretical predictions, and the implications of the findings are discussed.

## 1. INTRODUCTION

Differences between the various approaches to property enhancement of binary NiAl are presented in this literature review. The primary advantages of directional solidification, purity, and properties associated with fracture toughness, ductility, and creep strength are emphasized. A comprehensive review of all physical and mechanical properties of NiAl and binary NiAl-based eutectics is not intended.

## 2. PROPERTIES OF NICKEL ALUMINIDE

### 2.1 Physical Properties

Nickel aluminide is a  $3/2$  ordered  $\beta$  electron compound with a B2, CsCl-type crystal structure [1-3]. This is an ordered body centered cubic structure, Fig. 1, which may be considered as two interpenetrating simple cubic lattices. Aluminum occupies one sublattice and nickel the other. Recent investigation indicates that stoichiometric nickel aluminide melts congruently at 1955 K (1682°C) [4]. Slight deviations in composition and steep liquidus slopes are believed to be responsible for the lower value of 1911 K (1638°C) most often reported. Stability of the NiAl phase is shown not only by the high melting temperature, but a



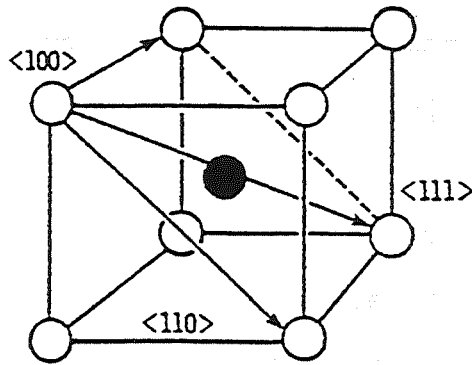


**Figure 1:** The CsCl (B2) crystal structure of  $\beta$ -NiAl and possible slip vectors on  $\{110\}$  planes [1].

high heat of formation as well. In fact, NiAl has the most exothermic heat of formation for any phase in the Ni-Al system, -72 kJ/mole [5]. A high ordering energy [1,6] may limit the possible slip systems. Its density is 5.95 g/cm<sup>3</sup> [1], approximately two thirds that of nickel-base superalloys.

Binary  $\beta$ -NiAl has a wide phase field ranging from 45.0 to 58.5 atomic percent Ni at room temperature (Fig. 2) [7]. The lattice parameter of binary NiAl peaks at 50 at/o aluminum, 2.886 Å [6,8,9], and depends strongly on stoichiometry (Fig. 3) [9]. Off-stoichiometric compositions are accommodated by incorporation of constitutional defects in the crystal lattice. Excess nickel substitutes for aluminum on the aluminum sublattice, but excess aluminum generates vacancies in the nickel sublattice because aluminum does not enter the nickel sublattice [6,10-12].

The highly symmetric and open crystal structure of  $\beta$ -NiAl increases the potential for successful property control through alloy additions compared to other intermetallic phases with more complicated crystal structures [1]. However, the open crystal structure may also increase the susceptibility to interstitial impurities and decrease the creep strength since diffusion rates are generally higher in open structures than for close packed structures [13,14].

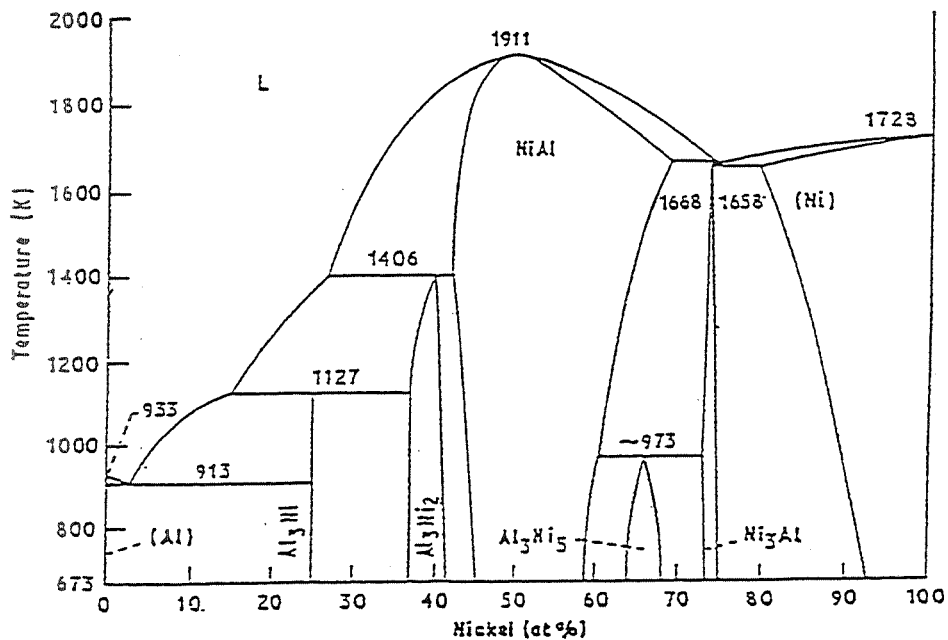


Figure 2: The Ni-Al phase diagram in atomic percent [7].

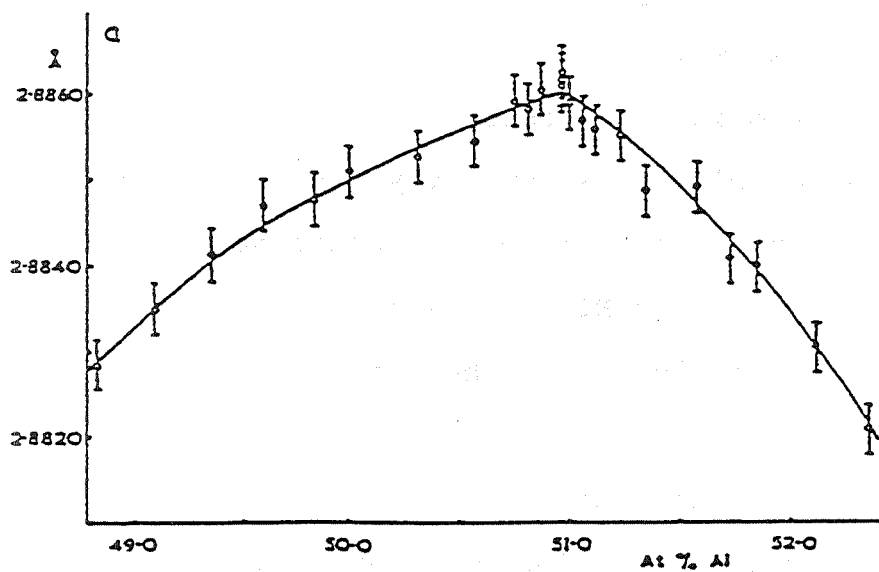


Figure 3: Variation of lattice parameter with composition for NiAl [9].

The thermal conductivity of approximately 75 W/m-K is 4 to 8 times that of nickel-base superalloys [1]. This fact makes NiAl very attractive for applications where heat dissipation is important. The coefficient of thermal expansion (CTE) is a strong function of temperature, and for temperatures ranging from 300 K to 1300 K follows the equation [9]:

$$\alpha_{\text{NiAl}} \text{ (K}^{-1}\text{)} = 1.16026 \times 10^{-5} + 4.08531 \times 10^{-9} T - 1.58368 \times 10^{-12} T^2 + 4.18374 \times 10^{-16} T^3$$

where T is in K. The CTE is very similar to that of nickel-based superalloys, but not to that of many reinforcement materials [9].

The oxidation resistance of  $\beta$ -NiAl is excellent. Nickel aluminide is currently used as a coating for nickel-based superalloys in turbine blade applications. Additions of 0.1 a/o Zr or Hf improve the cyclic oxidation resistance of  $\beta$ -NiAl by improving the adherence of the aluminum oxide film [15,16].

Purity and stoichiometry have often been ignored in alloying investigations. However, it is known experimentally that both can significantly affect the mechanical properties of NiAl. For example, substitutional impurities or alloying additions can alter the effective

Ni:Al ratio, generating point defects [9,10] which increase the effective diffusion coefficient and therefore the creep rate (Fig. 4) [9,17]. Furthermore, at low temperatures these defects create dislocation atmospheres which increase the yield strength and contribute to brittle behavior [9,17]. Thus, the ductility, ductile-brittle transition temperature (DBTT), and creep strength are sensitive functions of structure, alloy composition, stoichiometry, impurity content, and lattice defects [1,17], all of which are affected by the thermal and chemical environment of any processing technique.

To emphasize the sensitivity and complex nature of purity and stoichiometry effects, brief examples concerning substitutional and interstitial alloying are given here. More detailed discussion is presented in later chapters. Low levels of Mo, Fe, and Ga have been shown to increase the room temperature ductility of  $\langle 110 \rangle$  and  $\langle 111 \rangle$  single crystals, Fig. 5 [18]. The increase in ductility has been attributed to gettering of interstitial impurities [18]. However, at levels above 0.5 a/o the effect is lost.

Interstitial impurities can be potent strengtheners in NiAl, Fig. 6 [9]. The effects of specific interstitial impurities are currently under investigation. Unfortunately, the level of purity has not always been reported, making the isolation of purity related effects on

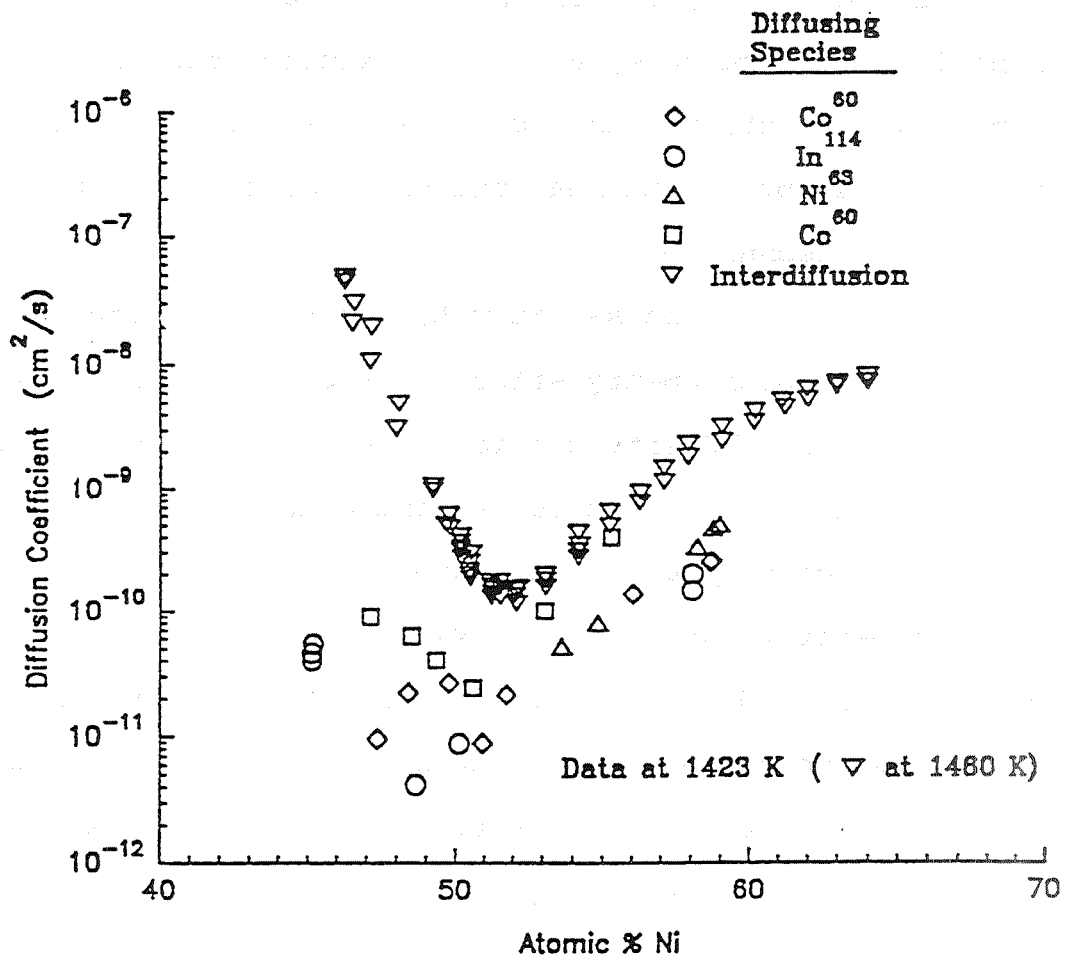


**Figure 4:** Effective diffusion coefficient versus atomic percent nickel [17].

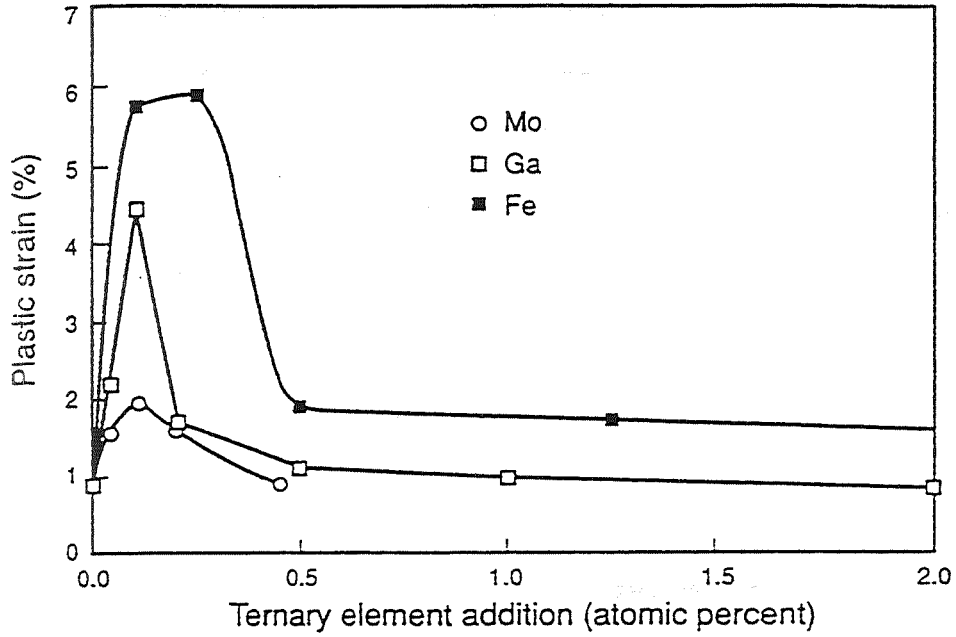


Figure 5: Microalloying affect on room temperature ductility of NiAl <110> and <111> single crystals [18].

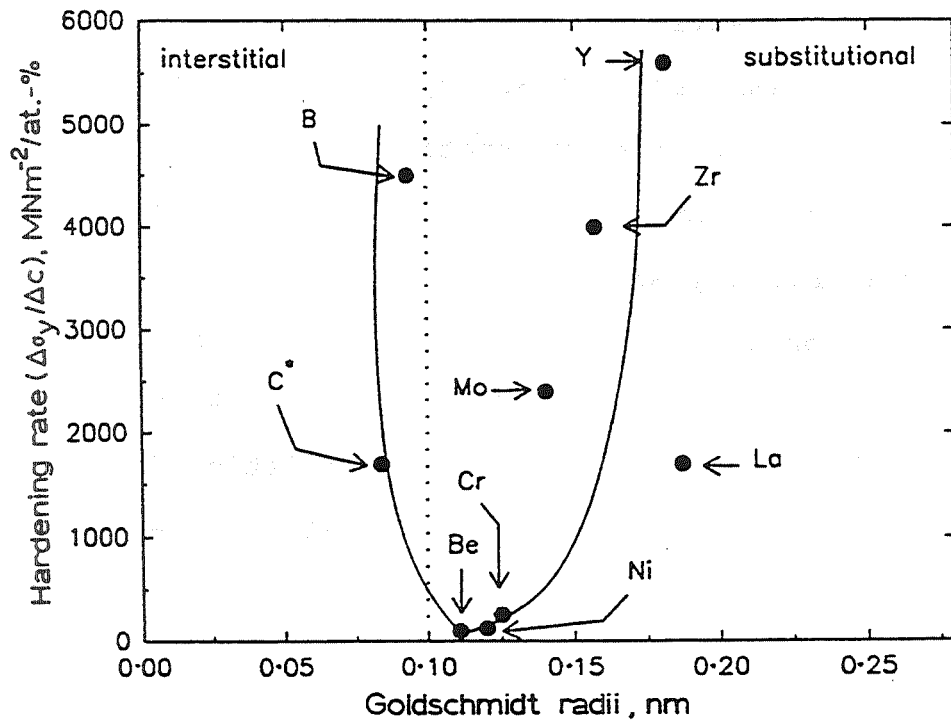


Figure 6: Relationship between hardening rate and alloying element size [9].

mechanical properties from existing literature very difficult. Intentional additions of the interstitial elements B and C provide a 30% increase in yield strength at only 30 wppm (parts per million by weight) [19]. At levels greater than 100 wppm, the increase in yield strength is more than 50%. Levels over 300 wppm have been shown to increase the ductile brittle transition temperature [19].

## 2.2 Elastic Properties

Elastic constants have been determined for single crystal binary NiAl [20-22] and summarized by several authors: Rusovic and Warlimont [23]; Miracle[24]; and Noebe, Bowman, and Nathal [9]. The values in Table 1 depend on crystallographic orientation, temperature, stoichiometry, and point defect concentration. Hence, the cooling rate and thermal history are important factors for interpretation and comparison of the results, but they are not always reported. The anisotropy,  $A=2C_{44}/(C_{11}-C_{12})$ , of NiAl depends on both stoichiometry and temperature. Deviation from stoichiometry gives values of A ranging from 1.85 for Ni-55Al to 5.67 for Ni-45Al [23,24]. The anisotropy factor decreases slightly with increasing temperature with values ranging from 3.3 at room temperature to 2.94 at 873 K [21,23].



Young's modulus shows a linear dependence on temperature [21,25], but is relatively insensitive to minor alloying additions[25]. The temperature dependence of Young's modulus follows the equation:

$$E=204.9-0.041(T)$$

where T is in K and E is in GPa [23]. For polycrystalline NiAl, Young's modulus shows a strong dependence on processing technique by virtue of crystallographic textures associated with the various processing conditions. For example, extruded NiAl shows a higher modulus than hot pressed or cast and homogenized ingots, probably due to a <111> preferred orientation [26,27]. Values of Young's modulus (E), Poisson's ratio ( $\nu$ ), compliance ( $C_{ij}$ ) and the shear modulus (G) are given in Table 1 and Figure 7.

**TABLE 1: Elastic constants for NiAl at room temperature**

PROPERTY	ORIENTATION	VALUE (GPa)	REF.
E	<100>	94.46	21
E	<110>	184.51	21
E	<111>	270.43	21
G	<100>	112.1	21
G	<110>	52.5	21
G	<111>	44.5	21
$C_{11}$	-	197	23
$C_{12}$	-	102	23
$C_{44}$	-	88	23
$\nu$	-	0.313	28

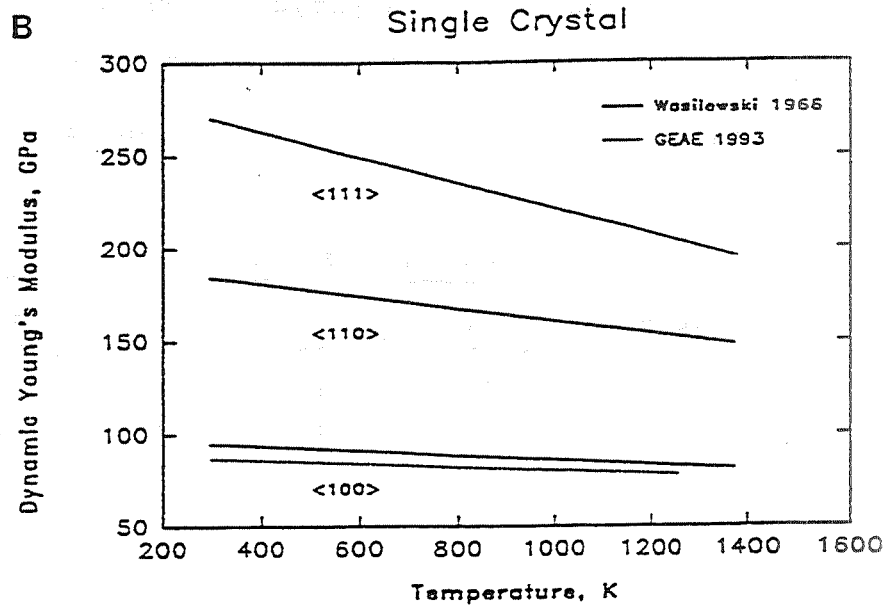
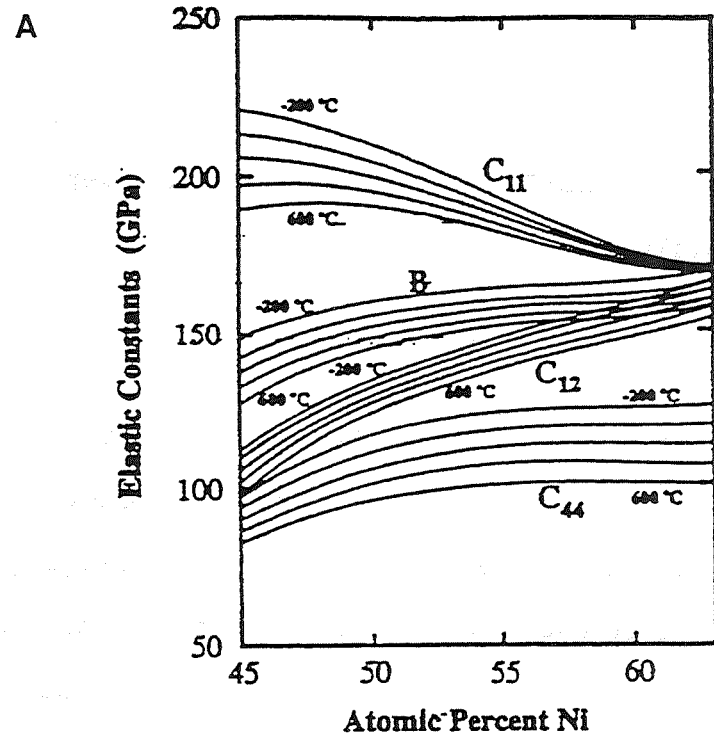


Figure 7: Elastic constants of NiAl as a function of temperature, composition, and orientation [23,24].  
 a) Elastic constants. b) Young's modulus for  $\langle 111 \rangle$ ,  $\langle 110 \rangle$ , and  $\langle 100 \rangle$  single crystal NiAl.  
 c) Young's modulus for polycrystalline NiAl.

C

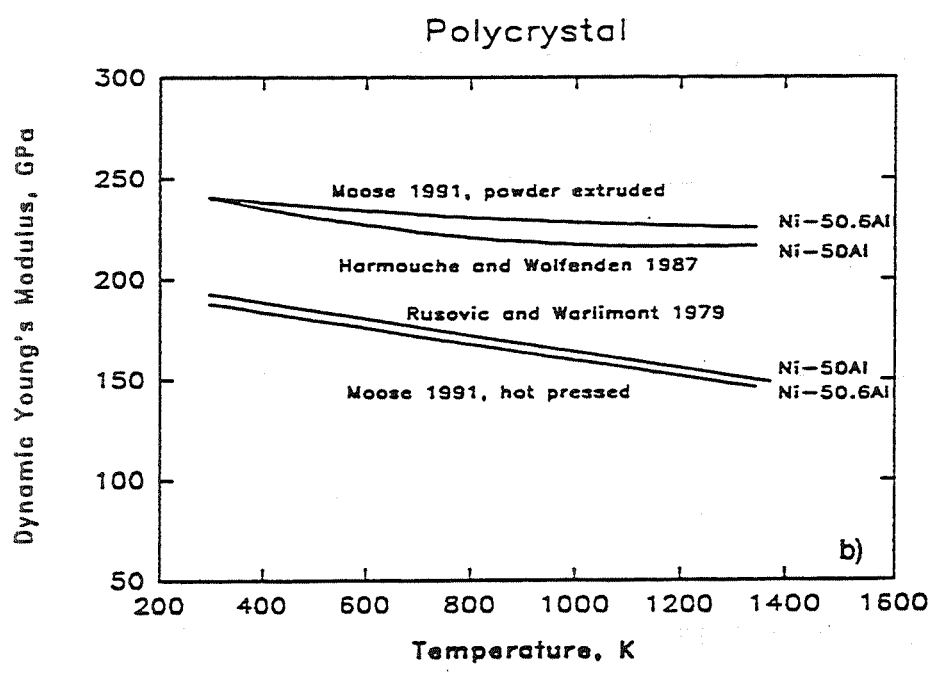


Figure 7 continued.

### 2.3 Slip Systems

Nickel aluminide does not meet the Von Mises criterion, falling short of five independent slip systems required for a generalized change of shape. At room temperature, the active slip system is predominantly  $\langle 001 \rangle \{110\}$  for polycrystals and nearly all single crystal loading conditions, with a very small percentage of  $\langle 001 \rangle \{100\}$  dislocations observed by some investigators [9,29]. Due to a high Schmid factor, the dominant slip system for  $[110]$  oriented crystals is  $\langle 001 \rangle \{100\}$  [30-32]. However, the major exception is  $\langle 001 \rangle$ -oriented single crystals where  $\langle 111 \rangle \{112\}$  dislocations have been observed at low and intermediate temperatures, Figure 8 [9,33]. At elevated temperatures a combination of  $\langle 100 \rangle$  and  $\langle 110 \rangle$  dislocations are observed which move by non-conservative motion [9,29]. Cross slip has been observed on orthogonal  $\{110\}$  planes [30,33]. In  $[110]$  and  $[112]$  oriented single crystals, duplex cube slip has been observed [30,31,34]. It should be emphasized that non- $\langle 001 \rangle$  dislocations result from testing at low temperatures under special conditions where the Schmid factor on the  $\{110\} \langle 001 \rangle$  systems is extremely low [9,29].

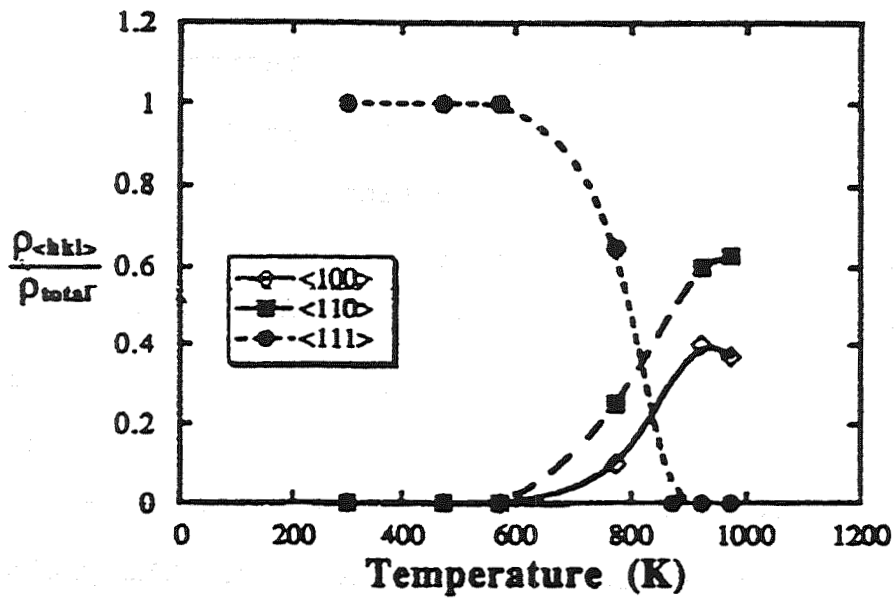
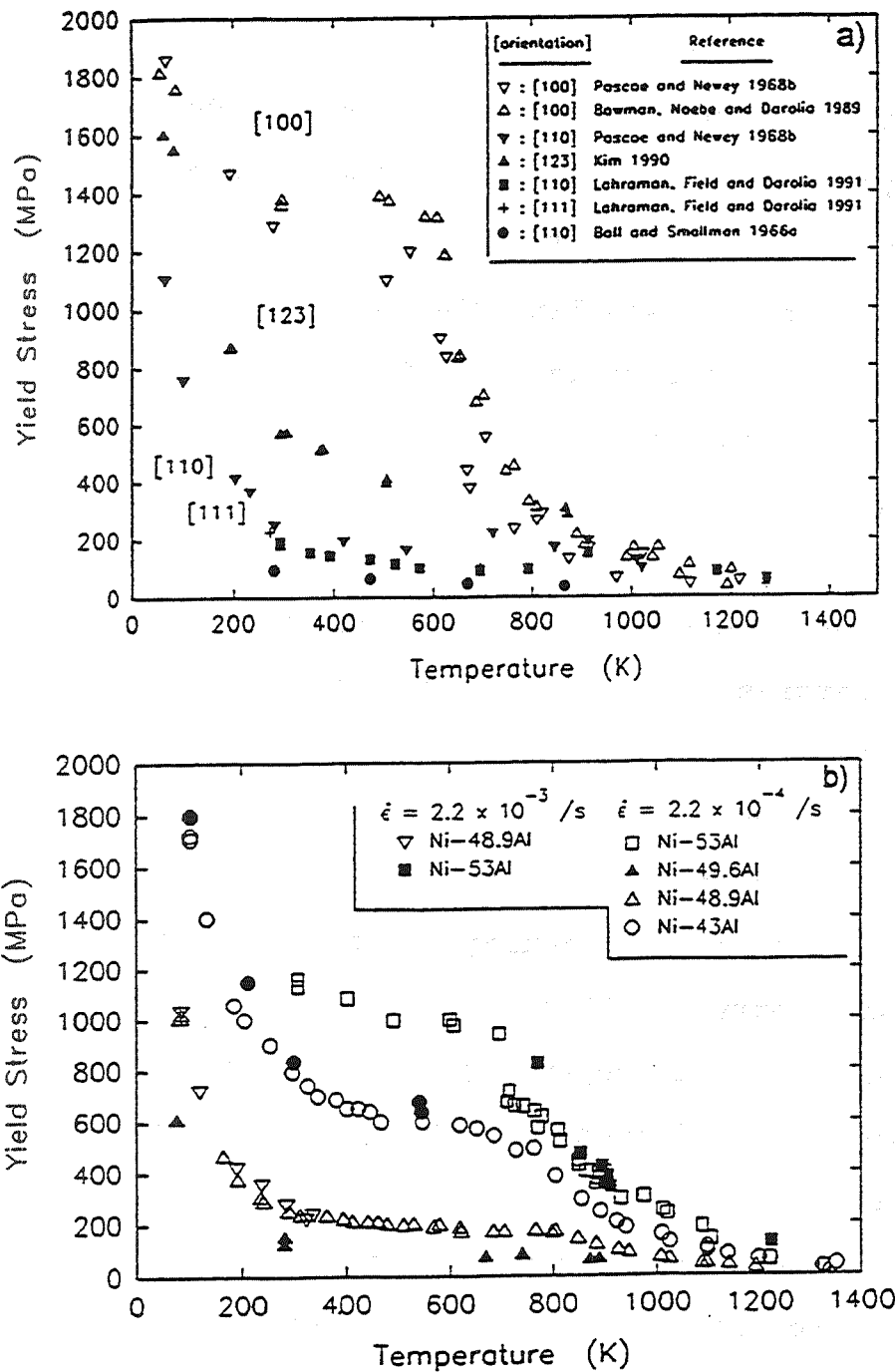


Figure 8: Fractional density of dislocations in "hard" single crystal Ni-48Al a/o after deformation as a function of temperature [9].

## 2.4 Yield Strength

The yield strength of  $\beta$ -NiAl at room temperature is generally measured in compression due to its low ductility. Results of compressive yield strength tests indicate that the plastic behavior of  $\beta$ -NiAl is highly sensitive to stoichiometry, impurity content, grain size, cooling rate (thermal vacancies), and specimen fabrication [1,6,10,14,20,35,36]. The temperature dependence is similar to that of BCC metals. An orientation dependence is clearly evident in Fig. 9. For [001] crystals the yield strength shows extreme orientation sensitivity at low absolute temperatures, a plateau of only slight dependence at intermediate temperatures, followed by another region of sensitivity at elevated temperatures [37]. The drop in yield strength near 600 K is associated with a change in the slip system in conjunction with the activation of non-conservative deformation mechanisms. The yield strength of stoichiometric  $\langle 110 \rangle$ -oriented single crystals is approximately 165-190 MPa [1,19,20,35,38,39] and for  $\langle 100 \rangle$ -oriented single crystals it is 980-1400 MPa [20,40].

Based on single crystal properties, crystallographic texture and substructure are expected to significantly contribute to the flow properties of polycrystalline NiAl [41]. However, a recent study by George and Liu [19] suggests that substructure may not be crucial to the limited



**Figure 9:** Yield stress as a function of temperature. For a) single crystal and b) polycrystalline NiAl as a function of strain rate and stoichiometry [32,37].

tensile ductility. They report a tensile yield strength of 154 MPa and ductility of 2.2% for extruded (9:1) and fully recrystallized stoichiometric NiAl with a grain size of approximately  $30 \pm 5 \mu\text{m}$ .

For polycrystalline NiAl of near stoichiometric composition, the yield strength is similar to that of soft oriented single crystals. For significantly off-stoichiometric compositions it is on the order of hard oriented single crystals, even though polycrystalline deformation occurs by  $\langle 001 \rangle$  slip. However, at elevated temperatures, 1000 K and above, the yield strength is essentially the same for soft and hard oriented single crystals and polycrystalline NiAl due to the activation of bulk diffusional processes [37].

The average hardening rates for variations in stoichiometry or alloy content are greater than 100 MPa/at%, the actual value depending on the alloying element [9,19]. While any significant deviation from stoichiometry results in considerable hardening, the difference in constitutional defects between Ni- and Al-rich NiAl provides different hardening rates. For Ni-rich material, the hardening rate is 120 MPa/at%, while for Al-rich NiAl it is nearly 350 MPa/at% [19]. Hence, the Ni vacancies required to accommodate excess Al are more effective at pinning dislocations than anti-site defects. The effect of non-



stoichiometry is negligible at temperatures near 1000 K [37], and stoichiometric NiAl becomes the stronger of the two compositions in the diffusion dependent temperature range, above 1000 K [24,33,37,42].

Thermal vacancies can be quenched into the microstructure by rapid cooling from elevated temperature. Their effect is similar to that of constitutional vacancies present in Al-rich NiAl. A 50-fold increase in cooling rate from temperatures above 1000 K results in an increase of nearly 30% in the compressive yield strength for stoichiometric polycrystalline NiAl [37]. Single crystal NiAl exhibits a similar dependence on cooling rate [43].

## **2.5 Critical Resolved Shear Stress (CRSS)**

The critical resolved shear stress has been determined by resolution of the flow stress onto either the observed slip system or an assumed slip system, usually  $\langle 100 \rangle \{110\}$ , for single crystal specimens. Experimentally determined values are listed in Table 2. The CRSS is significantly affected by substitutional and interstitial impurities, strain rate, and even small deviations from stoichiometry. Comparisons between published values are complicated by incomplete documentation of these factors. However, Field et al. [31] measured the CRSS for  $\langle 111 \rangle$  and  $\langle 110 \rangle$  oriented

crystals cut from the same homogenized casting, effectively eliminating deviations in composition and purity as variables. Slip was assumed to occur on  $\langle 001 \rangle \{100\}$  for the  $\langle 110 \rangle$  oriented crystal, which gives a CRSS of  $109 \text{ MN/m}^2$ ; an erroneous value of  $77 \text{ MN/m}^2$  results if the operative slip system is assumed to be  $\langle 100 \rangle \{110\}$ . Using the observed  $\langle 001 \rangle \{110\}$  slip system for the  $\langle 111 \rangle$  oriented crystal gives a value of  $124 \text{ MN/m}^2$ . In contrast, Wasilewski determined the CRSS for  $\langle 001 \rangle \{110\}$  slip in a  $\langle 111 \rangle$  oriented crystal to be  $60\text{-}100 \text{ MN/m}^2$  [21]. Values of CRSS are therefore a good indication of the relative purity between stoichiometric specimens.

**Table 2:  $\langle 001 \rangle \{110\}$  CRSS of commercial purity NiAl**

CRSS (MPa)	CONDITION	REF.
109	$\langle 110 \rangle$ crystal	[31]
124	$\langle 111 \rangle$ crystal	[31]
60-100	$\langle 111 \rangle$ crystal	[21]
$105.9 \pm 9.5$	as-processed*	[43]
$79.4 \pm 4.0$	1000 K(2hr)+FC	[43]
82.4	1000 K(2hr)+WQ	[43]

\* Bridgman-type process (commercial purity)

Temperature effects have been modeled equally well by two equations [24]:

$$\tau = Ae^{-Q/RT} \quad [40,44]$$

and the empirical equation

$$\tau = Ae^{(-BT)} \quad [45,46]$$

where  $\tau$  is the flow stress or critical resolved shear stress,  $Q$  is an activation energy and  $A$  and  $B$  are constants. Since the crystallographic loading conditions determine the active slip system and the active slip system is known to differ between hard and soft oriented crystals, their response to temperature changes must be considered separately. Hence the critical resolved shear stress for soft and hard single crystals shown in Figure 10 [24] exhibits a different temperature dependence. Hard oriented crystals show a sharp change in slope near 600 K. For hard orientations, slip occurs predominantly by glide of  $a\langle 111 \rangle$  dislocations below 600 K, but changes to  $a\langle 110 \rangle$  with increasing temperature. As expected the CRSS is essentially the same for  $a\langle 111 \rangle$  and  $a\langle 110 \rangle$  at 600 K, but with increasing temperature the value drops more quickly for  $\langle 110 \rangle$  slip.

## 2.6 Ductile-Brittle Transition Temperature (DBTT)

The DBTT depends strongly on strain rate, test specimen orientation, composition, and purity of the material [1,9,17,20,47]. Grain size has a relatively minor affect on the DBTT [37]. Typically, the DBTT is around 623 K (350°C) to 673 K (400°C) for  $\langle 100 \rangle$ -oriented single crystals [1] and 473 K (200°C) for soft-oriented crystals (Fig. 11) [48,49]. For  $\langle 001 \rangle$ -crystals, the DBTT occurs in the temperature range

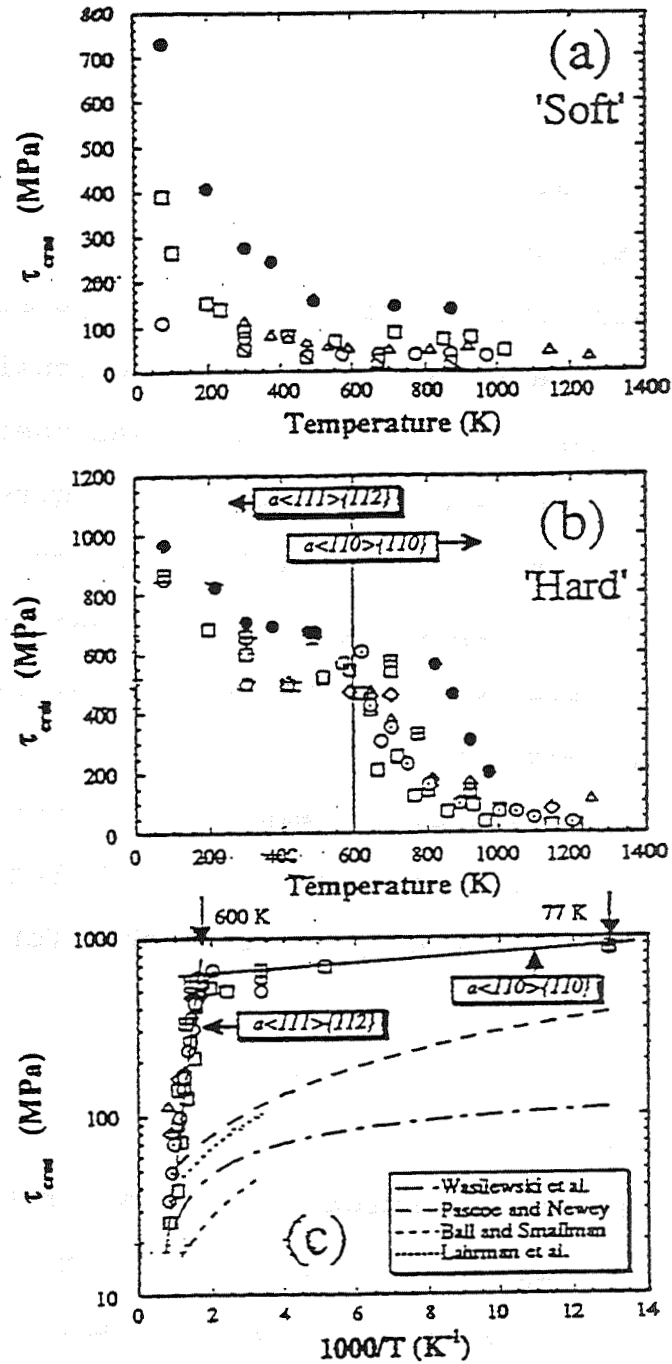


**Figure 10:** The critical resolved shear stress for single and polycrystalline NiAl. a)  $a\langle 100 \rangle$  slip in 'soft' crystals, b)  $a\langle 111 \rangle\{112\}$  and  $a\langle 110 \rangle\{110\}$  slip in 'hard' crystals, and c) the CRSS -vs-  $1000/T$  for nominally stoichiometric 'soft' (dashed curves) and 'hard' crystals, after Miracle [24].

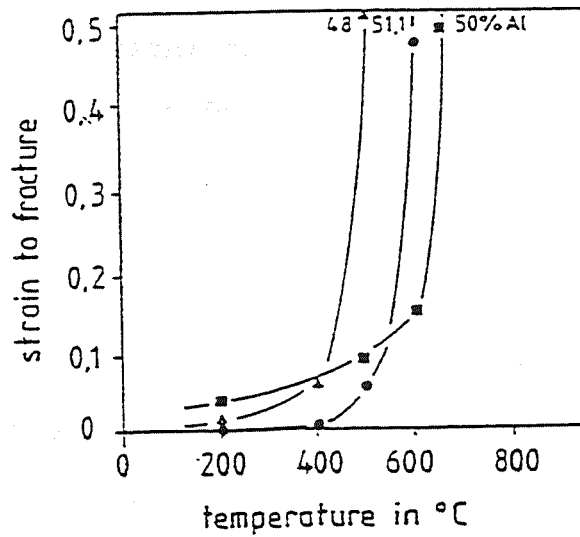
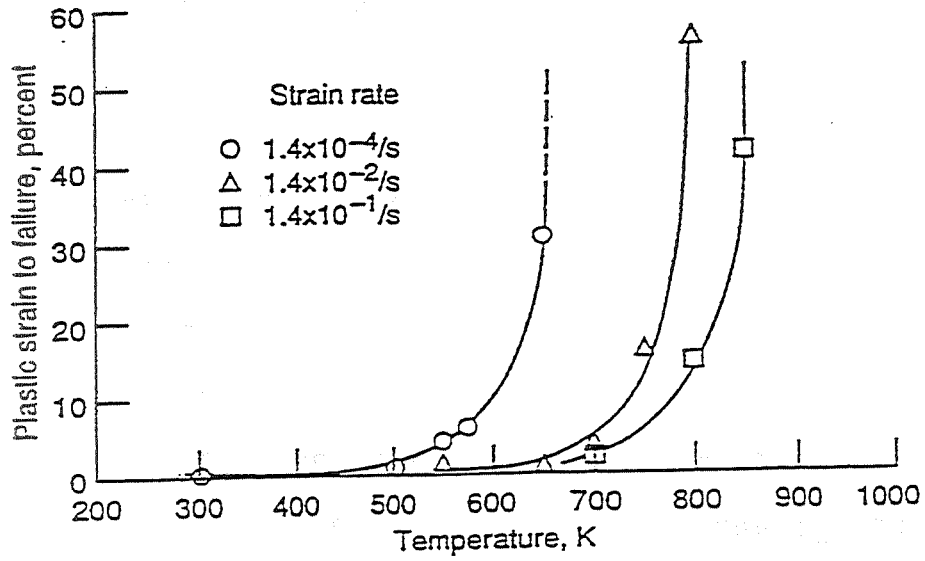


Figure 11: The ductile-brittle transition temperature for hard and soft oriented NiAl single crystals [9,14].

where the deformation mechanism changes from slip by  $\langle 111 \rangle$  to non-conservative motion of  $\langle 001 \rangle$  and  $\langle 110 \rangle$  type dislocations [50-52]. Deviation from stoichiometry increases the DBTT. For example, the DBTT of Ni-40Al  $\langle 001 \rangle$ -oriented crystals occurs at 1000 K [29], but for polycrystalline NiAl, it can occur as low as 550 K [37].

The change in fracture behavior at the DBTT is generally attributed to a change in either the dominant slip system or the activation of non-conservative mechanisms. The low DBTT's observed for soft oriented single crystals ( $0.28 T_m$ ) and some polycrystalline specimens cast doubt that bulk diffusional processes can account for the transition. Noebe [37] has identified an intermediate temperature regime between dislocation glide and bulk diffusion (creep) dominated deformation regimes, Fig. 12. In this intermediate regime, dislocation climb occurs by short circuit diffusion [53,54], in the vicinity of the grain boundaries only. Dislocation glide dominates the grain interiors below 1000 K. However, the resulting increase in grain boundary compatibility gives rise to increased ductility and toughness. Hence, the DBTT occurs at the onset of short circuit diffusion at the grain boundaries with an activation energy of 236 kJ/mole, slightly less than 314 kJ/mole observed in the high temperature regime [55], and a well defined stress exponent of  $16.2 \pm 1.3$ . In-situ

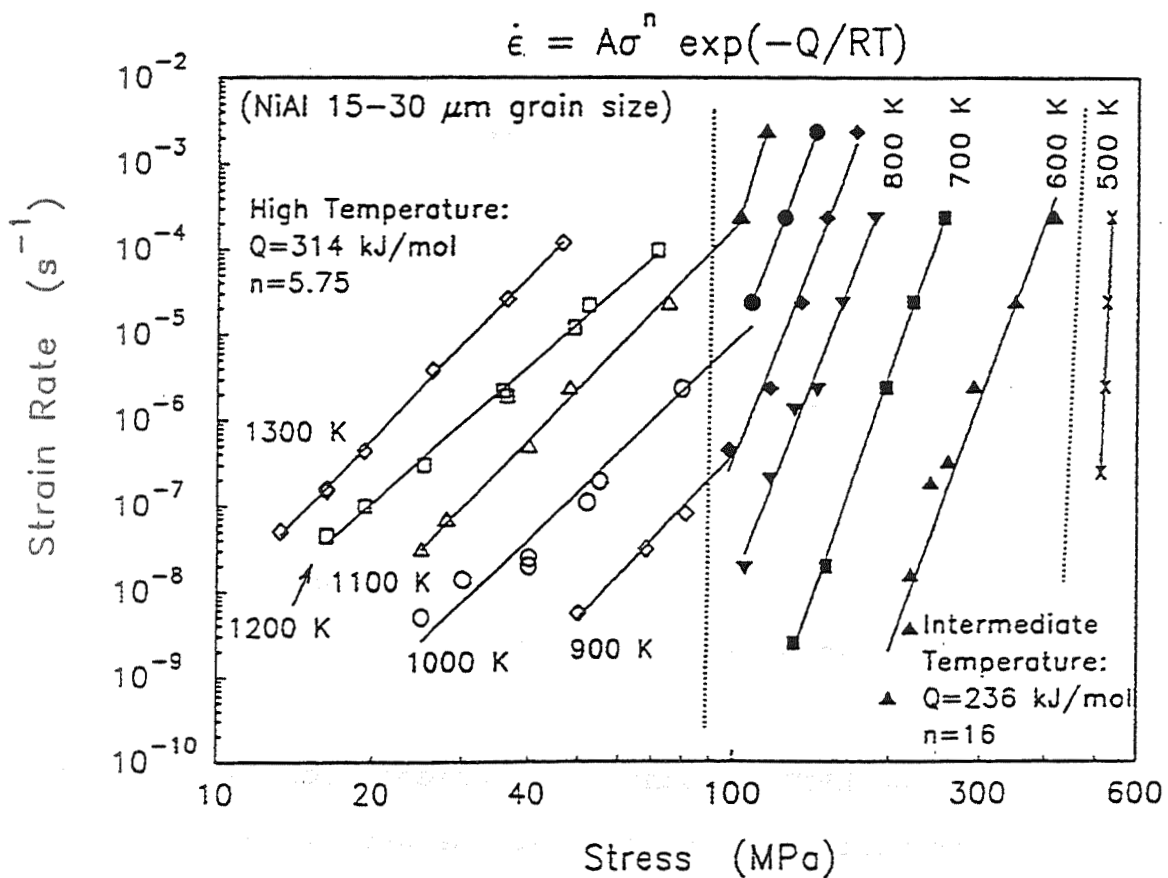


Figure 12: The steady state flow stress for NiAl as a function of strain rate and temperature. The low temperature regime is denoted by X, intermediate temperature regime by open, and high temperature regime by closed symbols [37].

observation of this mechanism confirms the transitions between all three of the temperature regimes illustrated in Fig. 12.

## 2.7 Ductility and Fracture Toughness

Early investigations of soft oriented NiAl reported an elongation at room temperature of approximately 1% [56,57]. Single crystal  $\beta$ -NiAl has 1-3% ductility and a fracture toughness of approximately 4-10 MPa $\sqrt{m}$  [1,19,36,47,58] depending upon orientation. However, recent investigation concerning specific heat treatments have shown an increase in ductility to 5-7%. Polycrystalline  $\beta$ -NiAl has tensile ductility of 0-3% and a fracture toughness of 4-7 MPa $\sqrt{m}$  [9,24]. Above the DBTT, fracture toughness values are in the range 20-50 MPa $\sqrt{m}$  [9,24], with a peak in ductility for single crystals in the range of 84-190% at temperatures just above the DBTT, depending on orientation [49]. At higher temperature, necking reduces the ductility to approximately 50%. The large elongations at intermediate temperatures result from a balance between work hardening and recovery which results in a high resistance to necking [49].

Recent investigations have revealed that fracture toughness is extremely sensitive to thermal history. When rapidly cooled from 1573 K,  $\langle 110 \rangle$  notched double cantilever



beam specimens had a fracture toughness of 16 MPa√m, but if subsequently annealed at 473 K and slowly cooled the value fell to only 3 MPa√m [38]. Thus strain aging may affect the yield strength and ductility of NiAl.

## 2.8 Creep Strength

The creep resistance of  $\beta$ -NiAl, defined as the stress required to produce a secondary creep rate of  $10^{-7} \text{ s}^{-1}$ , is lower than that of current superalloys [1,9,17]. The data shown in Figure 13 are typical of NiAl, and show power-law behavior, at least above a strain rate of  $10^{-8}$  [17]. The secondary creep rate,  $\dot{\epsilon}$ , is more generally expressed using a form of the Dorn equation:

$$\dot{\epsilon} = A \left( \frac{\sigma}{E} \right)^n \exp \left( \frac{-Q}{RT} \right)$$

where  $\sigma$  is the applied stress,  $E$  is Young's modulus,  $n$  is the stress exponent,  $Q$  is the activation energy for creep,  $R$  is the gas constant,  $T$  is the absolute temperature, and  $A$  is a constant involving the effects of microstructure and anti-phase boundary energies. The values of  $Q$  and  $n$  depend on the active deformation mechanisms. The stress exponent,  $n$ , was found to be between 4 and 5, indicating that creep in

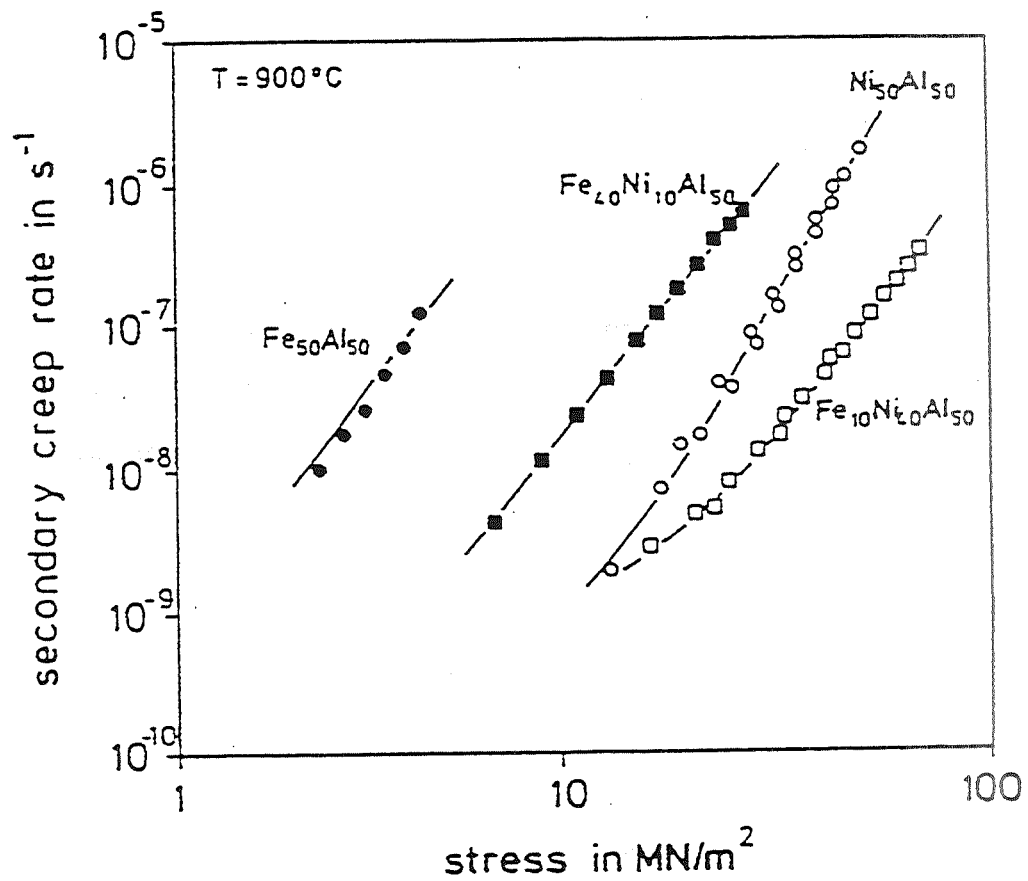


Figure 13: Typical creep data for NiAl, showing power law behavior at strain rates above  $10^{-8}$  [17].

$\beta$ -NiAl is controlled by dislocation climb [17]. Since creep is often related to diffusion-based processes, the value of  $Q$  is frequently on the order of  $Q_D$ , the activation energy for diffusion. Hence, the minimum in diffusion rate corresponds to the minimum creep rate with regard to stoichiometry and alloy additions. Generally the activation energy is lower at lower temperature and higher stress levels [24].

Dislocation creep is generally separated into two classes, M and A, for pure metal and alloy type behavior. Class M behavior is generally characterized by a stress exponent near 5 although values as high as 7 have been reported [59]. Creep of materials in this class is controlled by the rate of dislocation climb past obstacles, with dislocation glide occurring much faster. Class A behavior is often called viscous glide controlled creep and is generally characterized by a stress exponent of 3. Creep of Class A materials is governed by glide of dislocations where climb occurs very readily. High lattice friction due to long range order and solute drag effects contribute to reduced glide mobility [37].

The stress exponent of  $\beta$ -NiAl ranges from 4 to 7 for a wide variety of grain sizes, including single crystals, and over a temperature range of 1100 to 1400 K. Above 1000 K, values of  $n$  are generally lower for non-stoichiometric

compositions [55,60]. Noebe recently summarized other observations that also indicate that NiAl is a Class M material [37]. Specific examples include subgrain formation during high temperature deformation [60,61], normal primary creep behavior under both constant load and constant crosshead displacement conditions [55,62,63], strengthening by reduction in grain size [63], and strain rate transient results [64,65].

Nabarro-Herring and Coble creep are controlled by vacancy diffusion and are characterized by a stress exponent of 1. This type of deformation can occur at stress levels below that required for dislocation glide. Because this mechanism is controlled by vacancy diffusion, a grain size dependence is observed, with large grained material exhibiting lower creep rates. Evidence of this type of creep has been observed in Ni-20Fe-50Al where  $n=1$  [66] and in binary NiAl at low stress levels and temperatures above 1300 K where  $n=1.6$  to 2.1 [67].

Although vacancy diffusion has been observed for high temperature, low applied stress conditions, the creep rate remains independent of stoichiometry in the range of 45-51 atom percent Ni [55,60,68]. However, as the composition deviates from stoichiometry, the melting temperature decreases rapidly. The resulting increase in diffusivity

may explain the observed loss in creep strength for compositions outside this range [37].

Comparison between creep studies shows a variation of nearly two orders of magnitude for polycrystalline NiAl [24,55,60,63,69]. The agreement for single crystal data is also poor [70,71]. The disagreement may be explained by variations in interstitial impurity levels [72], voids [60], prismatic dislocations punched from impurities [60], and inclusions [55,60,63,73].

### 3. ALLOYING ADDITIONS

Alloy additions at levels which maintain a single phase microstructure are generally intended to either facilitate slip on additional systems [74,75] or to getter impurities and improve grain boundary strength [9,36,47]. Alloy additions have varying effects on the ductility, toughness, and creep strength of NiAl. The quantity of alloy additions are separated into two levels: microalloying (less than 1 a/o) and macroalloying (more than 1 a/o).

Changes in mechanical properties due to alloy additions result primarily from the creation of dislocation atmospheres, variations in the effective Ni:Al ratio, and changes in the effective diffusion coefficient. Constitutional defects which arise from preferential

substitution of an alloy addition will contribute to the strengthening of the alloy. These mechanisms must be accounted for when analyzing the effects of alloy additions. Since the nature of the mechanism depends on the type of defects formed by the alloying addition, the following discussion of single phase NiAl-based alloys is separated into two sections concerning substitutional additions and interstitial additions.

### **3.1 Substitutional Alloy Additions**

Elements with a Goldschmidt radius less than 0.1 nm prefer the interstitial sites in NiAl [19]. With increasing Goldschmidt radii, the preference shifts to substitutional sites. If a substitutional addition shows a preference for either Ni or Al lattice sites, then the effective stoichiometry may also be affected - leading to further strengthening of the alloy. For example, Be substitutes almost exclusively on Al sites [76]. Atom probe measurements by Jayaram and Miller confirm the preference of Fe for Al sites, but also revealed an excess of Ni in the specimen studied [76]. They determined that the increase in yield strength is on the order of that for Ni-rich NiAl. Hence, the behavior appears to be related to stoichiometry. In addition, the strengthening characteristics may be

different for alloys where the addition is intentionally substituted for either Ni or Al in the alloy composition [77].

No acceptable solid solution hardening theory can explain all of the experimentally observed behavior of ordered intermetallic alloys such as NiAl [9,37,78,79]. In particular, certain microalloying additions, intended to enhance the grain boundary strength or to getter impurities from the matrix, have been shown to produce a significant increase in the room temperature tensile ductility of NiAl, but only at low concentration levels [1,18]. Near stoichiometric [110] single crystal NiAl doped with 1000 ppm of either Fe, Ga, or Mo shows an increase in room temperature tensile elongation from 1% to 6% attributed to gettering of impurities [18]. Further addition of the ternary element negates the effect, Fig. 5.

A major area of research interest concerns the lack of five independent slip systems in NiAl. Hence, many alloy development programs, both theoretical and experimental, have focused on changing the ordering energy, or anti-phase boundary energy (APB), by alloying NiAl with ternary additions. Sufficient change in the APB energy will permit the activation of additional or alternate slip systems [75,77,80-87]. Generally a macroalloying approach is required, where additions of more than 1 a/o are common.

However, macroalloying has shown very limited improvement in ductility due to the concurrent effects of solid solution strengthening [6,80,88].

Theoretical calculations provide guidance for selection of potential alloy additions and the quantities required for maximum effect on the APB energy. Interatomic potential models indicate that elements such as Mn, Cr, Fe, and V may reduce the APB energy up to 70% when preferentially substituted for either Ni or Al at levels near 17 atomic percent [83,84,89]. However, the actual solubility of these elements in NiAl is limited to levels below that required for the maximum theoretical effect on the APB energy. Furthermore, theoretical analyses generally do not take into consideration the effects of solid solution hardening. In fact, solid solution effects have been shown experimentally to dominate the mechanical behavior.

The effects of Hf, Zr, Cu, Cr, Fe, Ga, La, Mo, Ni, Re, W, Y, and Be have been determined experimentally [9,88], some are shown in Fig. 14. The low cleavage strength of NiAl [90] is responsible for transgranular fracture. Intergranular fracture results when yielding produces strain incompatibilities at the grain boundaries. Only relatively pure NiAl and NiAl-Be alloys yield before fracture [9]. The effect of low levels of Zr, Cr, and V is significant only above the DBTT [75,86,91]. Auger studies indicate that Zr



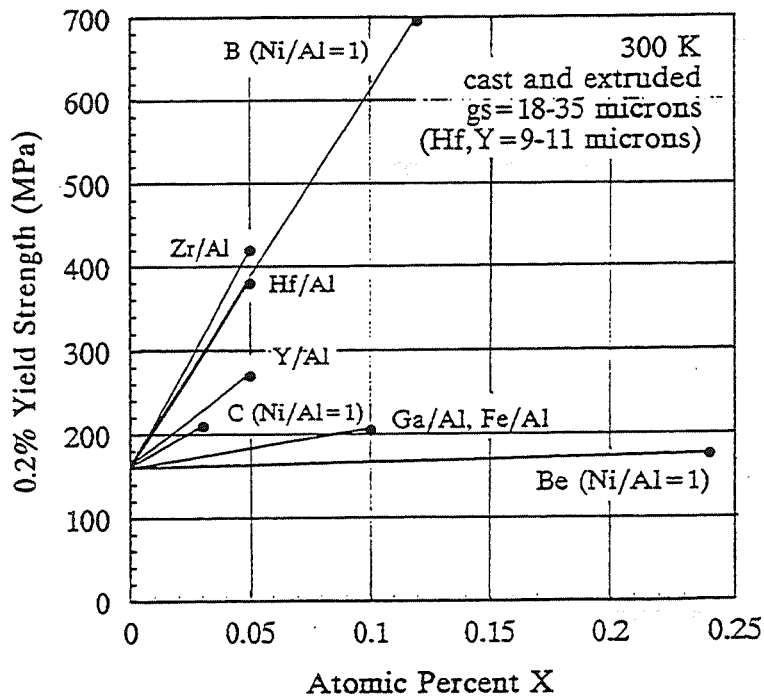
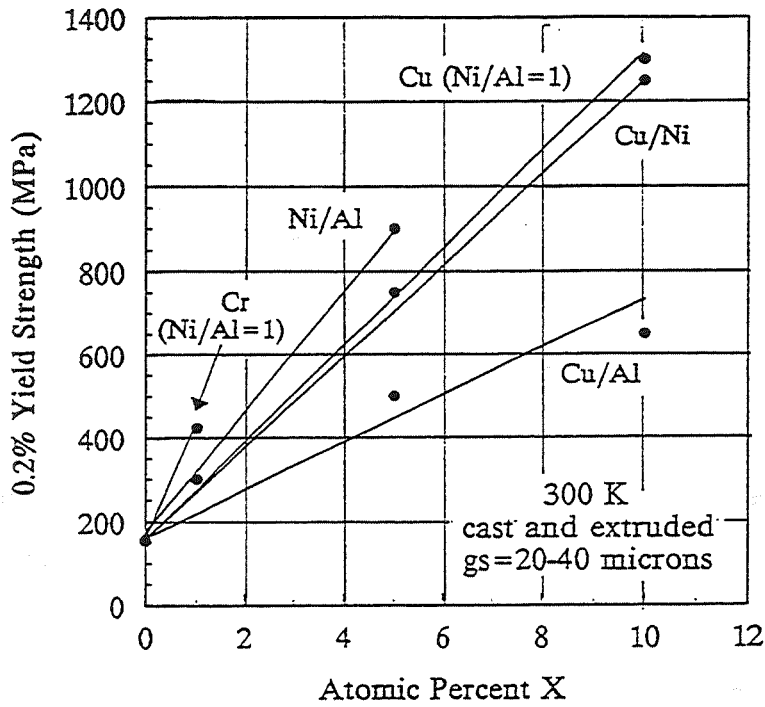


Figure 14: The effects of various elements on the mechanical properties of NiAl [9,80,88].

segregates to the grain boundaries [92]. The DBTT is strongly affected by Zr additions, increasing to 850 - 875 K [9]. The solid solution effect of Mo additions is potent, but Mo has limited solubility in NiAl. Hafnium is an unusually potent strengthener in NiAl [18].

Thermally activated processes begin to affect the mechanical properties of binary NiAl at temperatures near one third of its absolute melting point (Fig. 15) [37]. Various alloy additions intended to enhance the creep strength of binary NiAl have been examined including Fe, Ti, Co, Nb, Cr, Ta, Zr, and Hf [9;93-96]. However, it was determined for Nb, Ta, and Ti additions that long term improvements in the creep strength of polycrystalline NiAl-based materials are difficult to achieve through solid solution or precipitation hardening mechanisms [94]. This difficulty is due to effects of the thermal instability and the size and distribution of the precipitates, as well as a low stress exponent for essentially all Nb, Ta, and Ti additions [94].

Additions which alter the Ni:Al ratio not only affect the room temperature properties, but the diffusivity and therefore the creep strength [17]. For example, changes in the effective diffusion coefficient with additions of iron to NiAl [17,69,97] are shown in Fig. 16. The peak in creep resistance coincides with the minimum in the diffusion

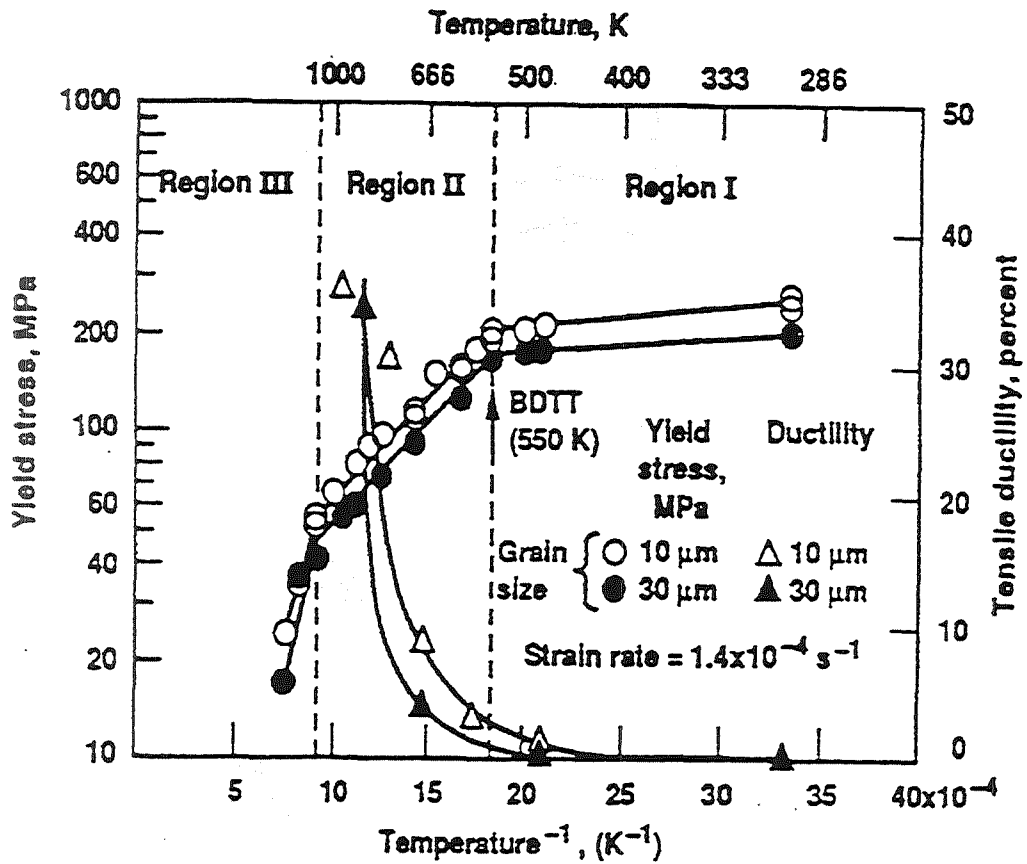


Figure 15: Arrhenius representation of the yield stress for polycrystalline NiAl and tensile ductility as a function of inverse temperature. The DBTT corresponds to a change in activation energy for plastic flow beginning at Region II [37].

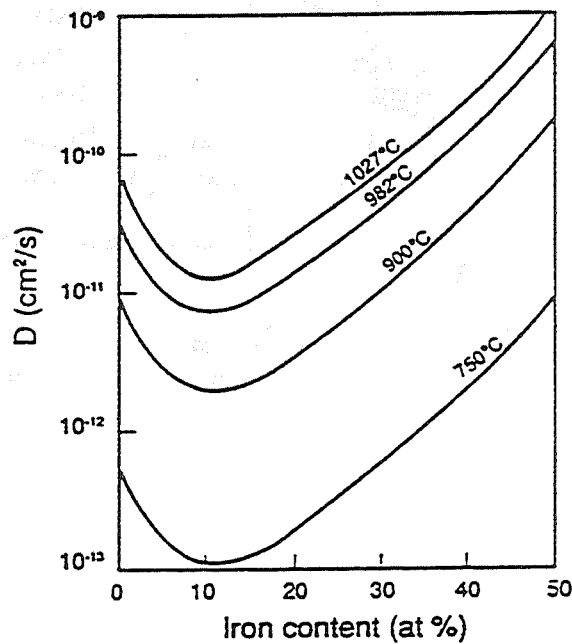
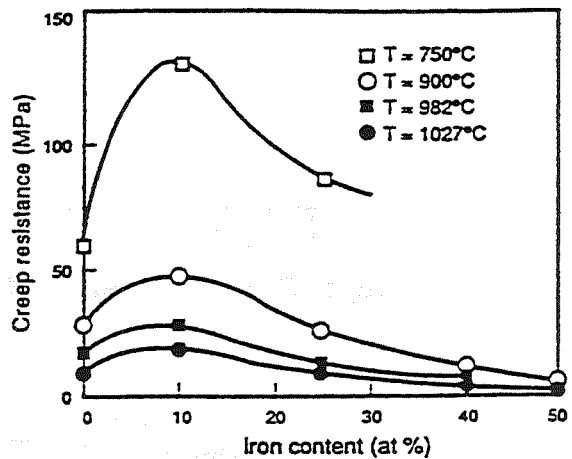


Figure 16: Diffusion coefficient as a function of Fe content in NiAl [69].

coefficient [17,97]. Since the diffusivity of NiAl is affected by stoichiometry, alloy additions which substitute preferentially for either Ni or Al will also affect the creep resistance. As pointed out, the problem is preserving ductility at lower temperatures using this approach [1]. Multiphase alloys will be discussed in greater detail in a later section.

The fracture toughness of alloyed NiAl is very sensitive to composition, but the dependence is not well understood due to a lack of compositional characterization [98,99]. Stoichiometry has little effect within the  $\beta$ -phase field. An unexpected and unexplained increase in fracture toughness is observed for 5 at% additions of either Nb or Ti [100]. Alloy additions of Fe, Mo, and Ga at levels which increase the tensile ductility, also increase the fracture toughness [1]. The largest increases in toughness result from multi-phase structures as discussed in detail later.

### **3.2 Interstitial Alloy Additions**

The effects of interstitial contamination on the mechanical properties of NiAl is a commonly cited source of discrepancy between the results of individual studies [9,24]. It has been shown experimentally that alloy additions which reside in the interstitial sites of NiAl are

also potent solid solution strengtheners, Fig. 6 [19,101,102]. Despite this evidence, purity levels are often not included with the published mechanical property data.

Recent studies using Auger analysis indicate that while C, O, and S do not segregate to grain boundary surfaces [19,92], B does [19]. Atom probe field ion microscopy (APFIM) has confirmed B segregation to grain boundaries. In addition, impurities such as Ti, V, Cr, and W precipitate from the matrix as  $MB_2$  when the total impurity level is greater than 460 appm, where M is the metallic element [76]. Hence, B getters substitutional impurities which are often present even in high purity Ni. Though C does not segregate to the grain boundaries, it was found to be twice as effective as B at getting metallic impurities [76]. In the case of C, the precipitates found by APFIM are of the MC type.

The yield strength is increased significantly for B and C additions. While high purity NiAl has a yield strength of 154 MPa [19], addition of 0.12 a/o B increases the yield strength to 329 MPa and for 0.1 a/o C to 336 MPa [19]. The presence of  $MB_2$  and MC precipitates in NiAl was addressed as the possible source of the increase in yield strength [76]. Using the measured B and C concentrations in the bulk NiAl, it was determined that solid solution hardening does not

account for all of the observed increase in yield strength. However, precipitation hardening contributions, which were estimated using the theoretical Orowan stress, can account for most of the observed increase in yield strength. These results reinforce the importance of purity for accurate determination of both mechanical properties and the effects of alloying additions.

The fracture mode was observed to change from intergranular to transgranular with the addition of B [19]. The increase in yield strength with B addition is more than 1500 MPa per atomic percent. Thus, for B-doped NiAl, the cleavage stress is surpassed prior to yielding and the fracture mode becomes transgranular cleavage.

The effect of interstitial contamination has recently been associated with an extreme sensitivity to heat treatment and cooling rate in commercial purity single crystal NiAl [38]. Fast cooling through the 400 to 20°C range gives 7% ductility and a fracture toughness of 13-17 MPa√m, while annealing similarly processed specimens at 200°C for 1.5 hours gives a fracture toughness of 2.8 MPa√m [38], Table 3. This type of behavior has been compared to the strain aging effect of carbon in iron [38]. Bieler, Noebe, and Hebsur [104] studied N additions to NiAl and found an increase in fracture toughness to 8 MPa√m due to lower levels of C in the N containing specimens. Both O and

C have low solubilities in NiAl. This phenomenon will also be discussed in more detail later.

Table 3: Fracture toughness of CP-NiAl\*

$K_{Ic}$ (MPa $\sqrt{m}$ )	CONDITION	REF.
2 - 4	as-processed	[36, 38]
2.8	1573 K/3hr/AC+473 K/1.5hr/SC	[38]
10 - 15	1573 K/3hr/AC	[38]

\* Double cantilever beam test.

The effects of interstitial impurities are not limited to room temperature properties though very little work has been done concerning the effect of interstitial additions on high temperature properties. For example, a significant decrease in the creep strength of NiAl results from addition of as little as 420 wppm C [72]. Precipitates of AlN and Al<sub>2</sub>O<sub>3</sub> have been found to benefit the creep strength [37].

### 3.3 Grain Refinement

Grain refinement is intended to increase the fracture toughness. This permits a higher applied stress before failure, resulting in an increase in the measured elongation to failure [39,105]. However, improvement in ductility by grain refinement alone is impractical [9]. While improvements in ductility with sufficiently small grain sizes have been observed [39,106], rapid grain growth during



processing makes production of ultra-fine grain size difficult. Likewise, grain growth during elevated temperature service severely limits the longevity of the effect. Alloy additions made to inhibit grain growth usually produce significant strengthening, leading to brittle behavior. The critical grain size for improved ductility is estimated to be less than 1  $\mu\text{m}$ , but depends on stoichiometry, temperature, and alloy composition [6,39,106]. The grain size effect decreases as the Ni:Al ratio deviates further from stoichiometry [24,106]. At 300 K and grain sizes above 1  $\mu\text{m}$ , ductility is essentially independent of grain size [9].

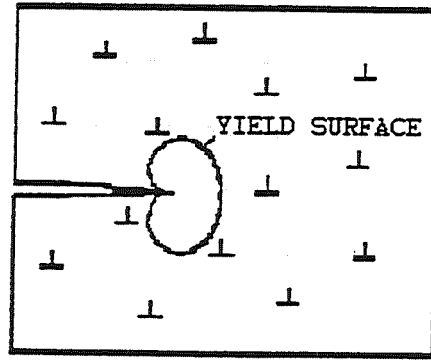
### **3.4 Dislocation Density Effects**

The ductility of the bcc refractory metals Cr, Mo, and W is known to be mobile dislocation density limited [38,107]. The same is reported of  $\beta$ -NiAl [38,108]. In support of this theory, oxide coatings were shown to improve ductility by serving as efficient sources of mobile edge dislocations [108]. Thermal and thermomechanical treatments were also shown to improve ductility and toughness by increasing the initial mobile dislocation density [38]. While oxide coatings and thermomechanical processing have been shown to increase the mobile dislocation density, it

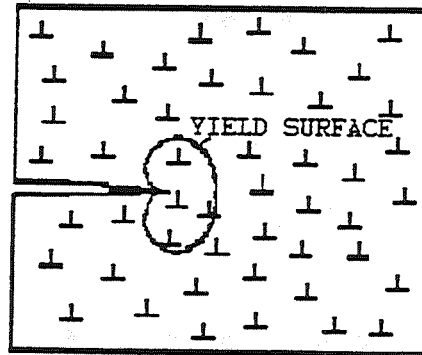
should be noted that these dislocations are not of a different character than for untreated NiAl. Therefore, these treatments do not increase the number of independent slip systems.

The reason for poor ductility and fracture toughness in a mobile dislocation density limited material can be understood from a fracture mechanics approach. The spacing of mobile dislocations in relation to the extent of the yield surface dictates the nature of the material (Fig. 17). If the yield surface size exceeds the spacing, then the material behaves in a ductile manner. Whereas if the spacing is too large, the stress intensity at the crack tip decays before causing glide of mobile dislocations and the material acts as if no mobile dislocations are present at all [38].

It should be emphasized that the techniques which have been shown to generate mobile dislocations produce only  $\{110\}\langle 001\rangle$  dislocations [47,109]. The lack of 5 independent slip systems required for a generalized change of shape remains. With this restriction, any yielding in a polycrystalline specimen will generate incompatible strains at the grain boundaries, leading to microcracking and failure by a Griffith type mechanism.



BRITTLE BEHAVIOR



DUCTILE BEHAVIOR

Figure 17: Mobile dislocation density -vs- fracture behavior in NiAl.

#### 4. MULTI-PHASE ALLOYING

Extrinsic effects due to the presence of more than one phase occur often in NiAl due to the low solubility for many of the candidate alloying elements. In fact, a very common extrinsic approach to property enhancement is to incorporate a ductile phase within the brittle matrix which results in greater composite ductility through increased toughness [58,95,110]. There is also the possibility of slip transfer between the second phase and the matrix, i.e., an intrinsic mechanism [37,58]. Optimization of microstructure, phase distribution of the reinforcement, and composition has the potential to significantly improve ductility.

Attempts to improve the creep strength of NiAl include alloy additions [10,17,94,97] and composite reinforcement [97,10,95,111]. The alloy additions are intended to produce solid solution effects and fine dispersions of precipitates, similar in theory and approach to superalloy development. Composite reinforcement may include both ductile and brittle phase additions.

Refractory metals, such as Mo, V, and Cr, provide an excellent opportunity for ductile phase reinforcement since they form eutectics with  $\beta$ -NiAl. A primary advantage of eutectic alloys is the thermodynamic stability of the phases up to the melting temperature. However, microstructural stability is not inherent to eutectic alloys. Eutectic

reactions between NiAl and Heusler or Laves phases provide opportunities for brittle phase reinforcement. The superior creep properties of Heusler and Laves phases, over that of NiAl, have shown promising results for improving the creep strength of NiAl [1,10,95,111,112]. For a coarse phase distribution, the contribution of the reinforcement follows a rule of mixtures relationship. However, very fine distributions may result in an increased threshold stress for creep [111,113].

1. Introduction

2. Methodology

3. Results and Discussion

4. Conclusion

5. References

**REFERENCES**

- [1] R. Darolia, *J. Metals*, 43(1991)44.
- [2] Pearson's Handbook of Crystallographic Data for Intermetallic Phases, P. Villars and L.D. Calvert eds., ASM Metals Park, OH (1985).
- [3] J.L. Gonzalez-Carrasco, P. Adeva, and M. Aballe, *Mater. Sci. Engr.*, A128(1990)231.
- [4] W.S. Walston and R. Darolia, in "High Temperature Ordered Intermetallic Alloys V", I. Baker et al., eds., MRS Symp. Proc. 288(1993)237.
- [5] E.-T. Henig and H.L. Lukas, *Z. Metallk.*, 66(1975)98.
- [6] R.D. Noebe, R.R. Bowman, and M.V. Nathal, NASA TM-105598 (1992)17.
- [7] P. Nash, M.F. Singleton, and J.L. Murray, in *Phase Diagrams of Binary Nickel Alloys*, Vol. 1, P. Nash ed., ASM Metals Park, OH (1991).
- [8] A. Taylor and N.J. Doyle, *J. Appl. Cryst.*, 5(1972)201.
- [9] R.D. Noebe, R.R. Bowman, and M.V. Nathal, *Int. Mat. Rev.*38, 4(1993)193.
- [10] K. Vedula, V. Pathare, I. Aslanidis, and R.H. Titran, MRS Symp. Proc. 39(1985)411-421.
- [11] A.J. Bradley and A. Taylor, *Proc. Roy. Soc.*, 103(1956)54.
- [12] M.J. Cooper, *Phil. Mag.* 8(1963)805.
- [13] G.S. Sauthoff, *Z. Metallk.*, 81(1990)855.
- [14] G.S. Sauthoff, in "High Temperature Aluminides and Intermetallics", S.H. Whang et al., eds., ASM/TMS(1990)329.
- [15] C.A. Barrett, *Oxidation of Metals*, 30(1988)361.
- [16] C.E. Lowell, C.A. Barrett, and J.D. Whittengerger, in *Intermetallic Matrix Composites*, D.L. Anton, et al., eds., MRS Symp. Proc. 194(1990)335.
- [17] G. Sauthoff, NATO ARW, "Ordered Intermet.-Phys. Met. and Mech. Behaviour", TISEE GER(1991).

- [18] R. Darolia, D.F. Lahrman, and R.D. Field, *Scripta Metall. Mater.*, 26(1992)1007.
- [19] E.P. George and C.T. Liu, *J. Mater. Res.*, 5, 4(1990)754.
- [20] R.T. Pascoe and C.W.A. Newey, *Metal Sci.J.*, 12(1968)138.
- [21] R.J. Wasilewski, *Met.Trans.* 236(1966)455.
- [22] M.R. Harmouche and A. Wolfenden, *J.Test.Eval.*, 15(1987)101.
- [23] N. Rusovic and H. Warlimont, *Phys. Stat. Sol. (A)*, 53(1977)283.
- [24] D.B. Miracle, *Acta Metall. Mater.*, 3, 41(1993)649.
- [25] W.S. Walston and R. Darolia, in *High Temperature Ordered Intermetallic Alloys V*, I. Baker, et al., eds. MRS Symp Proc. 288(1993)237.
- [26] T.R. Bieler, R.D. Noebe, J.D. Whittenberger, and M.J. Luton, in *"Intermetallic Matrix Composites II"*, D.B. Miracle et al., eds., MRS Symp. Proc. 273(1992)165.
- [27] K.J. Bowman, R.D. Noebe, J.R. Jenny, S.T. Kim, *Mater. Sci. Eng. A160*(1993)201.
- [28] C.A. Moose, M.S. Thesis, Pennsylvania State University, University Park, PA, (1991).
- [29] R.D. Noebe, A. Misra, and R. Gibala, *Iron Steel Inst. Jap. Int.*, 31(1991)1172.
- [30] R.J. Wasilewski, S.R. Butler, and J.E. Hanlon, *Trans. Metall. Soc., AIME*, 239(1967)1357.
- [31] R.D. Field, D.F. Lahrman, and R. Darolia, in *"High Temperature Ordered Intermetallic Alloys IV"*, MRS Symp. Proc.213(1991)255.
- [32] R.T. Pascoe and C.W.A. Newey, *Phys. Stat. Sol.* 29(1968)357.
- [33] A. Ball and R.E. Smallman, *Acta Metall.*, 14(1966)1517.
- [34] M.H. Loretto and R.J. Wasilewski, *Phil. Mag.*, 23(1971)1311.



- [35] Ha K. DeMarco and A.J. Ardell, in "Intermetallic Matrix Composites II", D.B. Miracle et al., eds., MRS Symp. Proc. 273(1992)
- [36] K.-M. Chang, R. Darolia, and H.A. Lipsitt, Acta Metall. Mater., 40(1992)2727.
- [37] R.D. Noebe, NASA Tech. Mem. 106534, Lewis Research Center, Cleveland, OH (1994).
- [38] J.E. Hack, J.M. Brzeski, and R. Darolia, Scripta Metall. Mater., 27(1992)1259.
- [39] E.M. Schulson, in "High Temperature Ordered Intermetallic Alloys", C.C. Koch et al., eds., MRS Symp. Proc. 39(1985)194.
- [40] R.R. Bowman, R.D. Noebe, and R. Darolia, HIGHTEMP Review-1989, NASA CP-10039, (1989)47-1.
- [41] K.H. Hahn and K. Vedula, Scripta Metall., 23(1989)7.
- [42] J.D. Whittenberger, R.D. Noebe, C.L. Cullers, K.S. Kumar, and S.K. Manon, Metall. Trans. A, 22A(1991)1595.
- [43] M.L. Weaver, M.J. Kaufman, and R.D. Noebe, Scripta Metall. Mater., 29(1993)1113.
- [44] D.B. Miracle, Acta Metall. Mater., 39(1991)1457.
- [45] A.G. Rozner and R.J. Waselewski, J. Inst. Metals, 94(1966)169.
- [46] J.H. Westbrook, J. Electrochem. Soc., 103(1956)54.
- [47] R.D. Noebe, R.R. Bowman, C.L. Cullers, and S.V. Raj, High Temp. Rev., NASA CP-10051, (1990)20-1.
- [48] D.F. Lahrman, R.D. Field, and R. Darolia, in "High Temperature Ordered Intermetallic Alloys IV", L. Johnson et al., eds., MRS Symp. Proc. 213(1991)603.
- [49] T. Takasugi, J. Kishino, and S. Hanada, Mat. Sci. Eng., A149(1992)183.
- [50] J.T. Kim, Ph.D. Thesis, University of Michigan, Ann Arbor, MI, (1990).
- [51] J.T. Kim and R. Gibala, in High Temperature Ordered Intermetallic Alloys IV, L. Johnson, ed., MRS Symp. Proc., 213(1991)261.

- [52] R.D. Field, D.F. Lahrman, and R. Darolia, *Acta Metall. Mater.*, 39(1991)2591.
- [53] H. Brophy, R.M. Rose, and J. Wulff, *Thermodynamics of Structure*, John Wiley & Sons, Inc., (1967)80.
- [54] P.G. Shewmon, *Diffusion in Solids*, McGraw-Hill, (1983)170.
- [55] J.D. Whittenberger, *J. Mater. Sci.*, 22(1987)394.
- [56] D.F. Lahrman, R.D. Field, and R. Darolia, *Scripta Metall. Mater.*, 28(1993)709.
- [57] T. Takasuge, J. Kishino, and S. Hanada, *Acta Metall. Mater.*, 41(1993)1009.
- [58] R.D. Noebe, F.J. Ritzert, A. Misra, and R. Gibala, *NASA Tech. Memo, NASA TM-103796*, (1991).
- [59] M.F. Ashby, *Acta Metall.*, 20(1972)887.
- [60] W.J. Yang and R.A. Dodd, *Met. Sci. J.*, 7(1973)41.
- [61] W.R. Kanne, P.R. Strutt, and R.A. Dodd, *Trans. Metall. Soc. AIME*, 245(1969)1259.
- [62] P.R. Strutt, R.A. Dodd, and G.M. Rowe, in *"Strength of Metals and Alloys"*, Vol. III, ASM International, Metals Park, OH, (1970)1057.
- [63] J.D. Whittenberger, *J. Mater. Sci.*, 23(1988)235.
- [64] D.L. Yaney and W.D. Nix, *J. Mater. Sci.*, 23(1988)3088.
- [65] K.R. Forbes, U. Glatzel, R. Darolia, and W.D. Nix, in *"High Temperature Ordered Intermetallic Alloys V"*, I Baker et al., eds., *MRS Symp. Proc.* 288(1993)45.
- [66] M. Rudy and G. Sauthoff, in *"High Temperature Ordered Intermetallic Alloys"*, C.C. Koch et al., eds., *MRS Symp. Proc.* 39(1985)327.
- [67] S.V. Raj and S.C. Farmer, in *"High Temperature Ordered Intermetallic Alloys V"*, I Baker et al., eds., *MRS Symp. Proc.* 288(1993)647.
- [68] J.D. Whittenberger, K.S. Kumar, and S.K. Mannan, *J. Mater. Sci.*, 26(1991)2015.

- [69] M. Rudy and G. Sauthoff, *Mater. Sci. Eng.*, 81(1986)525.
- [70] L.A. Hocking, P.R. Strutt, and R.A. Dodd, *Inst. Met. J.*, 99(1971)98.
- [71] J. Bevk, R.A. Dodd, and P.R. Strutt, *Metall. Trans.*, 4(1973)159.
- [72] A. Prakash and M.J. Pool, *J. Mater. Sci.*, 16(1981)2495.
- [73] K. Sadananda, H. Jones, C.R. Feng, and A.K. Vasudevan, in "High Temp. Ordered Int. Alloys IV", L. Johnson, J.O. Stiegler, and D.P. Pope, eds., *MRS Proc.* 213(1991)679.
- [74] D.B. Miracle, S. Russel, and C.C. Law, in "High-Temperature Ordered Intermetallic Alloys III", C.T. Liu et al., eds., *MRS Symp. Proc.* 133(1989)225.
- [75] R.D. Field, D.F. Lahrman, and R. Darolia, *Acta Metall. Mater.*, 39(1991)2961.
- [76] R. Jayaram and M.K. Miller, *Acta Metall. Mater.*, (199)
- [77] J.D. Cotton, M.J. Kaufman, R.D. Noebe, and M. Behbehani, in *HITEMP Review-1991*, NASA CP-10082, (1991)23-1.
- [78] R.L. Fleischer, in "High Temperature Ordered Intermetallic Alloys V", I. Baker et al., eds., *MRS Symp. Proc.* 288(1993)165.
- [79] D.M. Dimiduk and S. Rao, in "High Temp. Ordered Int. Alloys IV", L. Johnson, J.O. Stiegler, and D.P. Pope, eds., *MRS Symp. Proc.* 213(1991)499.
- [80] J.D. Cotton, R.D. Noebe, and M.J. Kaufman, *Intermetallics*, 1(1993)117.
- [81] C.C. Law and M.J. Blackburn, Report # ED/GPD FR-18674-4, United Technologies Corp., Pratt and Whitney Group, West Palm Beach, FL, (1985).
- [82] C.C. Law and M.J. Blackburn, Final Technical Report, AFWAL-TR-87-4102, United Technologies Corp., Pratt and Whitney Group, West Palm Beach, FL, (1987).
- [83] T. Hong and A.J. Freeman, in "High Temperature Intermetallic Alloys III", C.T. Liu et al., eds., *MRS Symp. Proc.* 133(1989)75.

- [84] T. Hong and A.J. Freeman, Phys. Rev. B, 43(1991)6446.
- [85] J.D. Cotton, Ph.D. Thesis, University of Florida, (1991), also available as NASA CR-189124, (1992).
- [86] R. Darolia, D.F. Lahrman, R.D. Field, and A.J. Freeman, in "High Temperature Intermetallic Alloys III", C.T. Liu et al., eds., MRS Symp. Proc. 133(1989)113.
- [87] D.B. Miracle, S. Russell, and C.C. Law, in "High Temperature Intermetallic Alloys III", C.T. Liu et al., eds., MRS Symp. Proc. 133(1989)225.
- [88] J.D. Cotton, R.D. Noebe, and M.J. Kaufman, ISSI, R. Darolia et al., eds., TMS, (1993)513.
- [89] C.L. Fu and M.H. Yoo, Acta Metall. Mater. 40(1992)703.
- [90] M.H. Yoo and C.L. Fu, Scripta Metall. Mater., 25(1991)2345.
- [91] R.D. Noebe, R.R. Bowman, I.E. Locci, and S.V. Raj, in "HITEMP Rev-1989", NASA CP-10039, (1989)48-1.
- [92] M.V. Zeller, R.D. Noebe, and I.E. Locci, in "HITEMP Review-1990", NASA CP-10051, (1990)21-1.
- [93] J.D. Whittenberger, M.V. Nathal, S.V. Raj, and V.M. Pathare, Mater. Lett. 11(1991)267.
- [94] J.D. Whittenberger, L.J. Westfall, and M.V. Nathal, Scripta Met., 23(1989)2127.
- [95] G. Sauthoff, JIMIS-6, J. Inst. Metals, O. Izumi, ed., Sendai, Japan, (1991)371.
- [96] J. Klower and G. Sauthoff, Z. Metallkd., 83(1992)9.
- [97] G. Sauthoff, in "High-Temperature Aluminides and Intermetallics", C.T. Liu et al., eds., ASM/TMS, Metals Park, OH, (1990)329.
- [98] S. Reuss and H. Vehoff, Scripta Metall. Mater., 24(1990)1021.
- [99] K.S. Kumar, S.K. Mannan, and R.K. Viswanadham, Acta Metall. Mater., 40(1992)1201.
- [100] W.A. Kaysser, R. Laag, J.C. Murray and G.E. Petzow, Int. J. Powder. Metall., 27(1991)43.

- [101] J.H. Westbrook and D.L. Wood, *J. Inst. Metals* 91(1962)174.
- [102] A.U. Seybolt and J.H. Westbrook, *Acta Metall.*, 12(1964)1456.
- [103] American Society for Metals, *Metals Handbook*, 9th ed., Vol. 11, ASM Metals Park, OH (1986).
- [104] T.R. Bieler, R.D. Noebe, M. Hebsur, and R. Saminathan, in "Advances in Hot Deformation Textures and Microstructures", K.J. Bowman et al., eds., TMS, Warrendale, PA (1994).
- [105] K.S. Chan, *Scripta Metall. Mater.*, 24(1990)1725.
- [106] E.M. Schulson and D.R. Barker, *Scripta Metall.*, 17(1983)519.
- [107] American Society for Metals, *Metals Handbook*, 9th ed., Vol. 3, ASM Metals Park, OH (1980).
- [108] R.D. Noebe and R. Gibala, in "High Temperature Ordered Intermetallic Alloys", C.C. Koch et al., eds., MRS Symp. Proc. 39(1985)319.
- [109] R.D. Noebe, in "High-Temperature Aluminides and Intermetallics", C.T. Liu et al., eds., ASM/TMS, Metals Park, OH, (1990)271.
- [110] F.E. Heredia, M.Y. He, G.E. Lucas, A.G. Evans, H.E. Deve, and D. Konitzer, *Acta Metall. Mater.*, 41(1993)505.
- [111] J. Klower and G. Sauthoff, *Z. Metallkde.*, 82(1991)510.
- [112] R.W. Cahn, *MRS Bull.*, 16(1991)18.
- [113] G. Sauthoff, C-MRS International, "Intermetallic Alloys-Overview on New Materials Developed for Structural Applications", Beijing (1990).

**PART II: SCOPE AND PURPOSE**

Several conclusions may be drawn from the previous investigations of NiAl and NiAl-based alloys reviewed in PART I.

First, a high level of purity is difficult to achieve in NiAl alloys. In fact, many discrepancies between similar studies have been attributed to variations in purity levels. It should be noted that NiAl is highly reactive in the liquid state and therefore highly susceptible to contamination. Conventional processing techniques, i.e., Bridgman type processes, may limit purity levels by chemical interaction between the crucible material and the molten NiAl.

Second, most efforts to improve room temperature ductility and fracture toughness have centered on either overcoming contamination by gettering impurities with micro-alloying additions (<1.0 a/o) or by activation of additional or alternative slip systems by macro-alloying additions. However, most alloy additions have proven to be very potent solid solution strengtheners in NiAl. The most successful improvement in tensile ductility has been attributed to gettering of impurities, at least for low levels of Fe, Ga, or Mo, but the effect is lost for higher concentrations. Activation of alternate slip systems has been shown only under specific test conditions, where the Schmid factor is very low on the normally active  $\langle 001 \rangle \{ 110 \}$  system.

Increasing the number of mobile dislocations does not address the lack of independent slip systems. Nickel aluminide has only 3 independent slip systems and therefore, does not satisfy the Von Mises criterion for a generalized change of shape. Techniques such as thermo-mechanical processing and slip transfer from thin films have been successful in increasing the number of  $\langle 001 \rangle$  type dislocations, but the improvement in ductility has been limited.

Alloy additions can alter the effective Ni:Al ratio and therefore the diffusivity of the alloy. Since creep strength is directly related to the diffusivity, the creep strength of the alloy is also affected by alloy additions. Additions which tend to improve the creep strength also tend to embrittle the alloy at low temperatures.

These observations do not exclude the possibility that an alloying approach may be found which accomplishes the intended property enhancement of single phase NiAl. However, the most promising avenue for property enhancement of NiAl appears to be careful processing of multi-phase alloys. Particularly promising are in-situ composites based on directional solidification of eutectic alloys. The presence of a second phase within an NiAl matrix creates the potential for crack bridging, crack trapping, debonding, crack branching, shear ligament formation, slip transfer



between the reinforcement and matrix, and other fracture toughness enhancing mechanisms. Furthermore, the addition of Laves or Heusler type phases to an NiAl matrix provides the potential for increased creep strength.

The purpose of this research was to identify, directionally solidify, and characterize NiAl-based in-situ composites in terms of their potential to improve the room temperature fracture toughness and creep strength of NiAl. Characterization of high purity NiAl provided the baseline for comparison with the eutectic alloys in order to clarify the effects of purity on the results. Finally, an assessment of the active fracture mechanisms and their contributions to fracture toughness were made by SEM characterization and simple models.

The scope of this research is broad and primarily experimental. Many different materials have been processed, many of which are new alloys. Therefore, the characterization of each has generally been limited to microstructure, phase constitution, phase relationships, room temperature fracture toughness, and 1300 K creep strength. In some cases, TEM characterization of the active slip systems, orientation relationships, and lattice parameter mismatch has been performed on the known eutectic alloys to examine any differences due to processing technique. Theoretical concerns have played a key role in

many aspects of this work, including identification of new eutectic alloys, processing, and failure analysis of the composite materials though they are not the primary focus.

For convenience, the results have been separated into four parts, IV through VII. Part IV concerns the characterization of binary NiAl to establish a baseline for comparison and assess the effects of the higher purity level produced by the containerless, electro-magnetically levitated zone process. Part V concerns the microstructure, slip systems, and mechanical properties of the binary eutectic alloys NiAl-9Mo and NiAl-40V, as well as the hypereutectic alloys NiAl-12Mo and NiAl-15Mo. These eutectics have been grown previously using a modified Bridgman process. Previous work has characterized their microstructures, high temperature stability, and phase relationships. Comparison between material produced by the two different processing techniques is included in Part V. Part VI contains the new ternary eutectic alloys along with their microstructural characterization, phase constitution, and mechanical property data. Finally, Part VII concerns the fracture of NiAl-based in-situ composite materials. Scanning electron microscopy is used to identify the dominant fracture mechanisms for each alloy. In some cases, a simple model has been applied to characterize the

contribution of crack bridging to the overall fracture toughness of the composite material.

**PART III: EXPERIMENTAL PROCEDURE**

## 1. INTRODUCTION

The differences between a typical Bridgeman technique, zone melting, and containerless electromagnetically-levitated zone (CELZ) processing as they relate to this work are briefly described in the following paragraphs. It is the containerless nature of the CELZ process, where only an ultra-high purity atmosphere is in contact with the ingot, which permits the solidification of high purity material.

The Bridgeman technique frequently used in the study of solidification involves withdrawing a crucible containing molten material from an energy source (electric furnace, induction coil, or other heating source) at a constant rate, thereby solidifying the material at that rate. The crucible generally rests on a water cooled pedestal (Fig. 18). This arrangement generally provides a temperature gradient sufficient to control the shape and position of the solid/liquid interface during crystal growth.

The heat flux near the solid/liquid interface must be nearly parallel to the axial direction of the ingot in order to maintain a planar geometry. The magnitude of the heat flux is due to the heat source, the heat of fusion released at the solidifying interface, the radiation loss from the surface of the crucible, the thermal conduction through the material being processed, and the size of the assembly. The

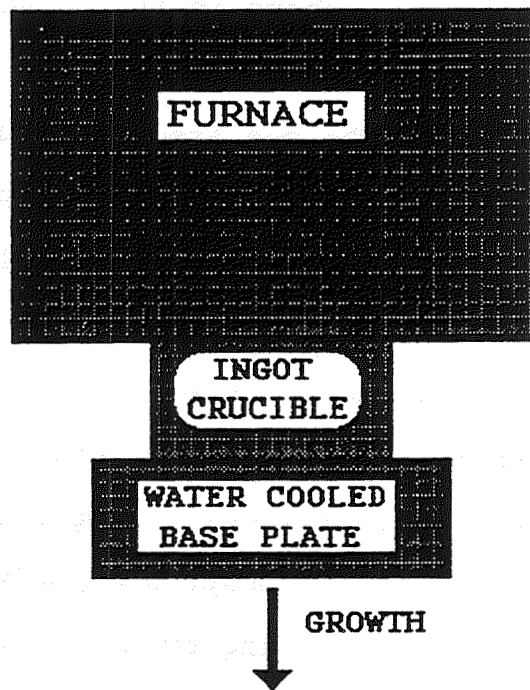


**Figure 18:** Schematic illustration of a modified Bridgman apparatus.

choice of crucible material is critical for reactive melts in order to minimize contamination of its contents.

Purification by fractional solidification under normal freeze conditions (such as in the Bridgeman technique) is more segregational than under zone melting conditions. Figure 19 is a graphical comparison of the composition versus axial distance along the ingot between normal freeze conditions and zone melting conditions. The actual shape of these curves depends on the partitioning coefficient, the fraction solidified or the zone length, and the solidification conditions such as the growth rate, diffusivity, and degree of mixing in the liquid. Since the degree of purification by fractional crystallization depends on material properties, many of which are not explicitly known for the materials to be studied here, the resulting compositions cannot usually be calculated. However, the emphasis is that limitations on the purity of NiAl-based ingots grown by a Bridgeman technique result from the crucible, not the actual solidification event or conditions.

The principal advantage of zone melting is the elimination of the crucible. "Certain materials are so reactive when molten that no known container can hold them without contamination"[1]. Nickel aluminide is very reactive in the liquid state and its mechanical properties are very sensitive to impurity concentrations. In this

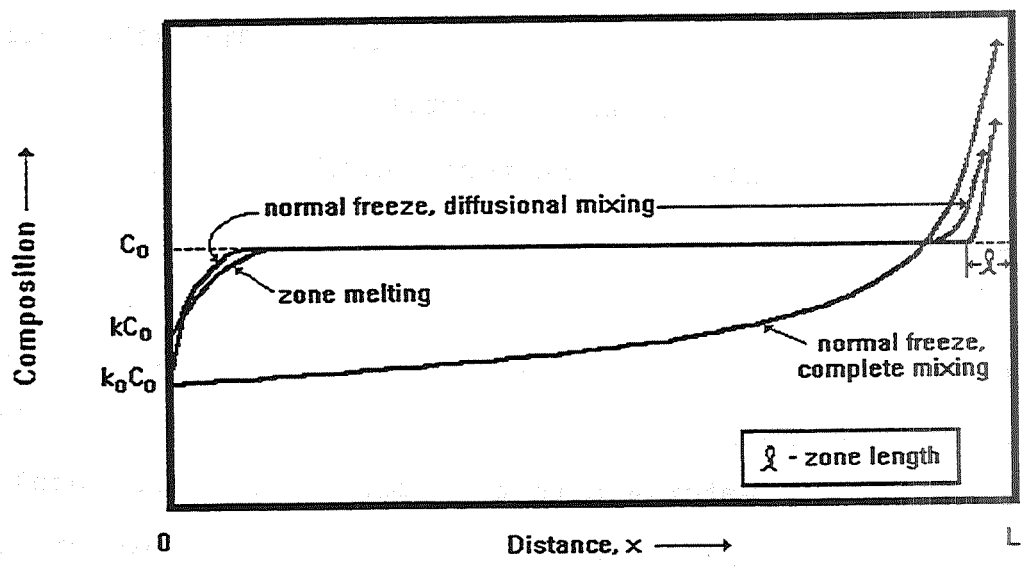


**Figure 19:** Composition of the freezing solid as a function of distance traveled under normal and zone melting conditions.



technique, the environment surrounding the liquid zone can be used as an open chemical reaction system to purify the liquid zone (hence the solidifying ingot) in addition to purification by fractional crystallization.

Zone melting and CELZ processing are essentially the same with the exception of ingot size limitations. Without the magnetic field containment, the height of the liquid zone is limited by the ratio of surface tension to density. For this reason, the diameters of float zone ingots are usually limited to approximately 8 mm. The high thermal conductivity of NiAl results in significant spreading of the heat and hence the liquid zone along the ingot axis, further limiting the diameter of the ingot. One way to decrease the height of the liquid zone is to focus the energy source to heat less material. In this way, use of an electron beam as an energy source may reduce the height of the zone, but it requires a vacuum environment. The use of focused high intensity light is limited by condensation of evaporated material on the mirrors or the ingot-encapsulating tube over the course of crystal growth. In addition, the use of electron beams, high intensity light, or radiant heating preclude the advantages of electromagnetic containment of the liquid zone.

## 2. CONTAINERLESS ELECTROMAGNETICALLY LEVITATED ZONE PROCESS (CELZ)

The ability to melt and simultaneously constrain or partially levitate the liquid zone is provided by induction coil-eddy current plate assemblies of various geometries that approximate slightly opened quadrupole fields [2,3]. A single geometry does not work for all systems since the melting range, thermal and electrical conductivity, density, emissivity, and other properties of intermetallic systems vary considerably. However, experience has shown that classes of systems behave similarly and may be processed with the same or similar induction coil geometries.

Directional solidification is accomplished by simultaneous control of two interdependent processing variables. These variables are the position of the solidifying interface and the liquid zone diameter just ahead of the freezing interface. A schematic of the process and control inputs is shown in Figure 20. The molten zone image is digitized by a 512 x 512 array of photodiodes, each representing one pixel with an intensity level between 0 and 256. The liquid diameter is determined at a selected row of pixels by counting the number of pixels having an intensity level above a threshold value. The diameter of the liquid is controlled by stretch or squeeze actions on the liquid which result from relative motion between the unmelted and

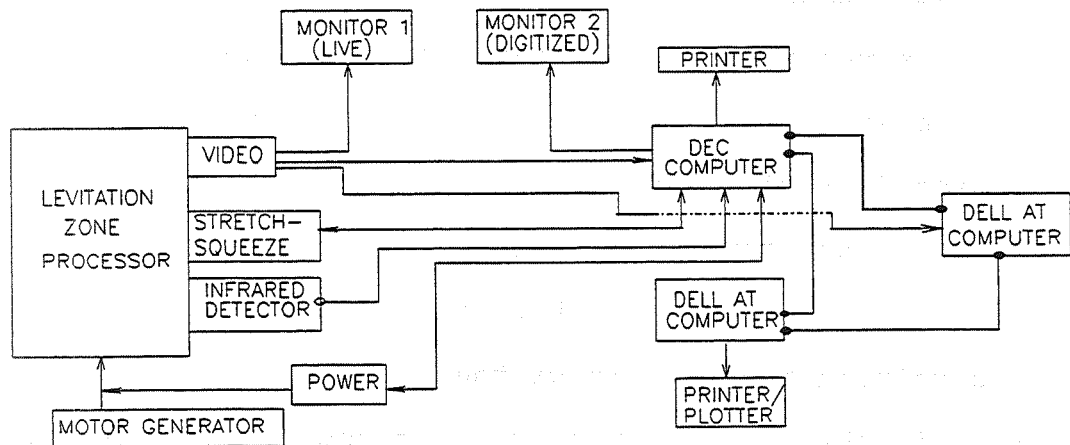


**Figure 20: Process control schematic.**

freezing portions of the ingot at opposite ends of the zone. The solid-liquid interface is determined by image analysis and held to a target position by controlling the induced power. Both the interface position and liquid diameter are held to their target values by proportional, integral (PI) control loops which cycle about 4 times per second.

In a typical run, the liquid zone is established manually and then transferred to computer control as the zone approaches steady state conditions. As the composition and therefore the temperature of the solidifying interface changes during directional solidification, the controller adjusts the power to maintain the position of the interface at the set point. The fact that this control action is independent of direct temperature measurements is important since temperature measurements have proven to be unreliable for process control for two reasons. First, the emissivity and melting temperature of the alloy are often unknown. Second, the emissivity at the surface of the ingot can change during processing due to the segregation of solid contaminants to the surface of the liquid zone. These solids subsequently deposit on the surface of the re-solidified ingot.

The control variables are interactive in that a change in one affects the others. For example, the melt record for NiAl-15Zr-15V (Figure 21) illustrates the interdependence

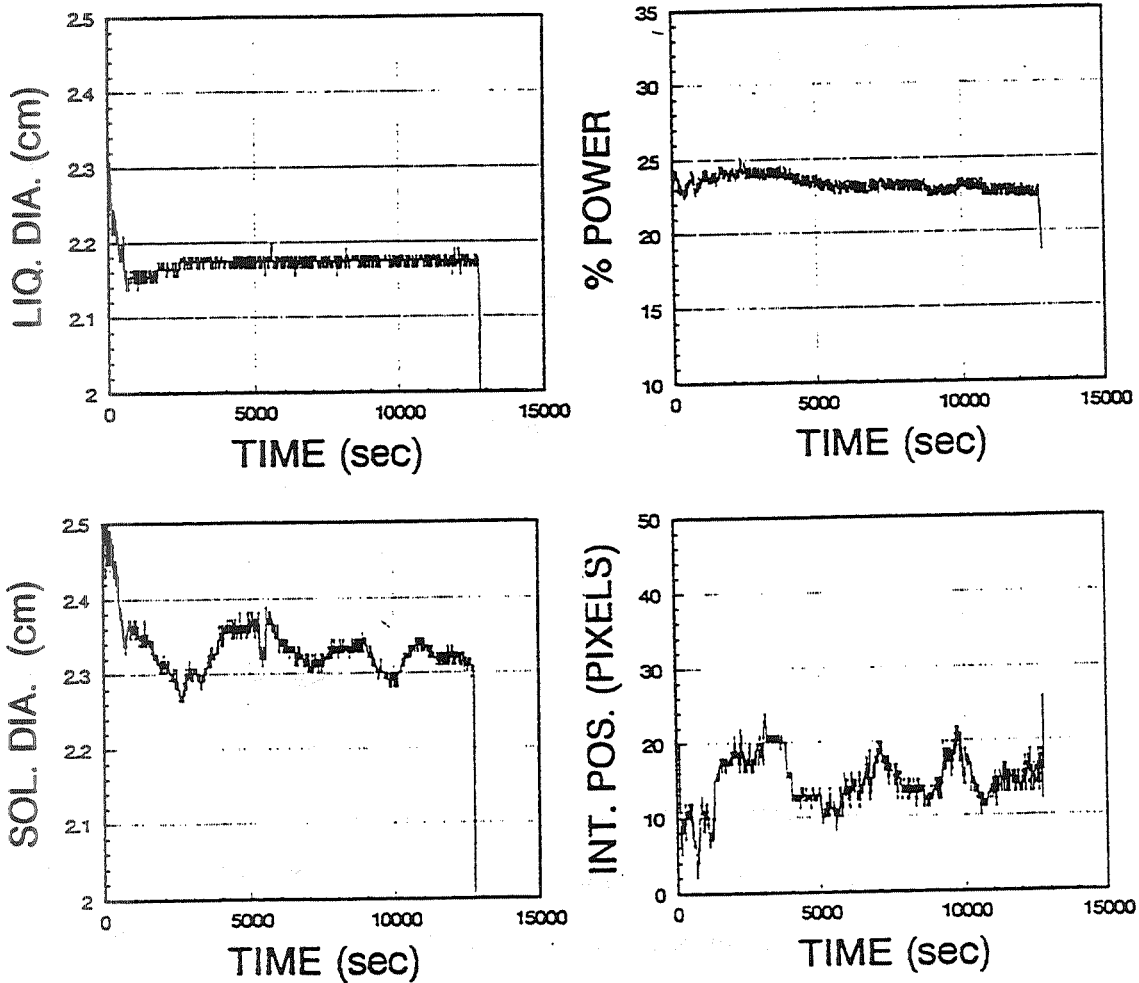


Figure 21: Melt record for NiAl-15Zr-15V. Shown are the relationship between key processing variables: liquid diameter, power, solid diameter, and interface position.

between liquid diameter, power, interface position, and solid diameter. The record shows that the liquid diameter was held constant. Nevertheless, the interface position varied due to a change in emissivity caused by impurity solids emerging at the surface of the liquid. This caused control actions to the power level in order to bring the interface position back to set point. The sum of these variations produced oscillations in the solid diameter.

The interdependence of the process variables creates a non-linear system. The ingot is an integral part of the power supply; it is essentially the core in a secondary coil of a transformer. As such, changes in the resistivity or dimensions of the ingot are equivalent to changing the properties of the transformer, i.e., the power transferred. Larger ingot diameters increase both the power input to the liquid zone and the levitation forces at a constant current setting. Higher emissivity results in greater local heat loss, requiring higher power levels to maintain a constant interface position within the electromagnetic field. The natural curvature of the zone at the solid-liquid interface depends on the surface tension relationships and viscosity of the liquid. This curvature can affect the process control since the distance between the measured liquid diameter and the freezing interface position determines how tightly control actions and system response are coupled.

The liquid diameter is measured at a selected pixel row, but the position of the interface may vary. As the distance between the interface and liquid diameter pixel line increases, the measured liquid diameter decreases due to the natural curvature of the zone. This causes a stretch/squeeze control action. This control action results in an increase in the liquid diameter at the interface and therefore an increase in the solid diameter. As the length of the liquid zone increases, its shape changes. This change affects the power by changing the coupling between the induction coil and the ingot. Thus, optimum control would maintain a constant separation between the freezing interface position and the liquid diameter control line of the image. Tighter control is afforded by a smaller separation distance between the interface and the diameter control line. However, if the liquid diameter control line lies below the freezing interface, the control system is unstable.

### **3. BEND TESTING**

Four-point bend tests were used to determine the room temperature fracture toughness [2]. Specimens were electrical discharge machined from the directionally solidified ingots. A single, straight notch (2 mm) was cut

by a low speed diamond saw in the specimen (nominally 4 x 6 x 40 mm) leaving a ligament approximately 4 x 4 mm. A fatigue crack was not initiated at the root of the notch prior to testing. The longitudinal axis of the specimens were parallel to the ingot axis. Therefore, the notch was cut transverse to the ingot growth direction. The nominal strain rate was  $1.4 \times 10^{-4} \text{ s}^{-1}$ . The K-calibration factor for pure bending was used to calculate the fracture toughness values [4]. The fracture toughness values correspond to "steady state", small scale bridging conditions.

#### 4. MICROSCOPY

Optical, scanning electron and transmission electron microscopy (TEM) were used to characterize the microstructures and dislocation structures of the processed ingots. Optical microscopy was used to characterize the general microstructure of the eutectic alloys before and after directional solidification. General metallographic preparation consisted of standard grinding and polishing techniques followed by etching with 5% HF-5% HNO<sub>3</sub>-90% H<sub>2</sub>O by volume.

Transmission electron microscopy was performed by X.F. Chen, a visiting scholar from Shanghai Jiao Tong University,



P.R. China. The TEM foils of CELZ processed eutectic alloys were taken from the free-ends of the bend specimens, while foils of bend-tested material were taken as close as possible to the fracture surface. The TEM specimens were prepared by sectioning with a low-speed diamond saw, followed by grinding and then electropolishing in a solution of 6.2% perchloric acid, 10% Butylcellosolve, 13.8% water, and methanol (by volume) at 40V and 10°C.

Determination of the Burgers vectors of the slip dislocations was accomplished using the invisibility criterion  $g \cdot b = 0$ . The lattice parameter mismatch was determined from selected area diffraction patterns.

Scanning electron microscopy was used to characterize the fracture surfaces of each alloy. A Cambridge, Stereoscan 120 scanning electron microscope (SEM) was used to examine fracture surfaces under back scatter and secondary electron modes. Phase constitutions were determined using a Cambridge, Stereoscan 360 SEM in conjunction with an energy dispersive X-ray system (EDS). The ZAF method was used to correct for atomic number, absorption, and fluorescence effects. Carefully prepared standards ensured the best accuracy possible with this technique.

## 5. ELEVATED TEMPERATURE TESTING

Elevated temperature testing was performed at NASA Lewis Research Center, Cleveland, OH, primarily under the direction of Dr. J.D. Whittenberger. Cylindrical compression samples 5 mm diameter and 10 mm in length were electrical discharge machined from the processed ingots. Compression tests were performed at 1300 K. Testing was performed in air as a secondary test for oxidation resistance. If a material exhibited promising strength at this temperature, additional testing was performed in the 1200 to 1400 K range. Both constant load and constant velocity test conditions were used. Constant load conditions were used for strain rates less than  $10^{-7} \text{ s}^{-1}$  in a lever-arm creep machine. Constant velocity conditions were generated using a screw driven universal machine for strain rates greater than  $10^{-7} \text{ s}^{-1}$ . Comparison of the stress-strain rate data between these two techniques show excellent correlation.

... ..

... ..

... ..

... ..

**REFERENCES**

- [1] W.G. Pfann, Zone Melting, John Wiley and Sons., New York, NY, (1958).
- [2] E.C. Okress et al., JAP, 23(1952)545.
- [3] A.J. Hatch, JAP, 36(1965)44.
- [4] W.F. Brown and J.E. Srawley, in Plain Strain Crack Toughness Testing of High Strength Metallic Materials, ASTM Special Publication No. 410, ASTM, Philadelphia, PA (1966)13.

**PART IV: Nial RESULTS**

## 1. INTRODUCTION

Discrepancies in the reported mechanical properties of NiAl are often attributed to variations in material purity. One of the unique advantages of the CELZ process is the high purity attainable in the resulting ingots. For this reason, careful characterization of CELZ processed NiAl has been performed at the University of Tennessee and NASA Lewis Research Center (NASA-LeRC), as well as other universities and corporate laboratories. The results indicate that the purity of these ingots is consistently higher than that of NiAl produced by commercial processing techniques. Further characterization has contributed significantly to understanding the strain aging phenomenon observed for commercial purity NiAl.

In all, the yield strength, critical resolved shear stress, percent elongation, 1100-1300 K creep strength, and fracture toughness of CELZ processed NiAl have been determined and compared to binary NiAl and NiAl-based alloys produced by other techniques. Experimental results are presented in this chapter and are subsequently used as the baseline for comparison with the in-situ composites discussed in later chapters.

## 2. EXPERIMENTAL PROCEDURE

Ingots of NiAl and NiAl(0.1Zr) have been directionally solidified using the CELZ process described previously. Typically, the growth rate is 2 cm/hr with the interface rotating at 75 rpm. For [011] seeded crystals, the nominal growth conditions are 1.9 cm/hr at 100 rpm. Room temperature fracture toughness, creep strength in the range of 1100 to 1300 K, and yield strength as a function of temperature were determined for high purity single crystals at the University of Tennessee and NASA-LeRC. Further characterization was performed elsewhere as referenced.

## 3. RESULTS

### 3.1 Processing

A typical data record for NiAl is shown in Fig. 22. Figures 23 and 24 show typical ingots grown from a polycrystalline precursor ingot and a [110] seed crystal, respectively. The seed crystal was provided by NASA-LeRC. As shown in Fig. 24, a small amount of contamination came to the surface of the seeded crystal during processing. However, the amount of contamination decreased as the run progressed, Fig. 24. Since this type of surface phase is not observed on the un-seeded crystals, the contamination is

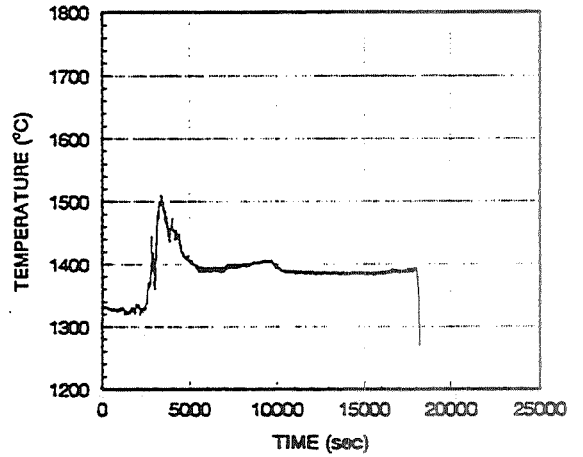
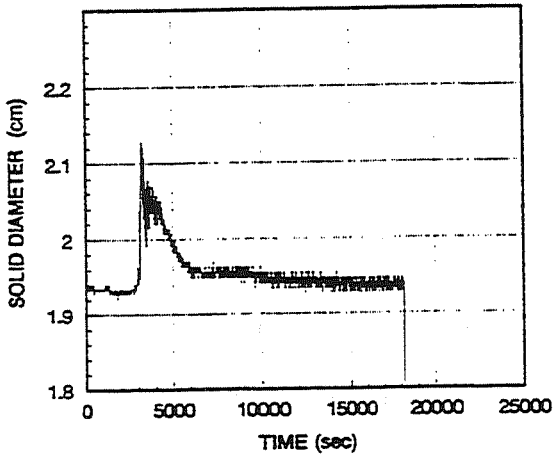
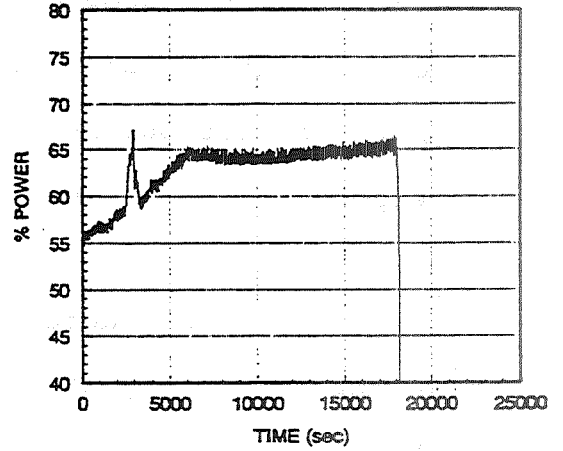
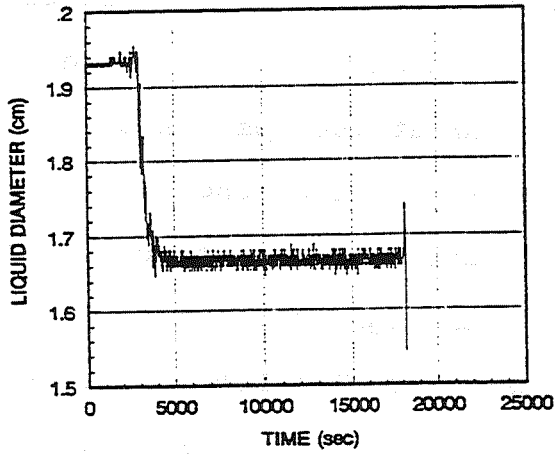


Figure 22: Typical melt record for binary HP-NiAl.



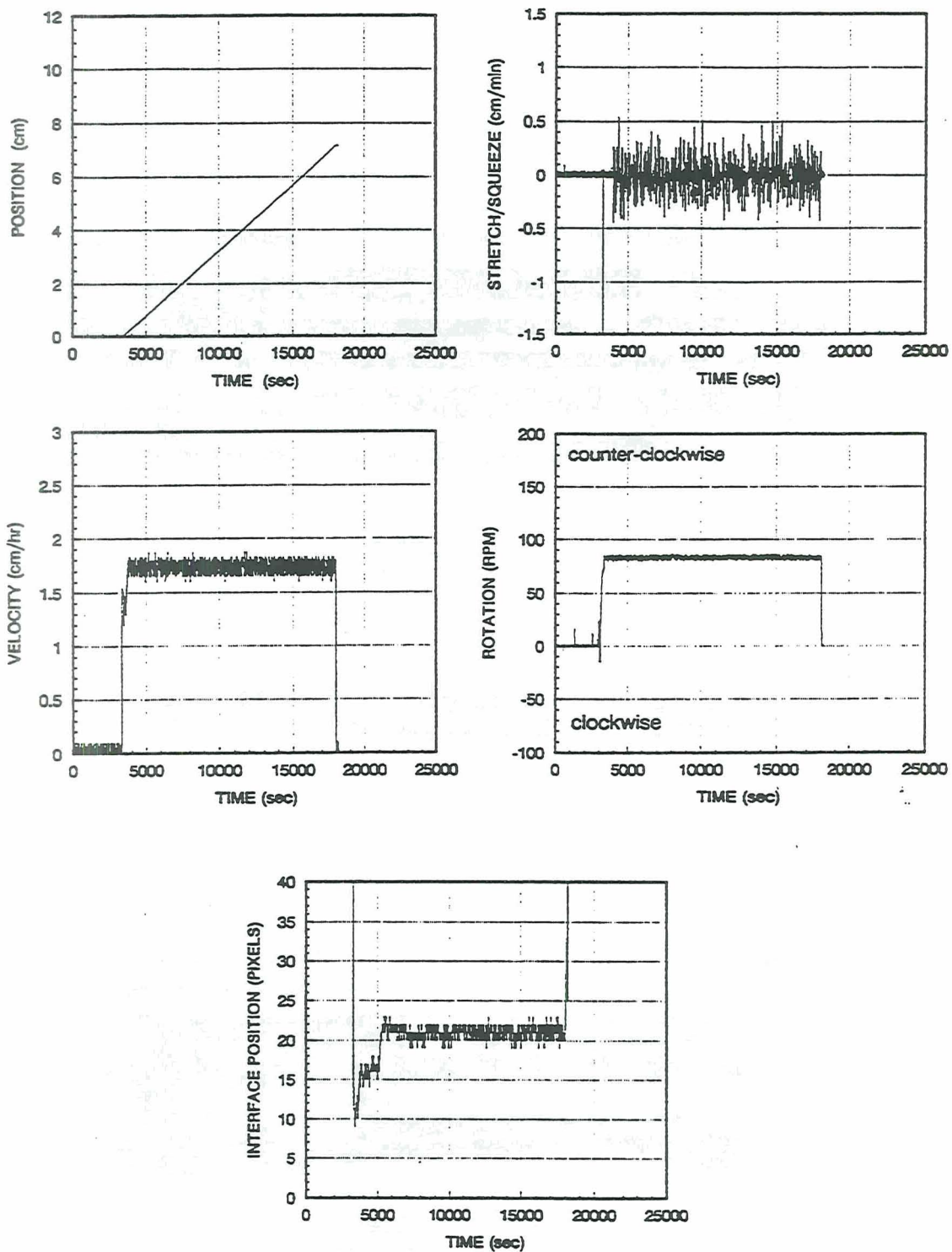
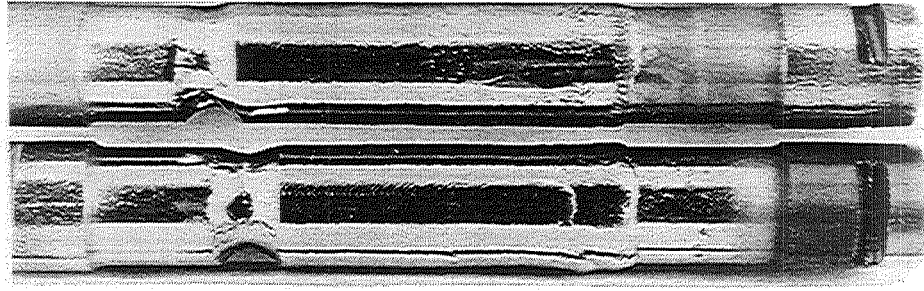


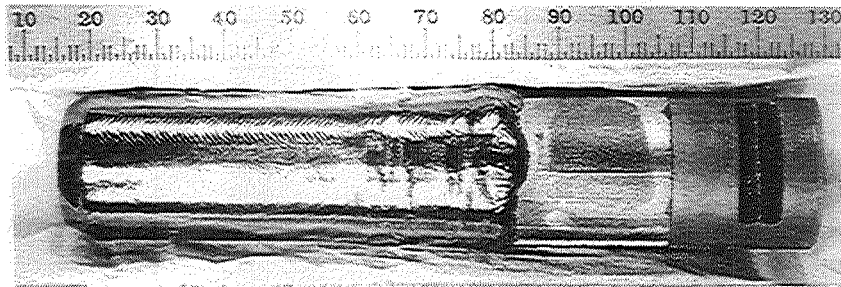
Figure 22 continued.

C-2.



2cm

**Figure 23:** As-processed single crystal HP-NiAl grown from polycrystalline precursor, orientation near  $\langle 123 \rangle$ .



Growth Direction

**Figure 24:** As-processed single crystal HP-NiAl grown from  $\langle 110 \rangle$  seed crystal.

presumed to originate from the seed crystal. This was observed on all seeded crystal growing runs. The seed crystal is partially melted during the initial start-up, so contamination in the zone would be highest at the beginning of the run and would be expected to deplete as solidification progresses.

The addition of 0.1 atomic percent Zr to binary NiAl is intended to enhance the elevated temperature properties [1,2] and does not affect the melt characteristics of the alloy. Establishing the initial zone is equally difficult for both the binary and Zr-doped NiAl. This difficulty is primarily due to the high melting temperature, high thermal conductivity, and low density of the alloy.

The high thermal conductivity and radiation increase the heat loss, increasing the power required for further melting. On the other hand, lower power levels would be adequate for levitation of the liquid zone because of the low density. Since the high power level required to melt the ingots leads to higher lift from the electromagnetic field of the induction coil-eddy current plate assembly, the liquid is often observed to over-levitate.

A change in coil geometry will affect the power input and lift generated at a given power setting. In lieu of expensive alterations to the coil geometry, the NiAl precursor ingots were down sized by grinding to 2.25 cm

(0.900 in), from 2.54 cm (1.00 in). This dimension was chosen from the steady state diameter of a successful processing run and provides a zone shape amenable to tight process control using the existing coil geometry. Grinding the ingots prior to directional solidification also helps to eliminate surface contamination which may have occurred during the initial drop casting operation used to prepare the precursor ingots.

The precursor ingots often contain a shrinkage pipe. Generally, this pipe is detrimental only during establishment of the initial zone. The ingot is initially cut into two pieces to allow for both thermal expansion of the assembly and volume expansion on melting. The first liquid to form is pushed to the center of the ingot and generally freezes, welding the two pieces together. Further melting begins to create the liquid zone, but the center of the ingot remains solid. This is the critical portion of the run for the NiAl ingots. It is within this manually controlled window that the vast majority of spills occur. When the center eventually melts, trapped gas in the pipe can blow the liquid out of the zone. Otherwise, the liquid may flow into the pipe by a combination of capillary action and pressure from the electro-magnetic field. The resulting zone diameter is much smaller and requires a much higher

power level to remain molten. Additional difficulties arise due to uneven melting of the precursor ingots.

Even though NiAl is a congruent melting phase, the melt line is rarely smooth during the initial stages of a run. Instead, the solid/liquid interface appears to melt in chunks, leaving fingers of unmelted NiAl protruding into the liquid zone. These fingers act as heat radiators, requiring an increase in power to continue melting. The power spike observed in Fig. 22 is a result of this phenomenon. Timing is critical at this point; the power must be decreased immediately upon melting of the fingers due to both the volume expansion on melting and concurrent decrease in heat loss. As shown in Fig. 22, this occurs in a matter of seconds or less. The increase in zone diameter will itself increase the power input to the ingot by more efficient coupling between the coil and the ingot. Together with the decrease in heat loss, the volume of liquid increases rapidly and must be controlled in order to prevent a spill.

Once the zone is established and computer control is engaged, the remainder of the run very rarely requires manual intervention. The melt line at this stage is very uniform. The solid-liquid interface of a single crystal often develops cusps at the crystallographic poles of the ingot. The number of cusps is an indication of the crystal orientation. However, prominent cusps can also form at high

angle grain boundaries. These cusps do not interfere with process control because the input parameter values used for control are averaged over at least 6 of the most recent data points.

The image-based control system is able to adjust the power to correct for changes in heat flow independent of temperature measurements. The heat flow varies with the position of the zone along the length of the ingot. Changes in the emissivity of the surface due to precipitation of contaminant phases from the liquid also cause the heat flow to vary. For the binary NiAl, changes in heat flow and interface temperature due to compositional changes in the zone are not a problem. Changes due to emissivity are generally the most severe.

The dimensional control possible using the image-based control system developed at the University of Tennessee [3-5] is very good, Figs. 23 and 24. Under tight control of a clean ingot, the tolerance approaches the resolution of the optical system. The pixel size determines the resolution and for the current system is approximately 0.08 mm. Hence, the solid diameter of NiAl ingots is often controlled to a tolerance of  $\pm 0.08$  mm.

### 3.2 Microstructure

The typical microstructure of an NiAl ingot processed from a polycrystalline precursor ingot consists of a single crystal between  $\langle 100 \rangle$  and  $\langle 123 \rangle$ , perhaps with a surface grain or two. The  $[110]$ -seeded crystals are in fact oriented along the  $[110]$  direction. However, the preferred growth direction is  $[001]$  for NiAl. The difference between the observed axis of the ingots (determined by Laue back-reflection) and the preferred growth direction is most likely due to the characteristic curvature of the solid/liquid interface in the CELZ process as discussed in PART III (experimental procedure).

This curvature is a function of the power input, thermal conductivity, emissivity, and melting temperature of the alloy. The power input is deeper than in most zone processes because the frequency used in the CELZ process is lower, 10 kHz. The power level drops to  $1/e$  of the surface at a depth of nearly 2.5 mm, much deeper than for frequencies in the mega-Hertz range. Any material property or process condition that affects heat flow will alter the curvature of the interface as well.

### 3.3 Purity

Table 4 is a summary of chemical analyses performed on the vacuum induction melted precursor ingots (VIM), CELZ processed NiAl (HP-NiAl), and of commercial purity (Bridgman processed) NiAl (CP-NiAl). The HP-NiAl material is significantly lower in interstitial contamination as compared to CP-NiAl. The O and C levels are lower by an order of magnitude [6-8]. The level of substitutional impurities (primarily Si) in HP-NiAl is less than one half that in CP-NiAl [7,8]. Furthermore, a study using an atom probe field ion microscope found at least an order of magnitude difference in the number of contaminant related precipitates between HP and CP material [9]. In fact, only one precipitate was observed in that study for the HP-NiAl material.

The source of the Si contamination in the CELZ material is the crucible used to cast the precursor ingots. For the commercial purity material, the crucible used to contain the ingot during directional solidification is partially silica, which increases the time of exposure and therefore chemical interaction with the silica compared to the CELZ ingots. Again, higher purity results from the containerless nature of the CELZ process. Further evidence of purity differences resulting from the different processing techniques is found in the mechanical property data.



Table 4: Purity levels in HP and CP NiAl (atomic percent).

Alloy	Ni <sup>a</sup>	Al <sup>a</sup>	Si <sup>b</sup>	O <sup>c</sup>	N <sup>c</sup>	Cd	Sd	ref.
VIM	-	-	-	0.0131	0.0014	0.0106	0.0041	[10]
HP	-	-	-	0.0034	0.0011	<0.0021	<0.0021	[10]
CP	50.09	49.70	-	0.055	<0.0009	0.0147	<0.0007	[6]
HP	49.91	50.07	-	0.003	<0.0009	0.0043	<0.0007	[6]
CP	51.7	48.1	0.20	0.0020	0.0040	0.0300	-	[8]
CP	50.35	49.46	0.15	0.0092	<0.0031	0.0169	<0.0007	[7]
HP	50.18	49.76	0.06	<0.0027	<0.0031	<0.0036	<0.0013	[7]
CP	-	-	-	0.0091	0.0015	0.0210	<0.0007	[11]
HP	-	-	-	0.0023	0.0005	<0.0018	0.0009	[11]

<sup>a</sup> Analysis performed using wet chemistry/titration,  $\pm 1\%$ .

<sup>b</sup> Analysis performed on an Ultraviolet/Visible Spectrophotometer, Shimadzu, Model UV-160,  $\pm 10\%$ .

<sup>c</sup> Analysis performed on a Simultaneous N/O Determinator. LECO Corp. Model TC-136 or Model TC-436,  $\pm 10\%$ .

<sup>d</sup> Analysis performed on a Simultaneous N/O Determinator. LECO Corp. Model TC-244,  $\pm 10\%$ .

### 3.4 Yield Strength and CRSS

The room temperature yield strength of NiAl has been measured for various heat treated conditions, purity levels, and grain sizes (including single crystals). Typical stress-strain curves for tensile and compression testing of NiAl are shown in Fig. 25 [7]. Table 5 is a summary of the yield strength of HP-NiAl in various heat treated conditions. The 47% decrease in yield stress resulting from annealing and water quenching is due primarily to the reduction in thermal vacancy concentration [7]. The hardening effect of thermal vacancies is 900 MPa/atomic % [12,13]. Vacancy concentrations of 0.5 to 1% are possible in NiAl quenched from intermediate temperatures [2,14-16] and up to 2% is possible near the melting temperature [17]. A vacancy concentration of only 0.11% is required to produce the observed decrease in yield strength, which is within the possible range of values. A proportionate decrease in yield strength occurs for CP-NiAl further implicating vacancies as the primary source of the observed yield drop. Differences between the yield strength of HP and CP-NiAl in the same heat treat condition are attributed to their purity levels and illustrate the importance of measuring these levels for a clear interpretation of the data.

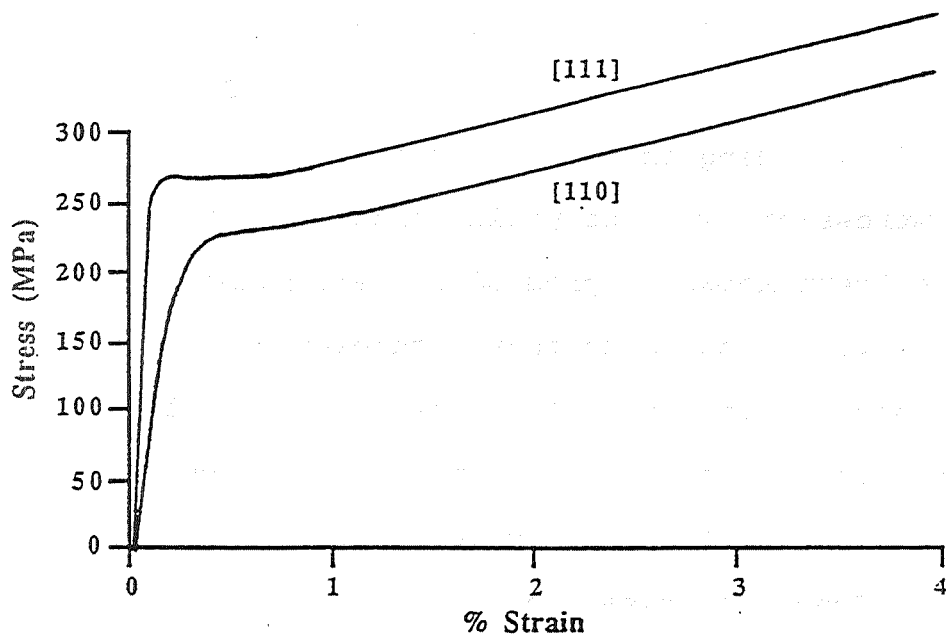
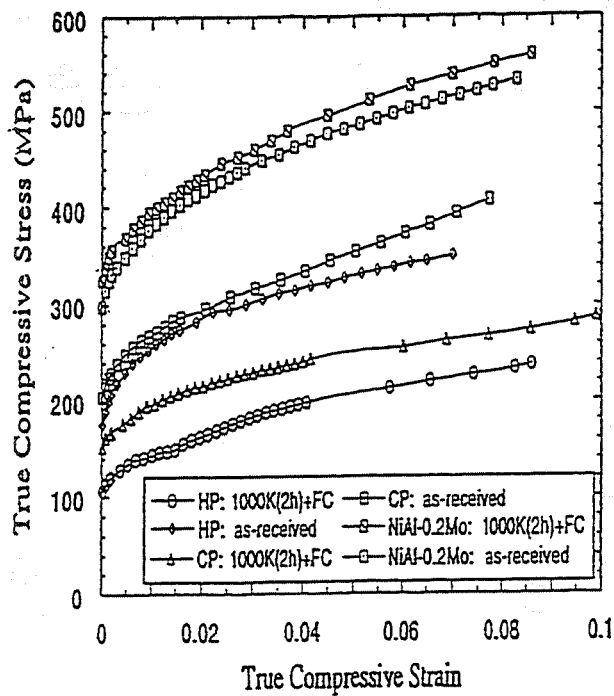


Figure 25: Compressive stress-strain curves for HP-NiAl, CP-NiAl, and NiAl-0.2Mo single crystals [7].

**Table 5: Yield strength data for binary NiAl at 300 K (MPa).**

HP-NiAl	CP-NiAl	Condition	Orient.	REF.
213 ± 14	233.1 ± 21.0	as-grown	<123> C	[7]
126 ± 6	174.7 ± 8.9	1000 K 2hr/sc	<123> C	[7]
112 ± 8	-	1000 K 2hr/wq	<123> C	-
230.4	-	1573 K 3hr/sc	near<123> T	-
231.6	-	1573 K/3hr, 473K/1.5hr/ fc	near<123> T	-
162	272	as-extruded	polycrysta l T	[6]
98	191	1100 K 2hr/fc	polycrysta l T	[6]

sc slow cooled

fc furnace cooled

wq water quenched

C - compression test

T - tensile test

A yield point is often observed for CP-NiAl especially after specific heat treatments [8,18-22]. On the other hand, yielding is continuous for HP-NiAl in tension and in compression, with no yield point evident even after the heat treatment known to produce a yield point in CP-NiAl. This observation suggests that a threshold level of contamination exists between that of HP-NiAl and CP-NiAl which dictates the yield behavior of the material. Such behavior is reminiscent of strain aging in low carbon steels [23,24].

Specific investigation into the yield behavior of NiAl has produced varied evidence of strain aging [25] including yield points and serrated yielding [26-31], strain rate sensitivity minima [32,33], yield stress plateaus as a

function of temperature [34], and flow stress transients on changes in strain rate [33,35]. Other investigations include pre-strain effects and the effects of Mo, N, and C doping on the yield behavior of NiAl [7,25].

Recent results indicate that C is responsible for the yield point behavior often observed for CP-NiAl [7,8,25]. The increase in yield strength per atomic percent C may be estimated from the data for CP and HP-NiAl and is approximately 2500 MPa/at% [7]. This is in agreement with the data of George and Liu [36] where the effect was estimated at more than 1700 MPa/at%. More in depth review of this phenomenon can be found elsewhere [2,7,11,18].

In general, as the purity of NiAl increases, the yield strength decreases. Another indication of purity level is the critical resolved shear stress (CRSS). Several investigations report values for the CRSS of CP and HP-NiAl [7,11,37,38]. Table 6 lists the reported CRSS values, most are for the  $\langle 100 \rangle \{011\}$  slip system. The CRSS is lowest for HP-NiAl in each heat treated condition. It should be pointed out that the results from the micro disc bend tests [37] are for CP-NiAl and HP-NiAl in different heat treatment conditions. A lower CRSS for HP-NiAl would be expected after the same heat treatment given the CP-NiAl. In fact, from compressive yield strength data, the CRSS of HP-NiAl is roughly 25% lower than that of CP-NiAl when compared under

**Table 6: Room temperature CRSS data (MPa) for NiAl.**

HP-NiAl	CP-NiAl	Specimen	System	Condition	REF.
$96.5 \pm 6.6$	$105.9 \pm 10$	<123>	<001>{110}	as-received	[7]
$57.2 \pm 2.6$	$79.4 \pm 4.0$	<123>	<001>{110}	1000K/2h/fc	[7]
$50.9 \pm 3.4$	-	<123>	<001>{110}	1000K/2h/wq	[6]
65.0	83.6	near<123>	<100>{001}	1588K/50h/fc	[11]
84.3	-	<110>	<100>{010}	as-received	[37]
-	81.2	<110>	<100>{010}	1589K/50h/fc	[37]
-	$109 \pm 0.4$	<110>	<100>{010}	1589K/50h/fc	[18]
-	145	<110>	<100>{010}	*	[39]

fc furnace cooled  
wq water quenched

similar conditions. The as-received conditions are not comparable because the CELZ and Bridgman techniques differ thermally and are therefore likely to differ in vacancy concentration.

The effects of prestraining on yield strength have been determined for polycrystalline CP and HP-NiAl [6]. The effect of prestraining on CP-NiAl is to eliminate the yield point. The HP material yields continuously both before and after the prestrain pressurization. The yield point returns for the prestrained CP-NiAl after a subsequent anneal (1100 K/3h/fc). The behavior of C-doped NiAl is similar to that of CP-NiAl. Nitrogen doped NiAl is similar to HP-NiAl because of the lower C concentration in that alloy [6].

The compressive yield strength of  $\langle 001 \rangle$  NiAl is shown as a function of temperature in Fig. 26 at a nominal strain rate of  $1.4 \times 10^{-4} \text{ s}^{-1}$ . The upper plateau extends from room temperature to approximately 625 K at nearly 1400 MPa. The precipitous drop is a result of the change in deformation mechanism which occurs near the DBTT. The DBTT of HP-NiAl is approximately 500 K, essentially the same as for CP-NiAl, based on Arrhenius plots of compressive data [7]. Together, the low resolved shear stress of the hard oriented crystals for the  $\langle 001 \rangle \{110\}$  system and the high CRSS for  $\langle 111 \rangle$  and  $\langle 110 \rangle$  systems result in a high yield strength. The yield strength is maintained until dislocation climb becomes

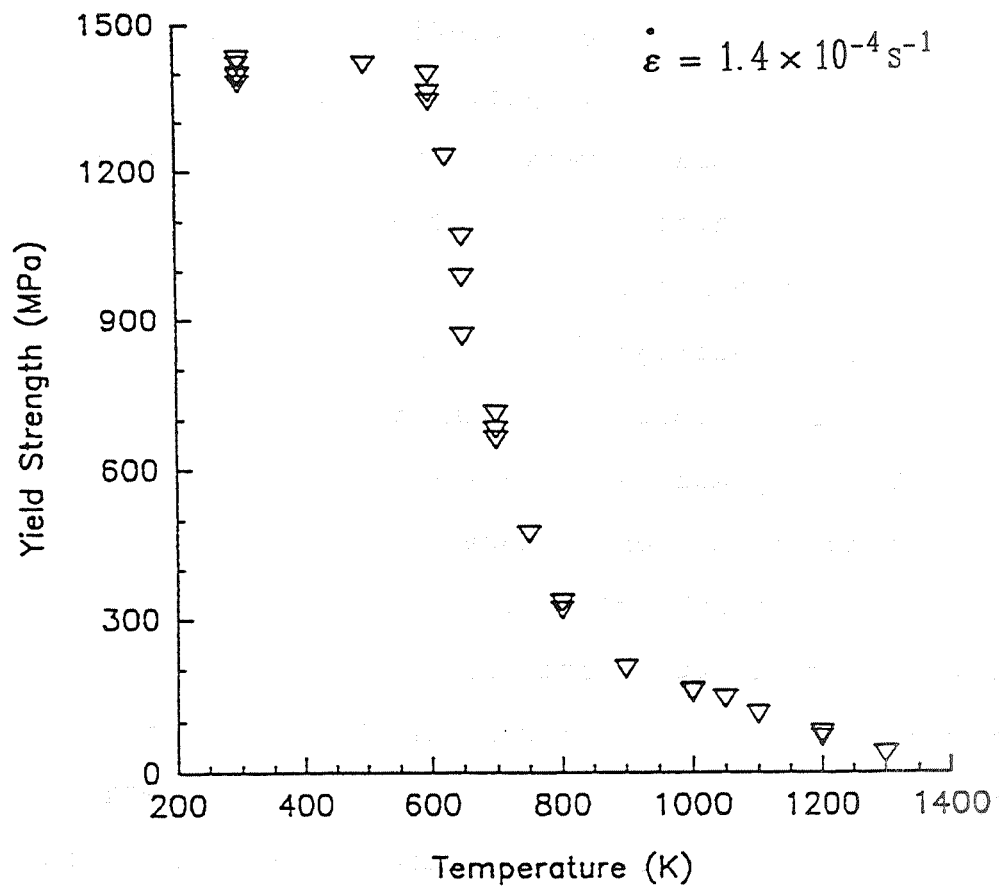


**Figure 26:** Yield strength in compression as a function of temperature for <001> HP-NiAl.



active near 600 K. Soft oriented crystals do not exhibit this plateau and yield at much lower stress levels, Fig. 26. Above 900 K, the yield strength of <001> crystals is very near that of soft oriented crystals [40]. Deformation in this temperature regime is controlled by bulk diffusional processes.

### 3.5 Fracture Toughness and Ductility

The fracture toughness and ductility of single crystal HP-NiAl is higher than the previously reported values for binary NiAl of the same orientation, Table 7. The room temperature fracture toughness of single crystal <001> HP-NiAl is  $11.2 \text{ MPa}\sqrt{\text{m}}$  as determined by 4-point bending. Compared to  $8.3 \text{ MPa}\sqrt{\text{m}}$  for CP-NiAl of the same orientation [41], the HP material is approximately 35% higher in fracture toughness. It should be noted that the values reported by Hack et al. [8] are for double cantilever beam specimens and are therefore not directly comparable to the 4-point bend results reported here. In addition to their geometry, the orientation of the specimens are different. In contrast to the observed behavior of CP-NiAl [8], the fracture toughness of the HP material is independent of heat treatment.

Table 7: Room temperature fracture toughness.

$K_I$ (MPa $\sqrt{m}$ )		NOTCH DIRECTION	SPECIMEN ORIENTATION	HEAT TREAT COND.
HP-NiAl	CP-NiAl			
11.2	8.3*	<001>	<100>	1573 K 3h/ac- 473 K 1.5h/fc
-	4.4*	<001>	<110>	na
-	4 <sup>+</sup>	<110>	<110>	1589 K 48h/fc
-	11.6 $\pm$ 1.6 <sup>+</sup>	<110>	<110>	1589 K 48h/ac
-	15.6 <sup>+</sup>	<110>	<110>	1573 K 3h/ac
-	2.8 <sup>+</sup>	<110>	<110>	1573 K 3h/ac- 473 K 1.5h/sc
9.6 $\pm$ 2.9	-	$\perp$ <123>	<123>	1573 K 3h/oq
6.3 $\pm$ 2.1	-	$\perp$ <123>	<123>	1573 K 3h/oq- 473 K 1.5h/fc

\* no heat treatment specified [41]

+ Double cantilever beam test [8], not 4-point bend.

The tensile ductility of HP-NiAl is 4.7% which is on the order of Fe-doped NiAl [42], suggesting that a gettering effect is responsible for the increase in ductility of the doped alloy. The ductility of CP-NiAl of the similar orientation is 1% [43]. Based on the yield strength data for CP, HP, C-doped, and N-doped NiAl, it appears that carbon is responsible for the lower ductility of the CP-NiAl. However, the effect of Si contamination can not be ignored since an order of magnitude difference in precipitate concentration has been observed between HP and

CP-NiAl [9]. The effect of these precipitates has been estimated to increase the CRSS by approximately 13 MPa [9]. An effect on the ductility would also be expected, but has not been addressed directly. The dependence of fracture toughness on orientation can be explained by resolving normal stress on the cleavage plane [41]. The cleavage plane for NiAl is {110}. Figure 27 shows the dependence of fracture stress on specimen orientation [41].

### 3.6 Creep Strength

The elevated temperature behavior of HP-NiAl has been determined over a range of 1100 K to 1300 K. At 1300 K, 1% true strain, and a strain rate of  $1 \times 10^{-6} \text{ s}^{-1}$ , the creep strength is 19.5 MPa. The behavior can be represented by the temperature compensated power law equation:

$$\dot{\epsilon} = (0.16)\sigma^{5.75} \exp\left(\frac{-314.2}{RT}\right) \quad 1100 - 1300 \text{ K}$$

where the activation energy for deformation is 314.2 kJ/mol, T is the absolute temperature in K, R is the gas constant (8.314 J/mol-K), and the stress exponent, n, is 5.75 [2]. The stress exponent suggests that creep is controlled by dislocation climb in this temperature regime. The activation energy for creep deformation in NiAl is within

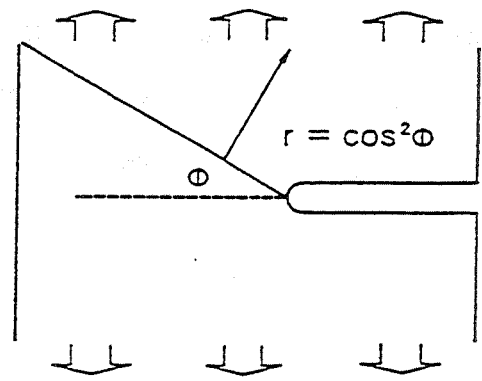
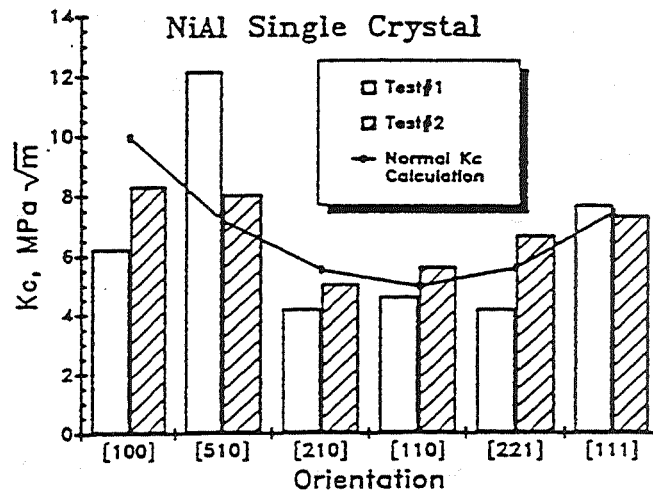


**Figure 27:** Fracture toughness of NiAl single crystals as a function of orientation [41].

the range of values for diffusion in NiAl [40]. In fact, Sauthoff [44] has determined that subgrains are formed in NiAl during creep deformation as expected for climb controlled creep. Hence, the behavior is similar to that of disordered metals. This data serves as the baseline for comparison with the eutectic alloys discussed in later sections.

#### 4. SUMMARY

The purity level of HP-NiAl is higher than that of commercially processed NiAl. The specific interstitial contaminant that appears to be responsible for the yield point behavior of CP-NiAl is carbon. The level of carbon is up to an order of magnitude lower for CELZ processed material as compared to Bridgman processed NiAl. The lack of a yield point in HP-NiAl is consistent with this analysis. The primary substitutional contaminant is Si which in HP material is generally half that of CP-NiAl. Overall, the mechanical property data are consistent with the higher purity of the HP material. The yield strength and CRSS are lower for the higher purity material under similar specimen treatments and testing conditions. The room temperature tensile ductility is comparable to Fe-doped NiAl and is the highest of any binary NiAl material produced

to date (4.7%). The fracture toughness is  $11.2 \text{ MPa}\sqrt{\text{m}}$ , also the highest of any NiAl in the 473 K annealed condition. The creep behavior is dislocation climb controlled with a stress exponent of 5.75. The activation energy for creep deformation (314 kJ/mol) is on the order of that for diffusion in NiAl.

**REFERENCES**

- [1] C.A. Barret, *Oxid. Met.*, 30(1988)361.
- [2] R.D. Noebe, NASA Tech. Memo. 106534 (1994).
- [3] D.R. Johnson, NASA Contractor Rep. 195333 (1994).
- [4] R.D. Reviere, Master's Thesis, University of Tennessee, Knoxville, (1989).
- [5] R.D. Reviere, B.F. Oliver, and D.D. Bruns, *Mat. Manf. Proc.*, 4(1989)103.
- [6] M.L. Weaver, R.D. Noebe, J.J. Lewandowski, B.F. Oliver, and M.J. Kaufman, *Mater. Sci. Eng.*, accepted for publication(1994).
- [7] M.L. Weaver, M.J. Kaufman and R.D. Noebe, *Scripta Metal. Mater.*, 29(1993)1113.
- [8] J.E. Hack, J.M. Brzeski, and R. Darolia, *Scripta Metal. Mater.*, 27(1992)1259.
- [9] A.J. Duncan, M.J. Kaufman, and M.K. Miller, *Appl. Surf. Sci.*, submitted(1994).
- [10] D.R. Johnson, S.M. Joslin, B.F. Oliver, R.D. Noebe, and J. D. Whittenberger, in "First International Conference on Processing Materials for Properties", H. Henein and T. Oki, eds., TMS (1993)865.
- [11] K. Kitano, T.M. Pollock, and R.D.Noebe, *Scripta Met. Mater.*, submitted(1994).
- [12] R.T. Pascoe and C.W.A. Newey, *Met. Sci. J.*, 2(1968)138.
- [13] T.G. Nieh, J. Wadsworth, and C.T. Liu, *Scripta Metall.*, 22(1988)1409.
- [14] H.L. Fraser, M.H. Loretto, R.E. Smallman and R.J. Wasilewski, *Phil. Mag.*, 32(1975)873.
- [15] W.J. Wang and R.A. Dodd, *Scripta Metall.*, 8(1974)237.
- [16] L.A. Kucherenko, N.M. Aristova, and VA. Troshkina, *Russ. J. Phys. Chem.*, 49(1975)14.
- [17] A. Parthasarathi and H.L. Fraser, *Phil. Mag. A*, 50(1984)89.



- [18] R.D. Field, D.F. Lahrman, and R. Darolia, in "High-Temperature Ordered Intermetallic Alloys IV", L.A. Johnson, D.P. Pope, and J.O. Stiegler, eds., MRS Symp. Proc. 213(1991)255.
- [19] R.W. Margevicius, J.J. Lewandowski, I.E. Locci, and R.D. Noebe, Scripta Metall. Mater., 29(1993)1309.
- [20] A.G. Rozner and R.J. Wasilewski, J. Inst. Met., 94(1966)169.
- [21] K.H. Hahn and K. Vedula, Scripta Metall., 23(1989)7.
- [22] R.W. Margivicius and J.J. Lewandowski, Acta Metall. Mater., 41(1993)485.
- [23] B.F. Oliver and E.W. Troy, Memoir. Scientifiques Rev. Metall., LXV, 15Juin(1968)39.
- [24] T.E. Tietz and W. Wilson, "Behavior and Properties of Refractory Metals", Stanford University Press, (1965)334.
- [25] M.L. Weaver, R.D. Noebe, J.J. Lewandowski, B.F. Oliver, and M.J. Kaufman, Mat. Sci. Eng., submitted(1994).
- [26] J.E. Hack, J.M. Brzeski, R. Darolia, and R.D. Field, in "High-Temperature Ordered Intermetallics V", I. Baker et al., eds., MRS Symp. Proc. (1993)1197.
- [27] E.P. Lautenschlager, D.A. Kiewit, and J.O. Brittain, Trans. AIME, 233(1965)1297.
- [28] R.W. Margevicius and J.J. Lewandowski, Scripta Metall. Mater., 25(1991)2017.
- [29] R.D. Field, D.F. Lahrman, and R. Darolia, in High-Temperature Ordered Intermetallics V, I. Baker et al., eds., MRS Symp. Proc. 288(1993)423.
- [30] J.M. Brzeski, J.E. Hack, R. Darolia, and R. D. Field, Mat. Sci. Engr., A170(1993)11.
- [31] C.T. Liu, E.H. Lee, E.P. George, and A.J. Duncan, Scripta Metall. Bater., 30(1994)387.
- [32] R.T. Pascoe and C.W.A. Newey, Metal Sci. J., 2(1968)138.
- [33] R.T. Pascoe and C.W.A. Newey, Metal Sci. J., 5(1971)50.

- [34] R.D. Noebe, R.R. Bowman, and M.V. Nathal, *Int. Mater. Rev.*, 38(1993)193.
- [35] M.L. Weaver, Progress Report, University of Florida, August 1 to September 15 (1993).
- [36] E.P. George and C.T. Liu, *J. Mater. Res.*, 5(1990)754.
- [37] Ha K. DeMarco and A.J. Ardell, in "High Temperature Ordered Intermetallic Alloys V", I. Baker et al., eds., *MRS Symp. Proc.* 288(1993)641.
- [38] D.R. Johnson, S.M. Joslin, R.D. Reviere, B.F. Oliver, and R.D. Noebe, in "Processing and Fabrication of Advanced Materials for High Temperature Applications-II", V.A. Ravi and T.S. Srivatsan, eds., *TMS* (1993)77.
- [39] R.J. Wasilewski, S.R. Butler, and J.E. Hanlon, *Trans. AIME* 239(1967)1357.
- [40] R.D. Noebe, R.R. Bowman, M.V. Nathal, *Int. Mat. Rev.*, 38(1993)193.
- [41] K.-M. Chang, R. Darolia, and H.A. Lipsitt, *Acta Metall. Mater.*, 40(1992)2727.
- [42] R. Darolia, *J. Metals*, March(1991)44.
- [43] T. Takasugi, J. Kishino, and S. Hanada, *Acta Metall. Mater.*, 41(1993)1009.
- [44] G. Sauthoff, NATO ARW "Ordered Intermet.-Phys. Met. and Mech. Behaviour", Germany(1991).

**PART V: TWO-PHASE COMPOSITE ALLOYS**

## 1. LITERATURE REVIEW

### 1.1 Introduction

With a new baseline established for NiAl, the focus turned to improving upon the binary alloy. As pointed out in the literature review, limited success has been achieved through single phase alloying. In fact, the improvements observed for microalloying additions are nearly matched by the high purity NiAl grown by the CELZ process. Therefore, a multi-phase alloying approach was adopted as the best opportunity to improve upon the baseline NiAl. Specifically, the processing and characterization of in-situ composites were taken as the focus of the research.

In-situ composites provide a unique opportunity to incorporate a second phase within an NiAl matrix. A particular advantage is the thermodynamic compatibility of the constituent phases, since these composites are based on directional solidification of eutectic alloys. On the other hand, the melting temperatures are lower, the oxidation resistance must be re-evaluated, and the lack of specific phase diagram information on Ni-Al-X systems will require additional effort to locate potential eutectic alloys. However, several NiAl-based eutectic composites have been previously identified. These in-situ composites have been conventionally processed by a modified Bridgman technique. Experimental investigation has focused on phase composition

and microstructural characterization. Limited mechanical property data is available.

Sections 2 and 3 review the available information concerning NiAl-9Mo and NiAl-40V. Results of CELZ processing and subsequent characterization of the NiAl-9Mo and NiAl-40V alloys are presented in sections 4 and 5, respectively. Hyper-eutectic NiAl-Mo alloys are covered in less detail. Each alloy system is characterized separately and then all are compared with each other and the results of previous investigations in Section 6.

### 1.2. NiAl-9Mo

The majority of the data collected on NiAl-9Mo has been from directionally solidified ingots processed by a modified Bridgman technique. It has been pointed out that the reactive nature of this alloy in the liquid state makes contact with oxide-crucible materials a likely source of contamination. In fact, typical chemical analyses show that these ingots invariably contain silicon and oxygen at hundreds of parts per million. Carbon and nitrogen are found at considerably lower concentrations, i.e., tens of parts per million. The effects of these contaminants on mechanical properties are not explicitly known for either binary NiAl or the eutectic because of the difficulty in

producing sufficiently large ingots with better purity. The variation in interstitial contamination from ingot to ingot is difficult to control and typically has not been reported.

As shown in the 1073 K, NiAl-Mo phase diagram in Fig. 28, a two-phase field occurs between NiAl and Mo [1,2]. The binary eutectic occurs at 1778 K (1505°C) and 9 atomic percent molybdenum [1,2]. There is less than 0.1 a/o solubility for Mo in NiAl and approximately 5 a/o solubility of Al and Ni in Mo after a 24 hour homogenization treatment at 1723 K (1450°C) [3]. However, solubilities as high as 9 a/o Ni and Al have been observed after 500 hours at 1473 K (1200°C) [3]. Hence, the mechanical properties of the Mo rods may be expected to differ from that of pure molybdenum.

Some of the promising characteristics of the eutectic NiAl-9Mo are the uniformity of the rod spacing [1], the stability of the faceted molybdenum rods within the NiAl matrix, and the fault-free growth of the rods from the melt [4]. Further characterization has shown that the preferred growth direction is  $\langle 001 \rangle$  [1,4,5] with a cube-on-cube orientation relationship between the faceted rods and the NiAl matrix. The facet planes of the molybdenum rods are of the  $\{110\}$  type [1,4]. The volume fraction of the molybdenum rods has been estimated to be between 0.09 and 0.11 [1,4]. Ingots processed at growth rates of 0.6 cm/hr and 5.0 cm/hr have rod densities of  $11 \times 10^6$  and  $46 \times 10^6$

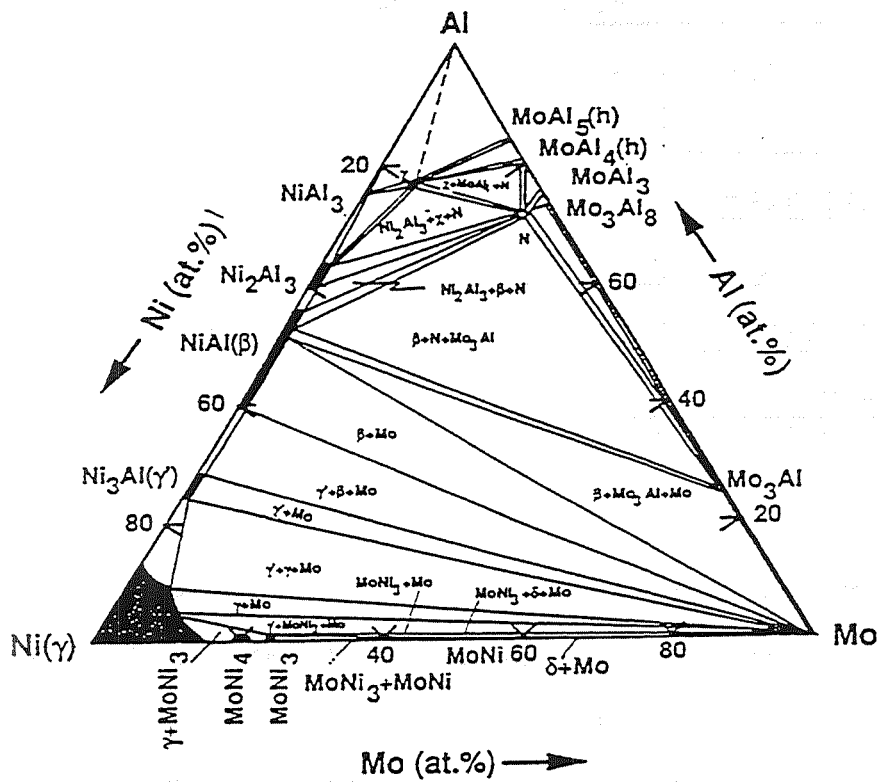


Figure 28: The Ni-Al-Mo ternary isotherm at 1073 K [2].

fibers/cm<sup>2</sup>, respectively [4]. Included in Table 8 is a summary of mechanical properties for NiAl-9Mo.

**Table 8: Summary of mechanical property data for binary eutectic alloys.**

ALLOY	$K_I$ (MPa√m)	Creep (MPa)	Hardness, $H_V$ (kg/mm <sup>2</sup> )	REF.
NiAl-9Mo	9.5 <sup>+</sup> 15*		-	[3, 6]
NiAl-12Mo	14 <sup>+</sup>		-	[3]
NiAl-40V	-		>400	[7]
NiAl(V)	-		356 ± 6	[7]
V(NiAl)	-		379 ± 20	[7]

<sup>+</sup> Arc melted button

\* Directionally solidified

Microstructural stability is excellent at high temperatures [4]. In fact, the faceted rods show no change in fiber density after more than 330 hours at 1673 K (1400°C) [4] and a negligible amount of coarsening after 100 hours at 1773 K (1500°C) [3]. In comparison, the cylindrical rods in the NiAl-34Cr eutectic are completely spheroidized after 160 hours at 1673 K (1400°C) [4]. The rapid spheroidization occurs by pinching off the cylindrical chromium-based rods at constrictions in the rod diameter. Variations in diameter occur during the directional solidification process [4]. The faceted molybdenum rods do



not pinch off because the interface between the rods and matrix is constrained to lie on {110} planes [4]. This constraint contributes to the fault-free nature of coupled growth in the NiAl-9Mo eutectic.

Data concerning the high temperature properties of NiAl-9Mo are very limited. The creep strength of aligned NiAl-9Mo has been shown to be superior to that of Rene 80 at high temperatures [5].

The room temperature fracture toughness of arc melted NiAl-9Mo is  $9.5 \text{ MPa}\sqrt{\text{m}}$  [3]. When directionally solidified, the fracture toughness increases to  $15 \text{ MPa}\sqrt{\text{m}}$  [3]. Hypereutectic, NiAl-12Mo, arc melted buttons have a fracture toughness of nearly  $14 \text{ MPa}\sqrt{\text{m}}$  [3]. The increment in fracture toughness over that of polycrystalline NiAl is  $2.8 \text{ MPa}\sqrt{\text{m}}$  for the eutectic alloy and  $7 \text{ MPa}\sqrt{\text{m}}$  for the hypereutectic alloy, Fig. 29 [3]. The increase in fracture toughness over binary NiAl has generally been attributed to crack bridging and crack trapping. Details of these mechanisms are discussed later.

### 1.3. NiAl-40V

The nickel-aluminum-vanadium system contains a large two-phase eutectic field between NiAl and V [4,8-9]. This lamellar eutectic occurs at 1633 K ( $1360^\circ\text{C}$ ) and 40 atomic

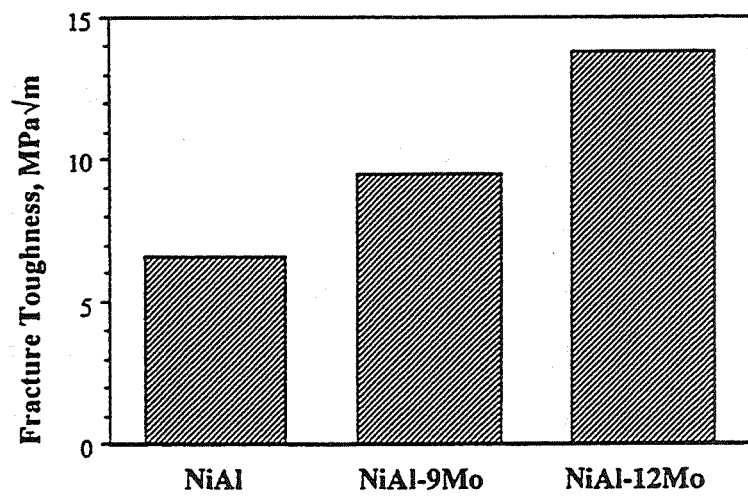
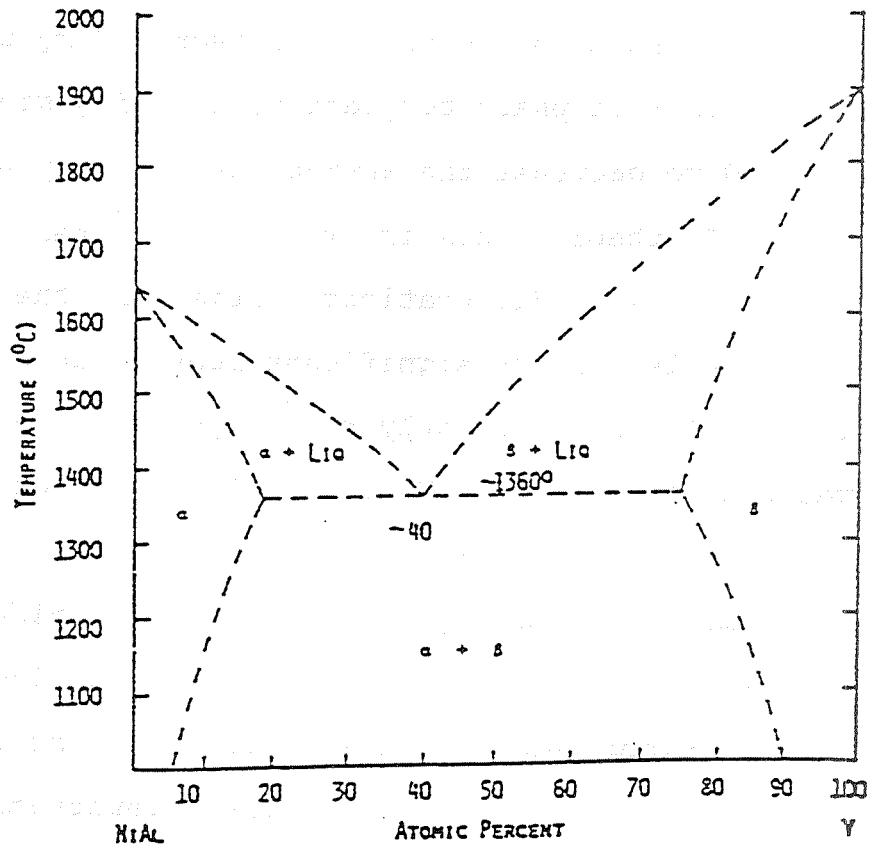
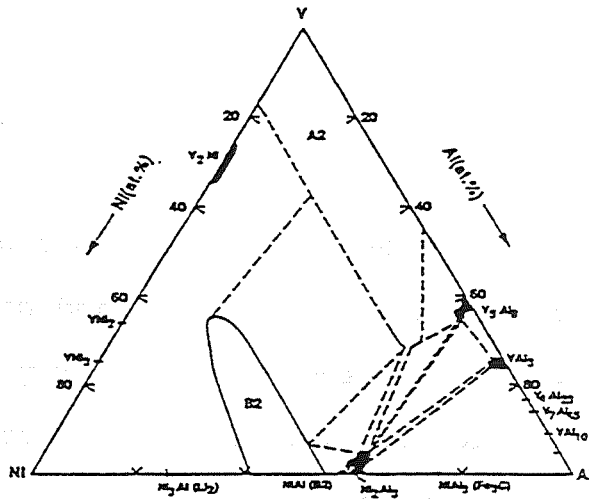


Figure 29: Room temperature fracture toughness for NiAl-Mo alloys [3].

percent V (Fig. 30) [4]. The volume fraction of the V-phase is approximately 0.40 [4]. A cube-on-cube orientation relationship exists between the vanadium lamellae and the NiAl matrix [7]. Included in Table 8 is a summary of the properties of NiAl-40V. Investigations of the NiAl-V system have focused on phase constitution and microstructure [4,7-9] with very limited mechanical property data.

Based on the high volume fraction of metallic phase and the lamellar structure, this eutectic is expected to exhibit significant improvement in toughness over binary  $\beta$ -NiAl. In addition to ductile phase toughening, alloying NiAl with V is predicted to decrease the anti-phase boundary energy of NiAl [10]. In theory, this is expected to permit deformation by  $\langle 111 \rangle$  dislocations, satisfying the Von Mises criterion and leading to significant improvements in tensile ductility [10]. However, only  $\langle 100 \rangle$  type dislocations are observed experimentally in NiAl(V) solid solution specimens after tensile testing at room temperature [10].

Experimentally, precipitation and solid solution hardening effects have been found to limit the increase in toughness of hypoeutectic alloys [7,10]. The solubility of V in NiAl is at least 14 at% at elevated temperatures [7]. The solubility decreases sharply for Al-rich NiAl and with decreasing temperature. Hence, precipitation hardening of the V phase is also likely. In addition, both Ni and Al are



**Figure 30:** Ni-Al-V phase diagrams. a) Ni-Al-V ternary isotherm at 1073 K [9] b) NiAl-V pseudo-binary isopleth [8].

known to embrittle V at levels as low as 1 weight percent [11]. In fact, Cotton et al. [7] measured the increase in Vickers hardness for both NiAl and V in hypoeutectic alloys containing up to 20 at% V. The hardness of the V-phase nearly triples, going from  $120 \pm 8 \text{ kg/mm}^2$  to  $379 \pm 20 \text{ kg/mm}^2$ , while for NiAl the increase is from  $254 \pm 10 \text{ kg/mm}^2$  to  $356 \pm 6 \text{ kg/mm}^2$ . The hardness values of composite regions were measured to be even higher by at least  $25 \text{ kg/mm}^2$ .

It is interesting to note that the hardness of pure V is less than one half that of binary NiAl, but when each is saturated with the components of the other, the V-solid solution becomes harder. Another important point is the effect of V additions on the Ni:Al ratio of the NiAl phase, i.e., the effective stoichiometry. The fact that the solubility for V is negligible for Al-rich NiAl suggests that V substitutes for Al in the ordered structure [7]. A site occupancy study using the ALCHEMI technique has confirmed preferential substitution of V on Al sites [10].

In addition to the effects of V additions to the matrix phase, the presence of a large volume fraction of a metallic phase may have a large effect on the fracture toughness, but the extent of these effects have yet to be verified experimentally.

## 2. EXPERIMENTAL PROCEDURE

The binary eutectic composites NiAl-9Mo, NiAl(0.1Zr)-9Mo, NiAl(0.1Zr)-12Mo, NiAl(0.1Zr)-15Mo, and NiAl-40V were directionally solidified using the CELZ process described previously. For each ingot, the processing atmosphere was He with an initial oxygen concentration in the range of  $10^{-13}$  to  $10^{-14}$  parts per million. Data records for the NiAl-9Mo and NiAl-40V ingots used for mechanical property evaluation are shown in Figs. 31 and 32. Typical CELZ-processed ingots are shown in Fig. 33. Growth conditions for the ingots are summarized in Table 9. The NiAl-40V ingot was long enough to section into two parts 40 mm in length, which were designated as sections i and ii. Observations concerning the processing of each composite are presented separately in following sections.

**Table 9: Growth conditions for two-phase eutectic alloys.**

COMPOSITION	GROWTH RATE(cm/hr)	ROTATION RATE(rpm)
NiAl(0.1Zr)-9Mo	1.9	85
NiAl-9Mo	1.9	75
NiAl-12Mo	1.9	50
NiAl-15Mo	1.9 - 2.5	45 - 65
NiAl-40V i*	1.3	150
NiAl-40V ii*	1.3	200

\* i and ii refer to sections of the NiAl-40V ingot.

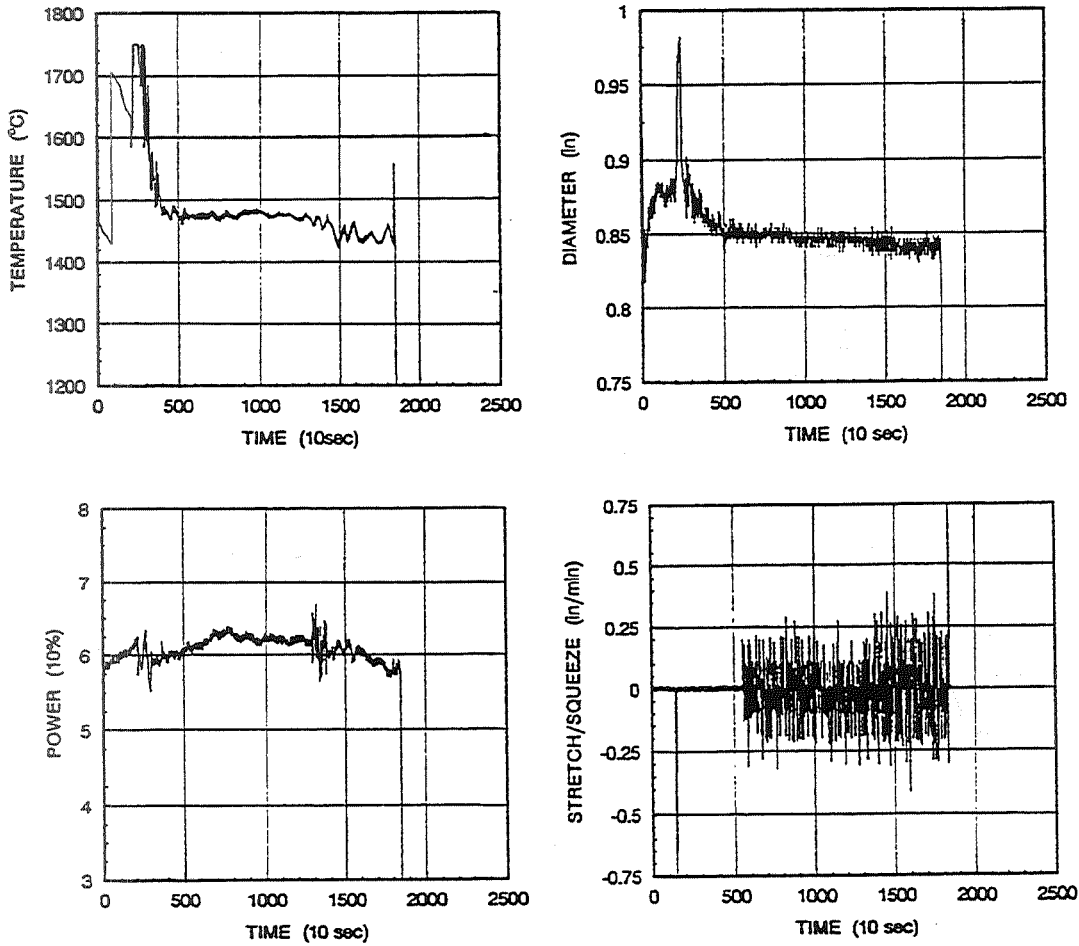


Figure 31: Typical melt record for NiAl(0.1Zr)-9Mo. Shown are a) temperature, b) liquid diameter, c) percent power, and d) stretch/squeeze as a function of time.

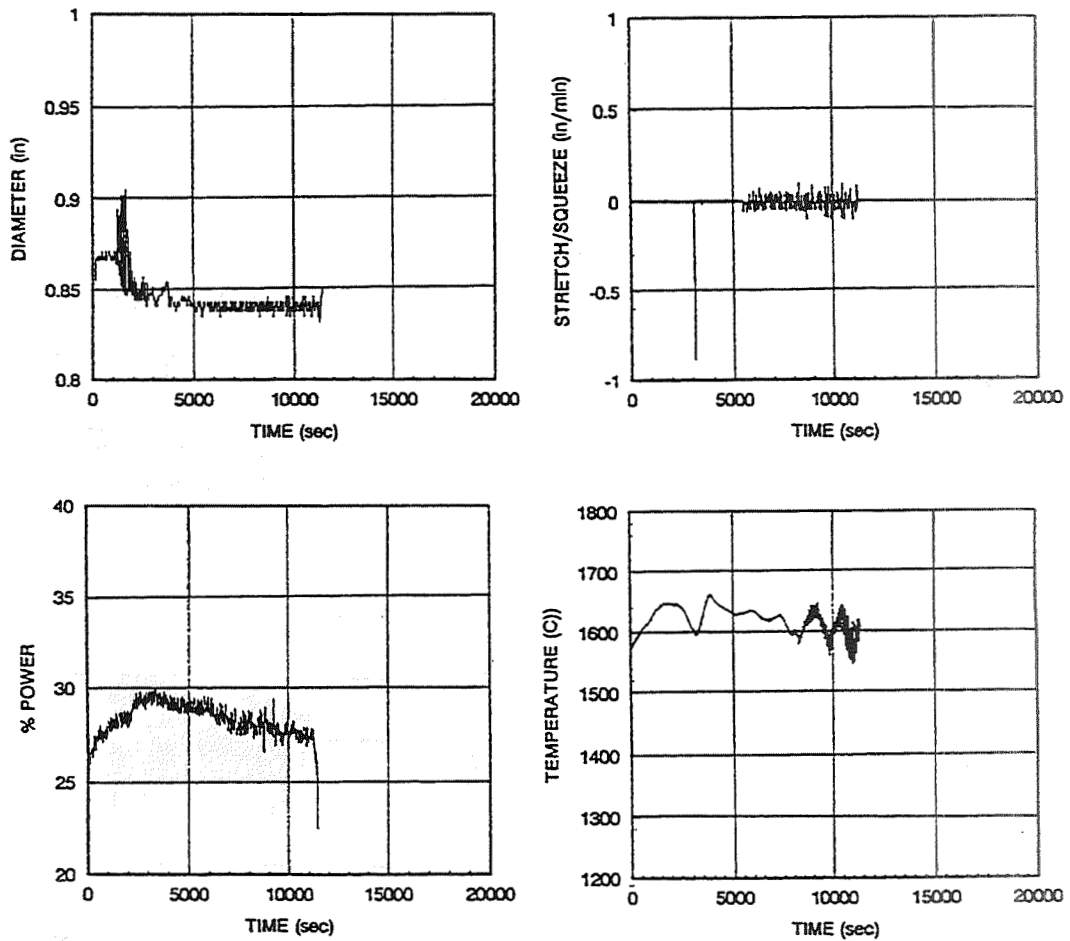


Figure 32: Typical melt record for NiAl-40V. Shown are a) liquid diameter, b) stretch/squeeze, c) percent power, d) temperature, e) distance traveled, f) growth rate, and g) rotation rate of the interface as a function of time.



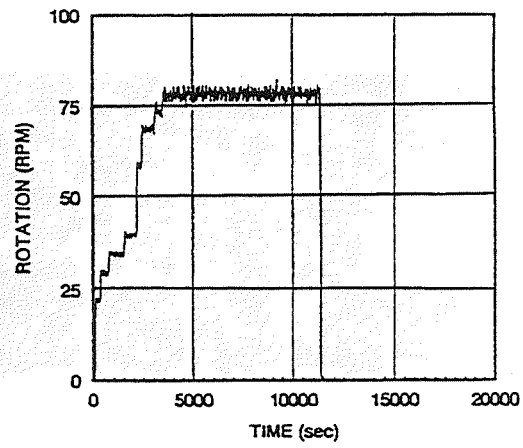
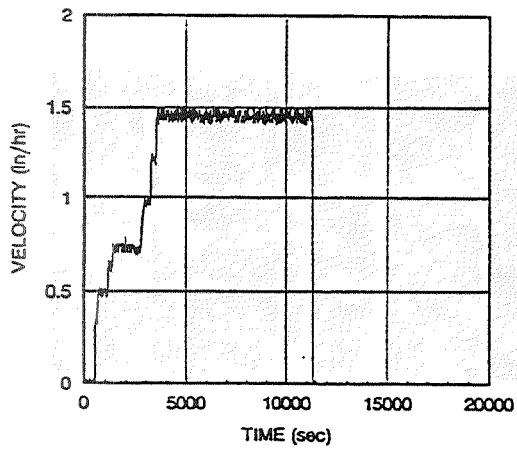
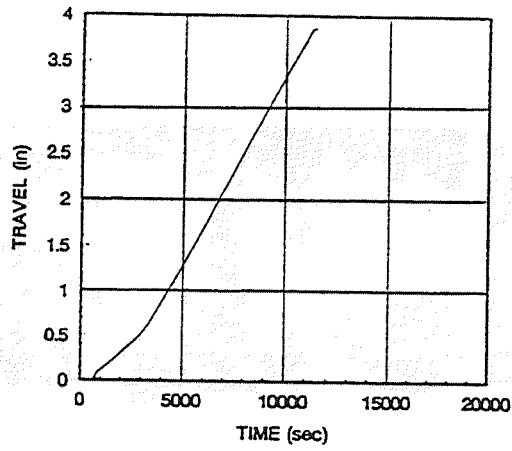
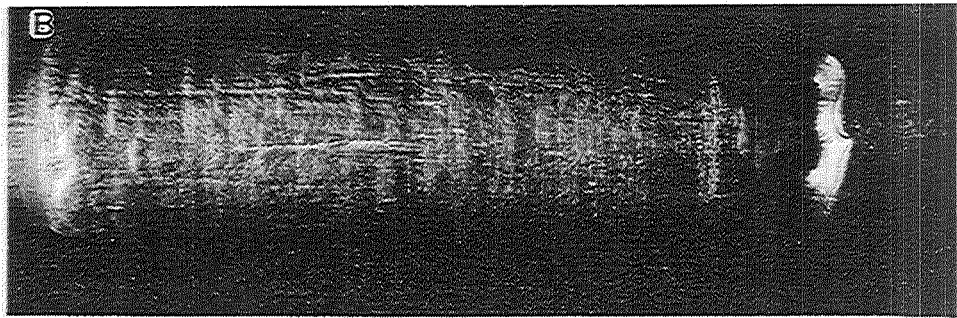
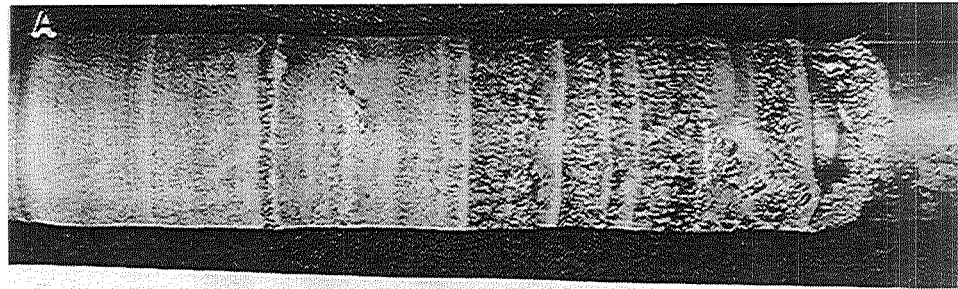


Figure 32 continued.



Growth Direction

**Figure 33:** As-processed ingots of a) NiAl-40V and b) NiAl(0.1Zr)-9Mo.

Microstructural characterization included optical, scanning electron, and transmission electron microscopy. All SEM microscopy was performed at 20-25 kV, using either a Cambridge Stereoscan 120 or a Cambridge Stereoscan 360. The Stereoscan 360 was used for EDS analysis of the constituent phases. However, it should be noted that the fine scale of these eutectic microstructures and beam spreading beneath the specimen surface often prevented an accurate determination of the individual phase compositions. Contrast due to differences in atomic number is minimal between the NiAl and V phases of the NiAl-40V eutectic even using backscattered electron imaging. On the other hand, the NiAl-9Mo eutectic has strong contrast between the constituent phases even for secondary electron imaging. In addition, the SEM was used to characterize the fracture of both eutectic alloys.

The room temperature fracture toughness of both composites was determined by four-point bending as described previously. High temperature testing was performed by J.D. Whittenberger at NASA-LeRC. The creep strength reported here is actually the true stress at 1% true strain required to maintain a constant creep rate of  $\sim 2 \times 10^{-6}$  per second. Compressive yield strength as a function of temperature was determined for the eutectic compositions. The nominal strain rate was  $1.4 \times 10^{-4} \text{ s}^{-1}$  for these tests.

Transmission electron microscopy was performed by Ms. X.F. Chen, a visiting scholar from Shanghai Jiao Tong University, P.R. China. Both binary eutectic alloys were characterized using TEM techniques. Dislocations were characterized for as-processed and room temperature bend tested specimens using a near invisibility criterion, g·b. This information was used to determine which deformation and failure mechanisms are active during room temperature bend testing.

### **3. NiAl-Mo SYSTEM**

Although processing of several NiAl-Mo ingots was attempted, only one ingot of each composition was used for mechanical property testing. Microstructural characterization was performed on the processed ingots used for mechanical property evaluation. Microstructural characterization, mechanical property results, and discussion of the elevated temperature test results are presented in this part. Detailed discussion and evaluation of the fracture toughness and fracture mechanisms will be presented in PART VII.

### 3.1 Processing

The NiAl(0.1Zr)-9Mo ingot was processed before the first control system upgrade was implemented. Therefore, the data record is limited to temperature, liquid diameter, power, and stretch/squeeze as a function of time. Power control was manual for this run. The small Zr addition does not significantly affect the processing parameters. The zone was established approximately 300 seconds into the data record, while liquid diameter control was implemented at 550 seconds into the run, Fig. 31(d). Variation in the recorded temperature resulted from rollover of the liquid onto the processed ingot and into the view of the optical pyrometer. Several diameter set point changes were made during this run to prevent the liquid from spilling, Fig. 31(b).

The NiAl-9Mo ingot was processed after the first system upgrade and therefore the data record contains additional information concerning solid diameter, ingot position, growth velocity, rotation rate, and interface location as a function of time. Diameter control was initiated at 1042 seconds and power control began at 1722 seconds into the run. The Mo-eutectic proved to be very difficult to process due to its high melting point, high thermal conductivity, and low surface tension of the liquid zone. Even under computer control, the liquid often spilled over the interface onto the solidified ingot. Computer control was

terminated briefly at about 15000 seconds in order to prevent a spill. As shown in the data record, the solid diameter was not constant even though the liquid diameter was under control during most of the run. This was due to the variation in the interface position and the roll over of the liquid onto the processed ingot. Comparison between the power, interface position, and solid diameter data records illustrates the coupling between process variables as discussed previously.

Since button melts with hyper-eutectic compositions show improved fracture toughness over NiAl, two hyper-eutectic ingots were directionally solidified using the CELZ process. An NiAl-12Mo ingot was processed at 1.9 cm/hr and 50 rpm (Table 9). While the power was controlled manually throughout the run, diameter control was initiated approximately half way through the run. An NiAl-15Mo ingot was processed at 1.9 to 2.5 cm/hr and 45 to 65 rpm under manual control. Establishing steady state growth conditions for the hyper-eutectic compositions proved to be difficult. The hyper-eutectic compositions exhibit the same melt characteristics as the eutectic composition, including the tendency for the liquid to roll over onto the processed ingot.

### 3.2 Microstructure

The microstructure of both NiAl-9Mo and NiAl(0.1Zr)-9Mo consists of Mo rods in an NiAl matrix as shown in Figs. 34 and 35. The rods do not appear as sharply faceted as for similar compositions processed by the modified Bridgman technique. The rod morphology of the Bridgman-processed material more closely resembles the as-cast structure of the precursor ingots used in this study, Fig. 36. While an effect of purity on the rod morphology can not be ruled out, the Bridgman process is more likely to represent steady state growth conditions compared to the CELZ process. Control of the CELZ process is more complex and dynamic in nature than that of the Bridgman process because the ingot is an integral part of the power supply in the CELZ process. Hence, the rods may have been in a state of transition throughout the growth process due to slight variations in the actual growth rate. The resulting variation in rod diameter and spacing is minimized by tighter process control.

The variation in rod spacing is shown in the low magnification micrograph, Fig. 37. A schematic representation of the solid-liquid interface at progressive times during solidification and a planar intersection (surface of a metallographic section) with these surfaces is shown in Fig. 38 to illustrate the development of the bands

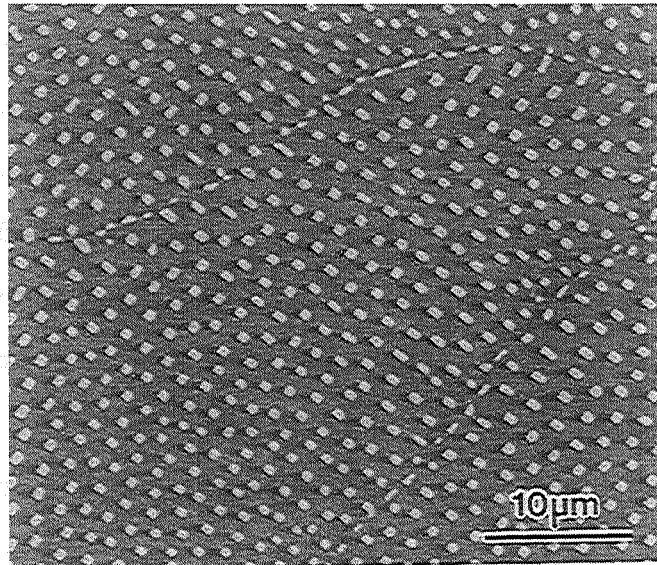


**Figure 34:** (SEM-4QBS) As-processed microstructure of NiAl-9Mo, transverse section, unetched.

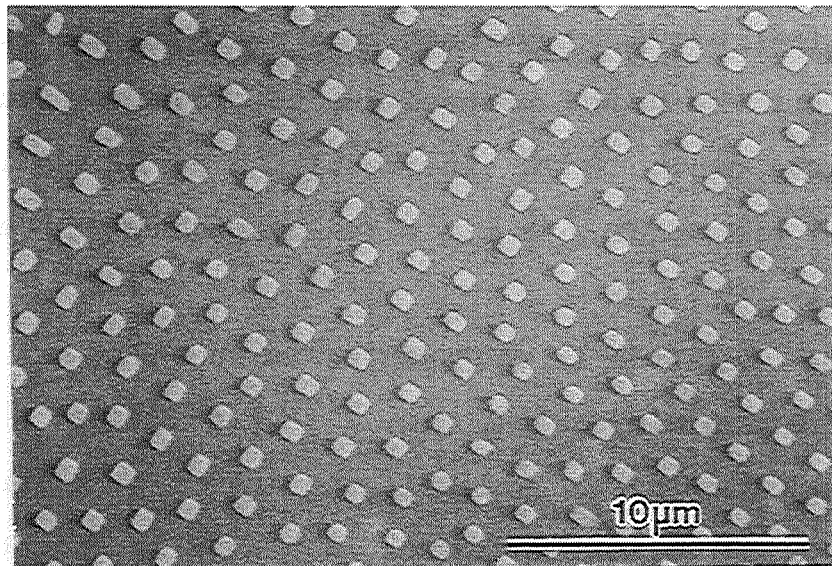


**Figure 35:** (SEM-4QBS) As-processed microstructure of NiAl(0.1Zr)-9Mo, transverse section, unetched.



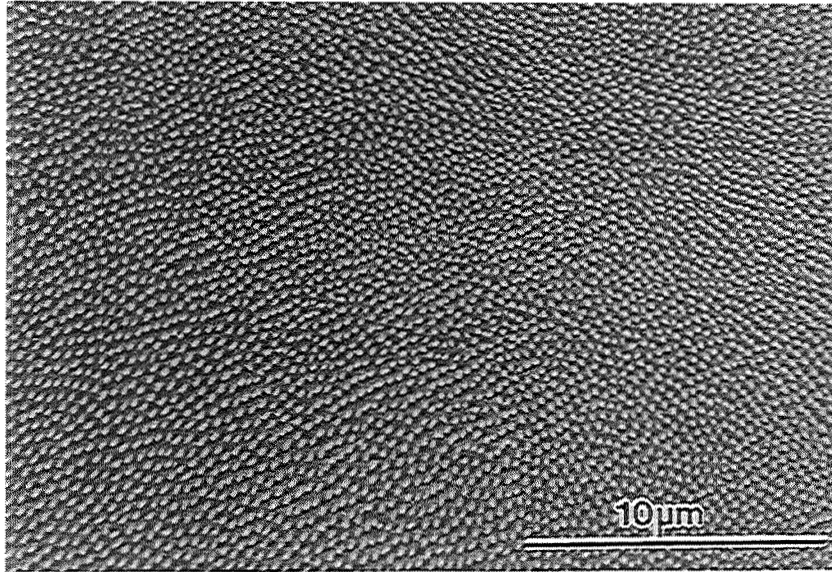


**Figure 36:** (SEM-4QBS) As-cast microstructure of NiAl(0.1Zr)-9Mo precursor ingot, transverse section, unetched.

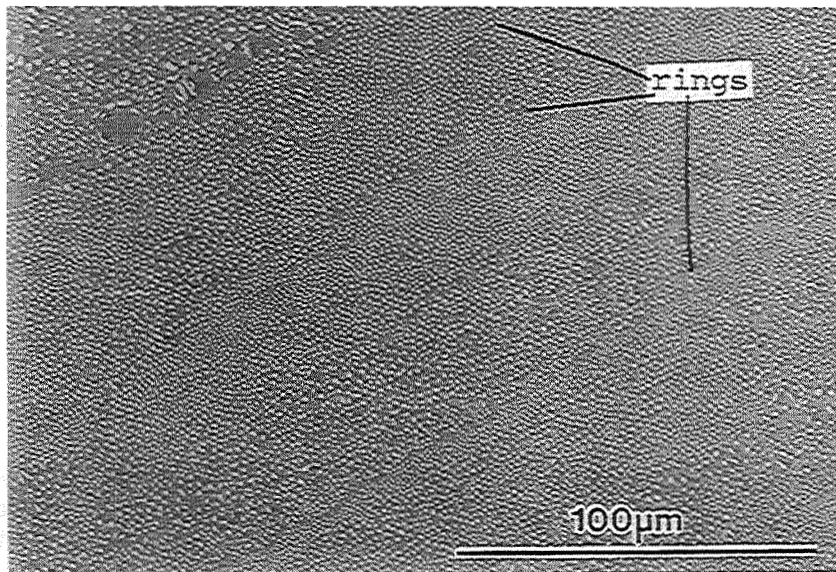


**Figure 37:** (SEM-4QBS) As-processed NiAl-9Mo ingot showing rings of variable rod spacing and density due to variation in growth conditions.

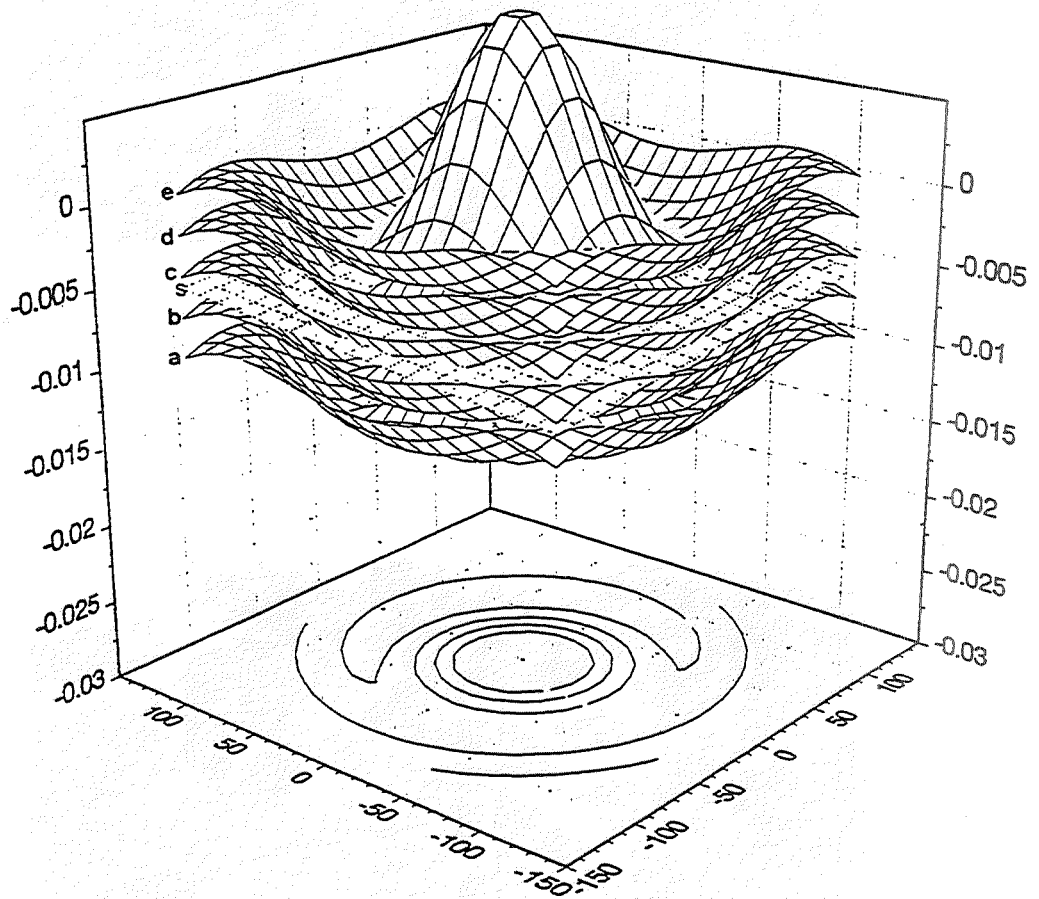
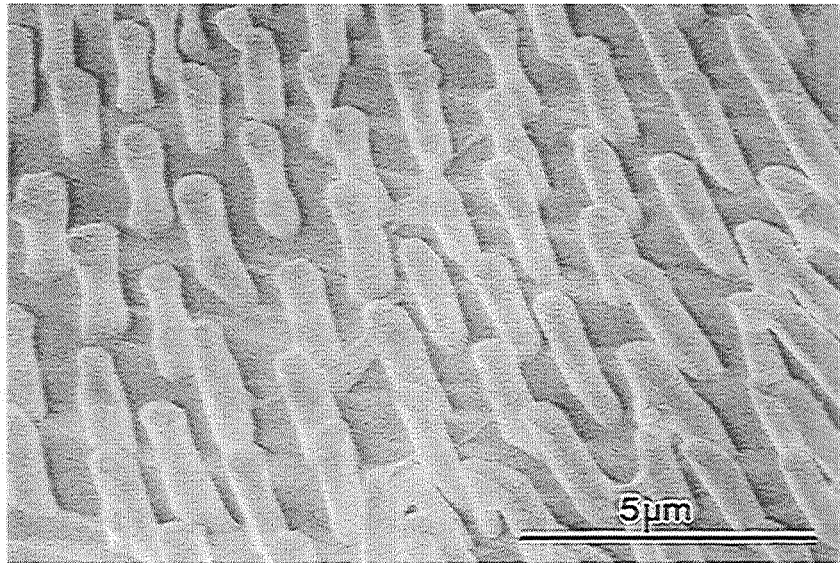


Figure 38: Schematic illustration of the development of the ring pattern observed in NiAl-9Mo ingots. The surfaces a-e represent the growing interface at successive times during solidification. Since the growth rate varies along a to e, the rod spacing must change according to the relation:  $G/R \propto \lambda^2$ . The plane S is the sectioning plane which is projected onto the plane below.

observed in Fig. 37. Deep etching of a specimen reveals that branching of the rods (Fig. 39) occurs as a means to alter the rod spacing. A variation in the dimensions of individual rods is also shown in Fig. 39.

The orientation of the rods vary such that each rod grows perpendicular to the local solidifying interface. On a small scale, this means that the cusp formed at an eutectic colony boundary at the solid-liquid interface will alter the rod axis towards the boundary [12], Fig. 40. Macroscopically, the curvature of the solid-liquid interface will alter the rod axis of the entire colony. Hence, a sample taken from the center of the ingot will contain rods which are aligned with the specimen axis, while the alignment between the rod axis and specimen axis may vary for specimens taken near the perimeter of the ingot.

In addition to slight variations in rod morphology and orientation, the ingots contain structural discontinuities. These discontinuities appear as bands transverse to the growth direction where the composite or coupled growth is disrupted. A severe case is shown in Fig. 41. Dendrites of NiAl form across the interface for a short distance followed again by coupled growth. The origin of these growth defects is unknown and does not correlate with any process control parameter. However, similar defects occur in ingots processed using the Bridgman technique [5].



**Figure 39:** (SEM-SE) Deeply etched NiAl(0.1Zr)-9Mo ingot. Shown are rod branching and variations in the rod diameter which occur during directional solidification.

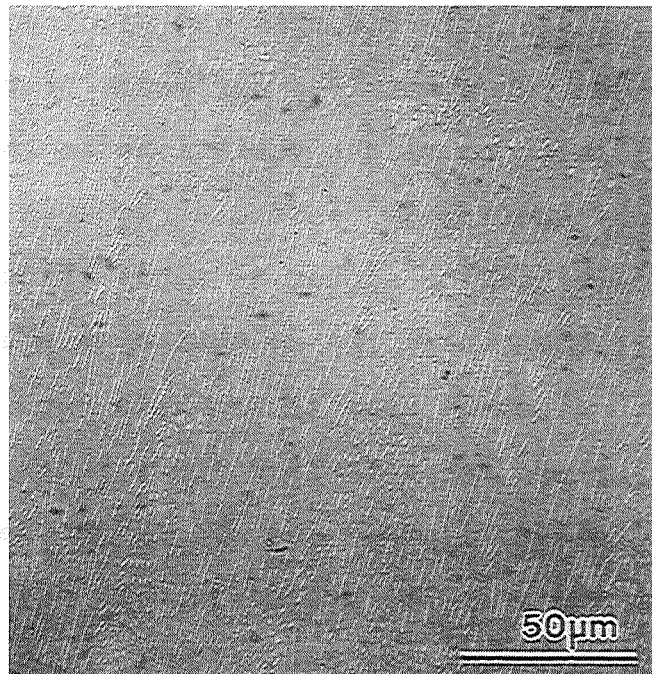


**Figure 40:** Longitudinal microstructure of NiAl(0.1Zr)-9Mo.

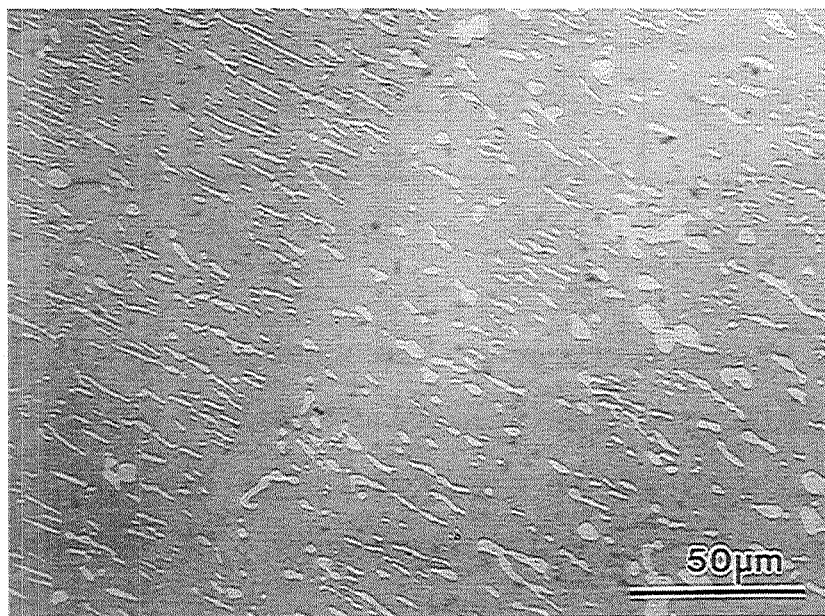


**Figure 41:** Longitudinal section of NiAl(0.1Zr)-9Mo showing severe banding.

The interstitial purity of the NiAl(0.1Zr)-9Mo ingot is given in Table 10. The level of purity is not as high as for NiAl. The source of the additional impurities is most likely the Mo feed stock for the precursor ingots.

**Table 10: Interstitial impurity content\* (atomic %).**

ALLOY	Carbon	Nitrogen	Oxygen	Sulfur
NiAl(0.1Zr)-9Mo	0.0194	<0.0007	0.0057	<0.0020
NiAl-40V	0.0506	0.0191	0.0069	0.0023

\* Relative accuracy 10%

The microstructures of the hyper-eutectic alloys are shown in Fig. 42. The primary difference between these alloys and NiAl-9Mo is the presence of large Mo grains in the banded and intercellular regions. The intent is to increase the volume fraction of the Mo-phase in the composite structure. Coupled growth of off-eutectic compositions is possible [13], but disruptions in the coupled growth of the ingot are observed to occur more often than for the eutectic composition. However, the presence of large Mo particles increase the volume fraction of the ductile reinforcement phase and may therefore enhance the fracture toughness. The possible effects on the high temperature properties are less clear, see section 5.4.2.

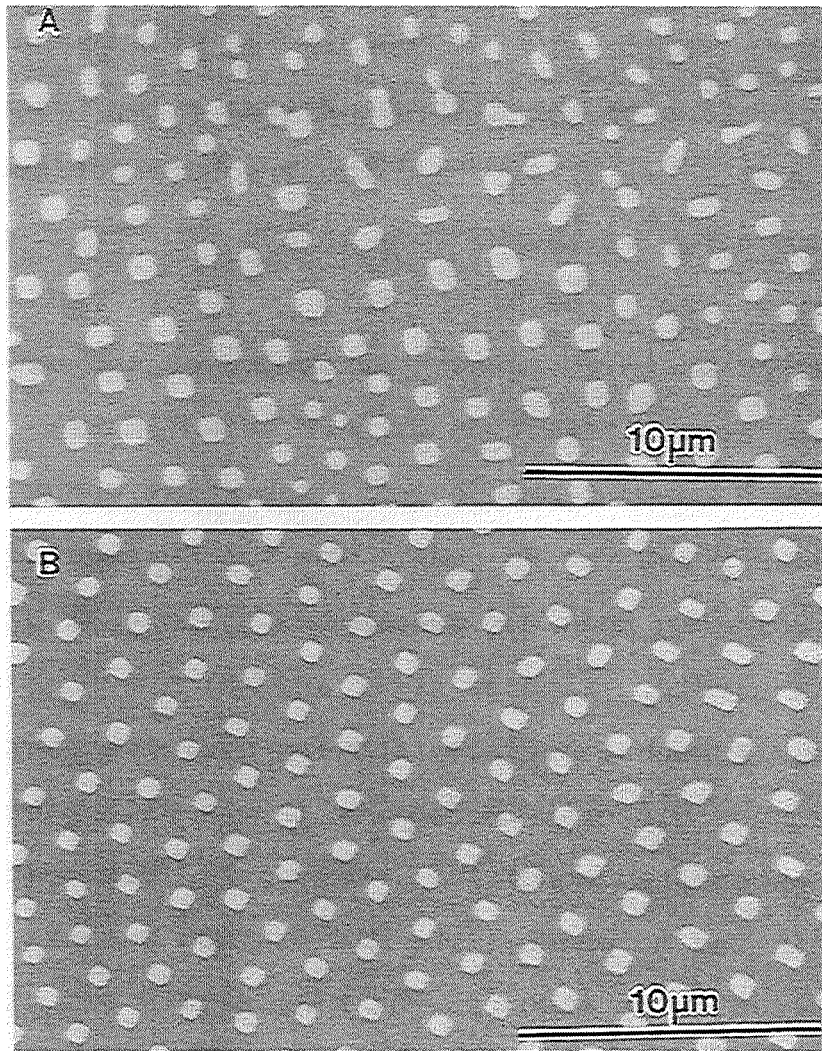


**Figure 42:** (SEM-4QBS) Microstructure of eutectic regions in a) NiAl(0.1Zr)-12Mo and b) NiAl(0.1Zr)-15Mo, transverse sections, unetched.

### 3.3 TEM Observations

Shown in Figure 43 is a typical TEM micrograph of the microstructure of the NiAl(0.1Zr)-9Mo alloy. Figure 43(a) represents material far from the fracture surface and shows the morphology of the Mo rods in the CELZ-processed condition. The plane of the foil is (001) which is perpendicular to the growth direction of the eutectic. The selected area diffraction pattern shown in Fig. 43(b) confirms a cube-on-cube orientation relationship between the NiAl matrix and the Mo rods. The volume fraction of the reinforcing Mo rods was determined to be 0.11 by SEM digital image analysis. Figures 44(a) and (b) are from material near the fracture surface, showing dislocation tangles and a much higher dislocation density in the NiAl matrix than for the as-processed condition. Only a few dislocations can be found in the Mo phase. The dislocation Burgers vectors were determined to be  $\langle 100 \rangle$  in the NiAl matrix and  $\langle 111 \rangle$  in the Mo phase [14].

### 3.4 Mechanical Properties

#### 3.4.1 Fracture Toughness

Results of the screening tests performed on the binary eutectic alloys are listed in Table 11. At first, the Zr addition appears to have a significant effect on the room



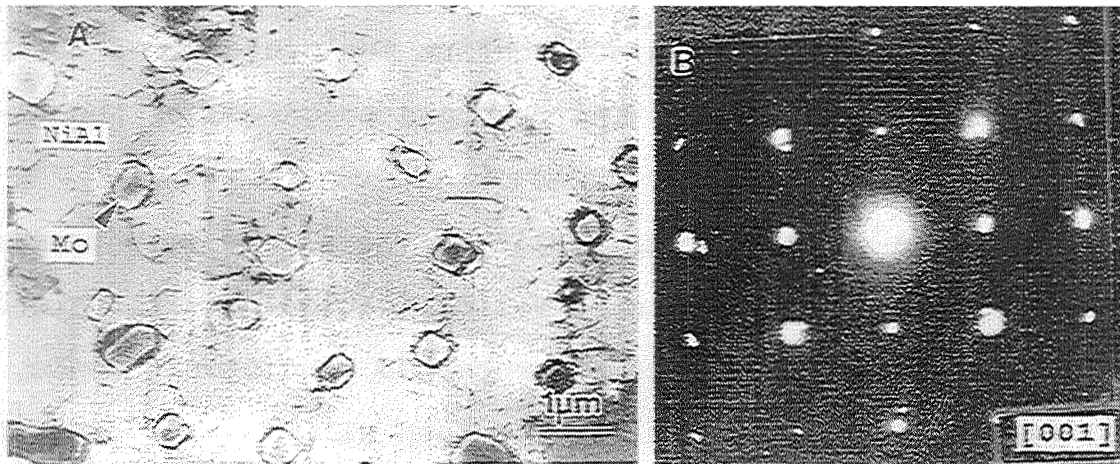


**Figure 43:** TEM micrograph and diffraction pattern of NiAl-9Mo. a) micrograph along a  $\langle 001 \rangle$  direction (growth direction), b)  $[001]$  diffraction pattern showing the cube-on-cube orientation relationship between the NiAl and Mo phases.

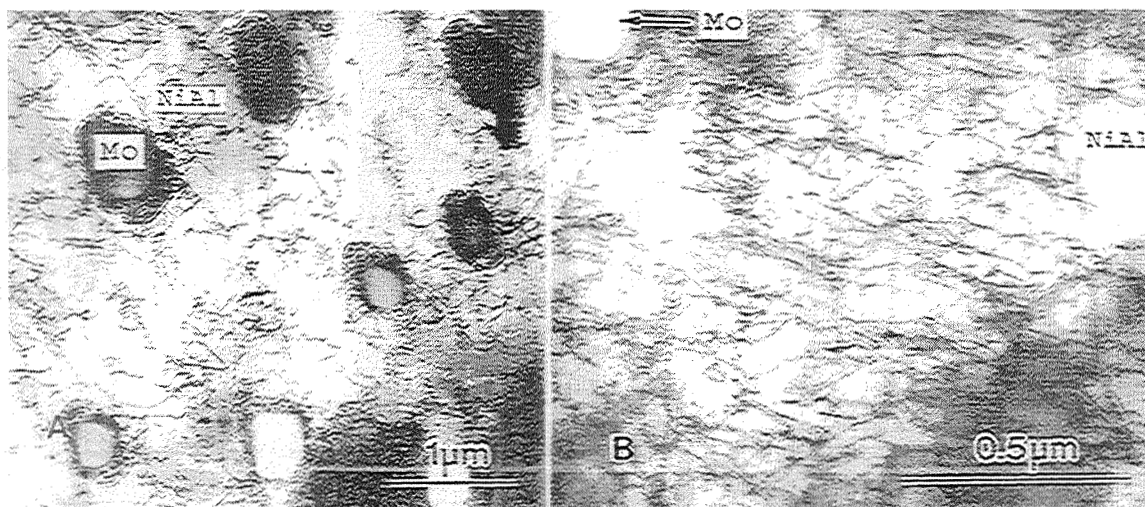


**Figure 44:** TEM micrographs of NiAl(0.1Zr)-9Mo taken near the fracture surface of a bend bar. Both a) and b) show the high dislocation density in the NiAl matrix.

temperature fracture toughness of NiAl-9Mo, even though chemical analysis does not confirm the presence of Zr in the CELZ processed ingot. The fracture toughness of the Zr-doped alloy is  $15.7 \pm 0.8$  MPa $\sqrt{m}$  compared to only  $7.0 \pm 0.2$  MPa $\sqrt{m}$  for the Zr-free alloy. The alloys were processed under essentially the same solidification conditions and both were tested in the as-processed condition. Hence, the thermal history is similar for each alloy. The observed difference, however, is due to banding in the Zr-free specimens in the vicinity of the notch root. There are other possible reasons for the difference in fracture toughness as well, such as gettering of impurities by the Zr addition and solid solution strengthening of the Mo rods. The effect of reinforcement properties will be covered in PART VII.

**Table 11: Results of screening tests for binary eutectics.**

ALLOY	$K_I$ (MPa $\sqrt{m}$ )	Creep (MPa)	Density (g/cm <sup>3</sup> )	Eutectic $T_e$ (K)
NiAl-9Mo	$7.0 \pm 0.2$	---	---	1778
NiAl(0.1Zr)-9Mo	$15.7 \pm 0.8$	81.5	6.39	1778
NiAl(0.1Zr)-12Mo	$15.5 \pm 1.3$	---	6.45	--
NiAl(0.1Zr)-15Mo	$14.0 \pm 2.6$	---	6.62	--
NiAl-40V	$32.9 \pm 3.6$	39.8	5.93	1633

A closer look at the microstructure in the region of fracture for the bend specimens reveals severe banding for the 15Mo specimens and little or no banding for the 12 Mo specimens in the immediate vicinity of the notch, Fig. 45. The fracture path is observed to follow the boundary between the NiAl and Mo phases in the banded regions. Hence, there was no crack bridging contribution from the large Mo particles for the NiAl(0.1Zr)-15Mo material.

The standard deviation of the fracture toughness data is not large for specimens where the notch is far from a banded region. Even though the banding will act as a stress riser, the notch will concentrate the stress onto a smaller volume of the specimen such that only the local microstructure at the root of the notch determines the specimen behavior, not necessarily the weakest link in the microstructure. Furthermore, some interdendritic Mo-phase reinforcement is always present even in the most severe cases of banding.

It should be emphasized that the banding observed in the microstructure is found in Bridgman processed ingots as well and is not limited to the NiAl-Mo system. In fact, the banding is more severe for the NiAl-34Cr alloy because the Cr-phase is completely suppressed in the banded regions [15]. For the NiAl-34Cr eutectic alloy, some bend bars fractured outside the 2 mm deep notch at a disruption in the

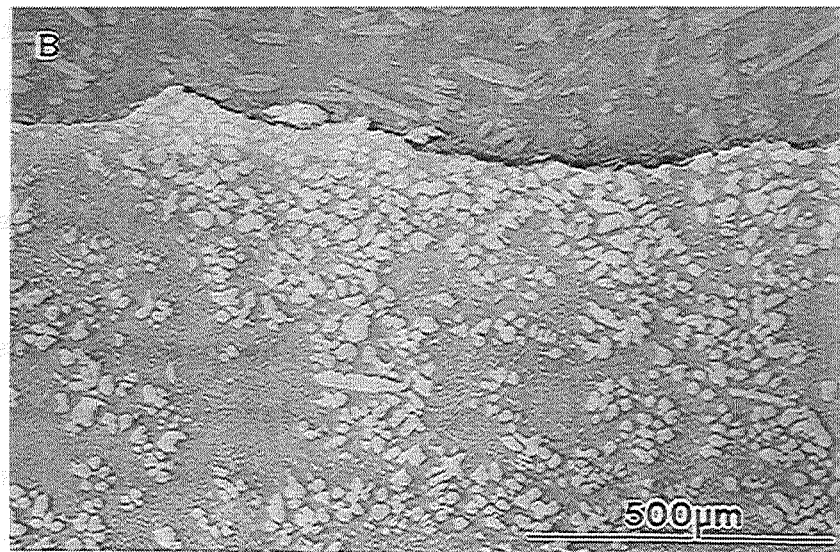
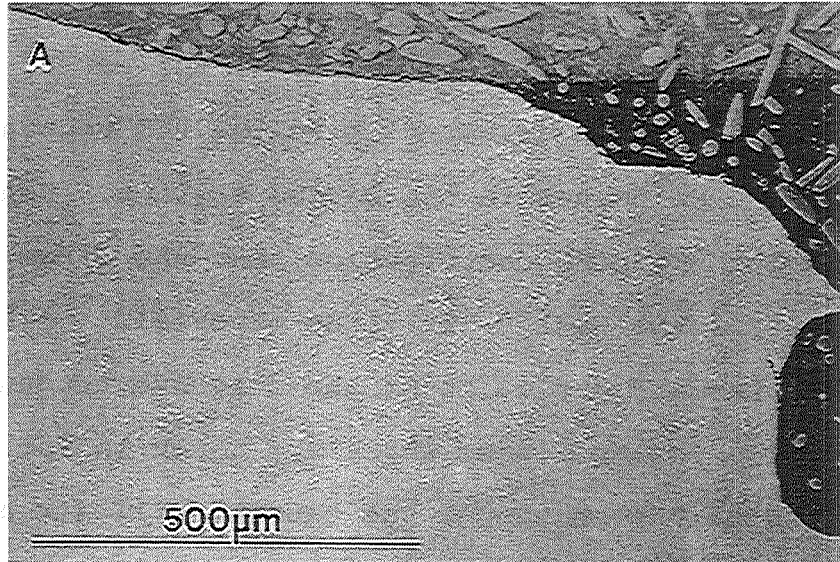


**Figure 45:** (SEM-4QBS) Microstructure at the root of the notch in a) NiAl(0.1Zr)-12Mo and b) NiAl(0.1Zr)-15Mo bend bars. Severe banding at the root of the notch causes the low fracture toughness observed in NiAl(0.1Zr)-15Mo.

composite structure [15]. Finally, it should be stated that in the absence of a notch, the fracture initiation site is likely to be more closely associated with the banding. The results indicate that a 2 mm deep notch is a more severe stress riser than the banding in the microstructure for the NiAl-Mo system, but not for the NiAl-34Cr alloy.

The fracture toughnesses of the hyper-eutectic alloys do not show any improvement over that of the eutectic composition. The NiAl-12Mo specimens have a fracture toughness of  $15.5 \pm 1.3$  MPa $\sqrt{m}$  and NiAl-15Mo of  $14.0 \pm 2.6$  MPa $\sqrt{m}$  [16]. This suggests that the presence of large Mo particles within the composite microstructure does not enhance the fracture toughness of the eutectic alloy, despite the larger volume fraction of reinforcement. The slight decrease in fracture toughness for the NiAl-9Mo and NiAl-15Mo specimens is due to microstructural discontinuities in the vicinity of the notch, i.e., the presence of large Mo particles. The crack path is generally observed to follow the particle boundary unless the aspect ratio or size of the particle is large. Such a crack path is expected to require less energy per unit area and therefore detract from the fracture toughness. The larger standard deviations in fracture toughness values support this observation.

Determination of the volume fractions of Mo in the hyper-eutectic alloys reveals that the excess Mo is dumped either in the intercellular regions of the microstructure or in the banded regions. The eutectic colonies contain 0.11 volume fraction Mo phase, the same as ingots of the eutectic composition. In fact, the NiAl(0.1Zr)-12Mo specimens show the same fracture toughness as the NiAl(0.1Zr)-9Mo alloy. The excess Mo contributes to the banding problem and is therefore more likely to decrease rather than increase the fracture toughness of the directionally solidified composites.

#### 3.4.2 Elevated Temperature Properties

The Zr addition is intended to improve the elevated temperature properties of NiAl, specifically the oxidation resistance. Therefore, the Zr-doped alloy was used to determine the effect of temperature on the yield strength as a function of temperature and creep strength at 1300 K. These tests were performed in air as a secondary check for oxidation resistance. The results are shown in Figs. 46 and 47 along with those of other binary eutectic alloys for comparison. All of the composites show improved yield strength at intermediate and higher temperatures and improved creep strength at 1300 K compared to single crystal NiAl in the hard orientation.

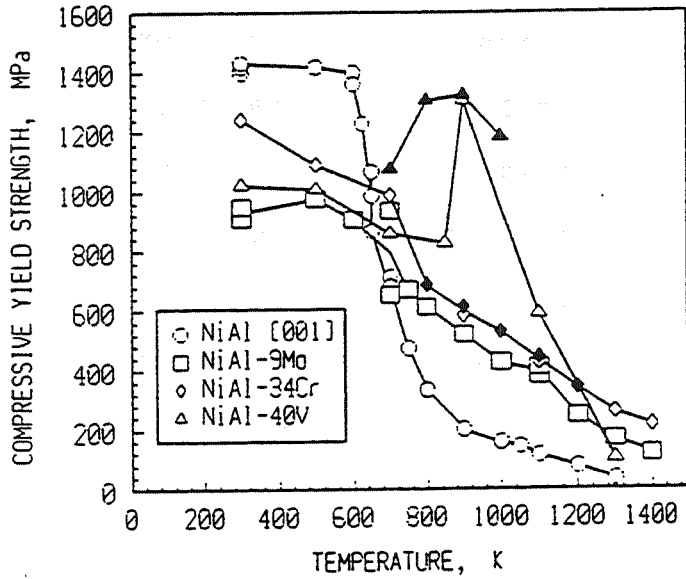


Figure 46: Compressive yield strength as a function of temperature for NiAl-based composites [16,20,21].

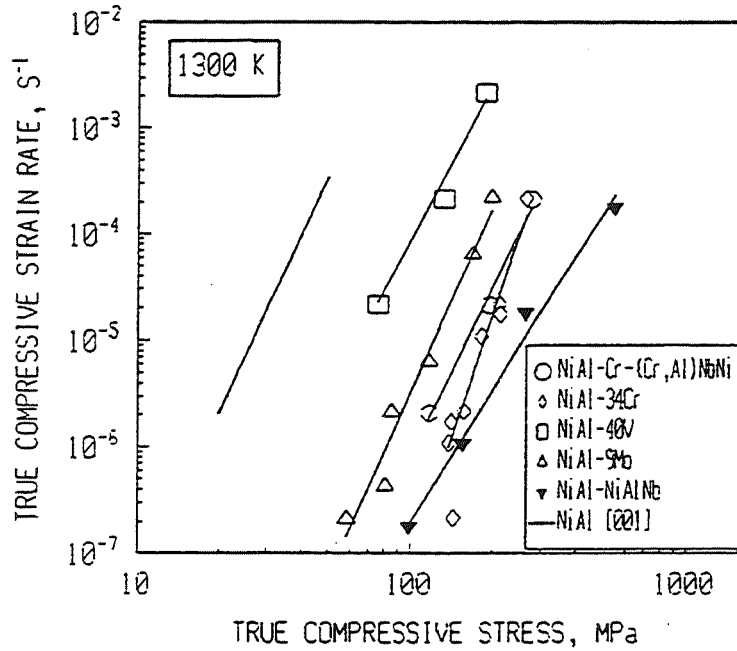


Figure 47: Compressive flow stress-strain rate behavior for several NiAl-based composites at 1300 K [16,20,21].

The compressive yield strength of NiAl-(0.1Zr)-9Mo is greater than that of [001] NiAl for temperatures above 700 K [16]. The improvement in yield strength persists to temperatures above 1300 K. Compared to NiAl, the decrease in yield strength with increasing temperature is less precipitous for the eutectic alloy. The abrupt decrease in yield strength observed for NiAl is associated with a change to a thermally activated deformation mechanism at the DBTT [17]. Such a change is not apparent for the eutectic alloy.

The 1300 K creep strength of NiAl-(0.1Zr)-9Mo at 1% true strain and a strain rate of  $10^{-6} \text{ s}^{-1}$  is 81.5 MPa and is represented by the equation:

$$\dot{\epsilon} = (8.59 \times 10^{-18}) \sigma^{5.79}$$

The stress exponent is essentially the same for [001] NiAl single crystals, Table 12 [16]. A stress exponent in the range of 4-5 generally indicates the creep behavior is dominated by a dislocation climb controlled mechanism [17-19]. Such a mechanism is typical of pure metals. The low solubility of Mo in NiAl and of NiAl in Mo is in line with this result.



**Table 12: Summary of 1300 K creep strength.**

ALLOY	phases present	Equation*
NiAl [001]	NiAl	$\dot{\epsilon} = (0.16)\sigma^{5.75} \exp\left(\frac{-314.2}{RT}\right)$
NiAl(0.1Zr)-9Mo	NiAl, Mo	$\dot{\epsilon} = (8.59 \times 10^{-18})\sigma^{5.79}$
NiAl-40V	NiAl, V	$\dot{\epsilon} = (1.56 \times 10^{-14})\sigma^{4.88}$

\*1200 - 1400 K range for [001] NiAl data.

As mentioned, the microstructure of the NiAl(0.1Zr)-9Mo varies along the length of the ingot. Although a significant effect due to banding is not observed for this alloy under the four point bend conditions used for fracture toughness evaluation, the creep strength varies significantly with specimen position along the growth direction. The 1300 K creep strength at 1% true strain and a strain rate on the order of  $10^{-5} \text{ s}^{-1}$  ranges from 90 to 169 MPa. Hence, the microstructure is very important to the development of this alloy for high temperature structural applications. The scale of the microstructure is an important parameter in determining the creep strength of composite materials. An increase threshold stress for creep is expected for very small reinforcement spacings [19]. Hence, the banded regions are most likely weaker than the continuous composite structure. The creep strength values

are presumed to represent minimum values for the composite material.

#### **4. NiAl-40V**

Two NiAl-40V ingots were processed, but only one ingot was used for mechanical property testing. Microstructural characterization was performed on the ingot used for mechanical property evaluation. This section concerns microstructural characterization, mechanical property results, and discussion of the elevated temperature test results. Discussion and evaluation of the fracture toughness and fracture mechanisms will be presented in Part VII.

##### **4.1 Processing**

The growth conditions for the second pass on the NiAl-40V ingot are given in Table 9. Two passes were made on this ingot because a high emissivity phase precipitates on the surface of the liquid zone during processing. The ingot was cleaned by grinding the deposit from the surface prior to the second pass. However, the precipitates formed again during the second pass. This unknown phase forms in the liquid and subsequently deposits on the surface of the

directionally solidified ingot, disrupting the process control by altering the heat flow conditions. Hence, the solid diameter varies along the length of the ingot. The actual growth rate deviates slightly from the nominal value because of the difficulty in maintaining tight control of the process.

#### 4.2 Microstructure

The resulting microstructure (Figs. 48 and 49) indicates that a cellular interface exists for growth under these processing conditions. The microstructure is aligned except for banding which does occur for this alloy as well (Fig. 50). Contrary to the NiAl-9Mo alloys, the vanadium solid solution is continuous in the NiAl-40V alloy. The volume fraction of NiAl is 0.50 as determined by both digital analysis of SEM images and weight fractions of optical micrographs and is slightly lower than reported in previous investigations [8]. The solubility of each phase in the other decreases with decreasing temperature. Precipitation of NiAl is observed in the V dendrites which intermittently disrupt the coupled growth, Fig. 51.

The purity of the NiAl-40V alloy is given in Table 10. The level of purity is lower than both NiAl and the NiAl-9Mo

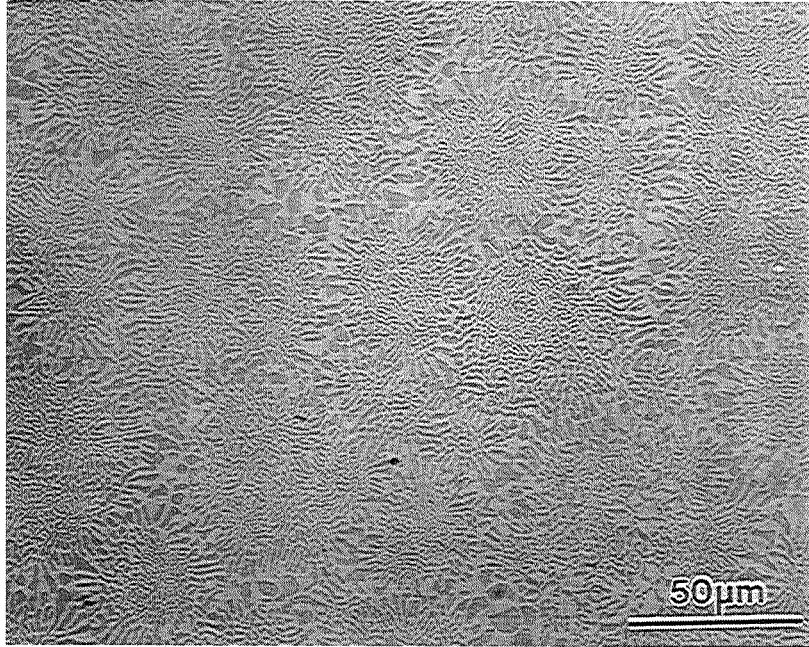


**Figure 48:** (OPT) Typical transverse microstructure of NiAl-40V showing cellular growth.

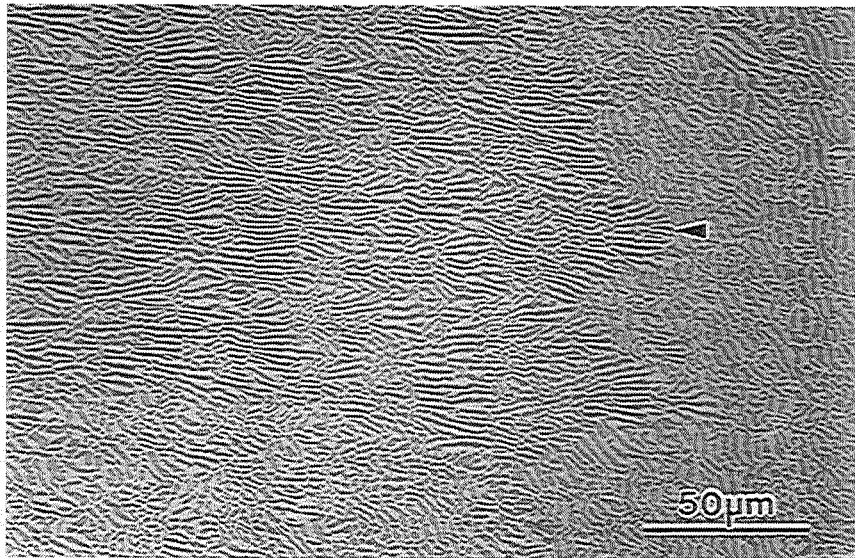


**Figure 49:** (OPT) Typical longitudinal microstructure of NiAl-40V showing cellular growth front (arrow).

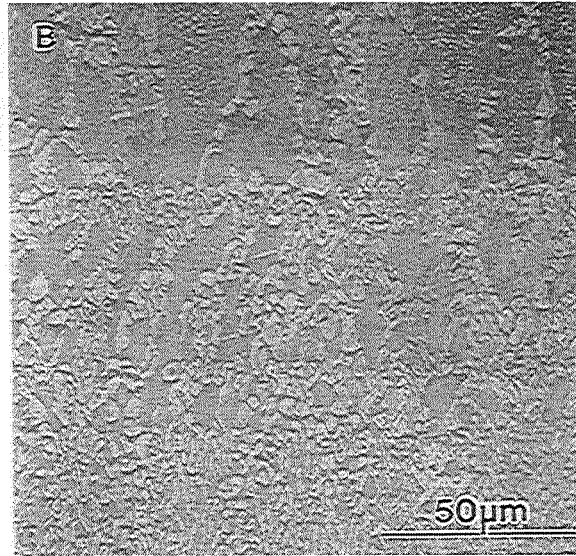
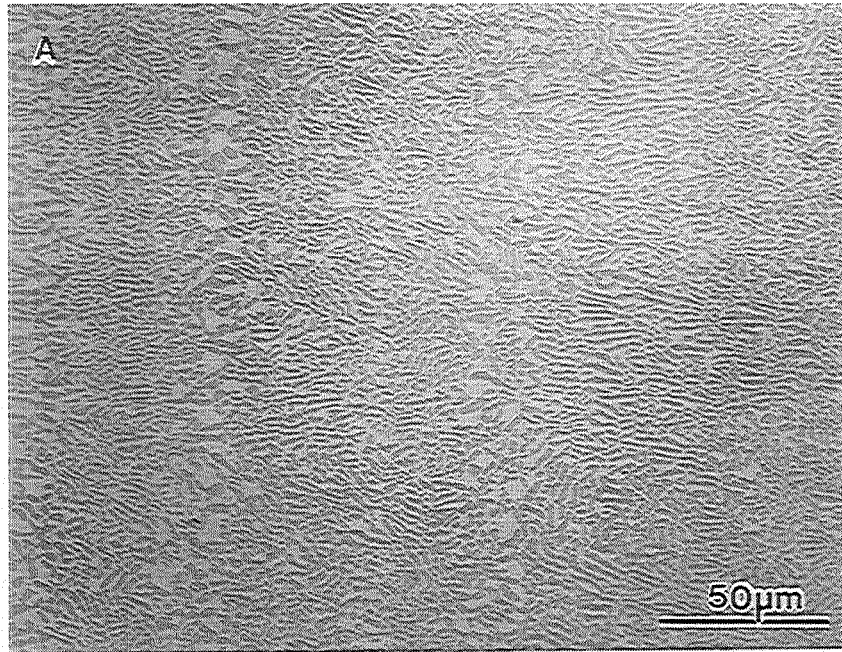


**Figure 50:** (OPT) Longitudinal section of NiAl-40V showing a) minor banding and b) severe banding due to changes in the local growth conditions.

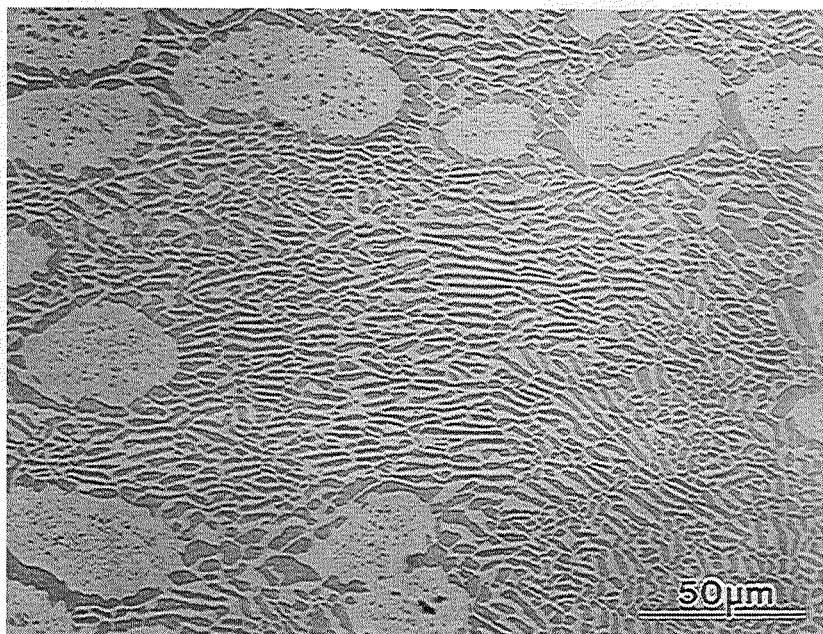


**Figure 51:** (OPT) Longitudinal section of NiAl-40V showing precipitation of NiAl within large single phase V regions. Precipitation does not occur within the coupled growth regions.

eutectic due to the purity of the vanadium stock and its high atomic percentage in the alloy.

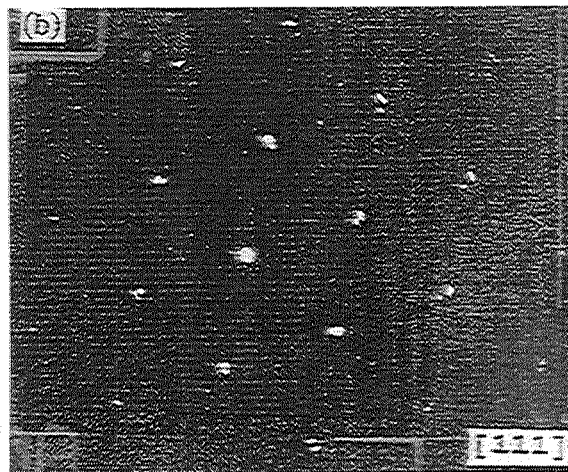
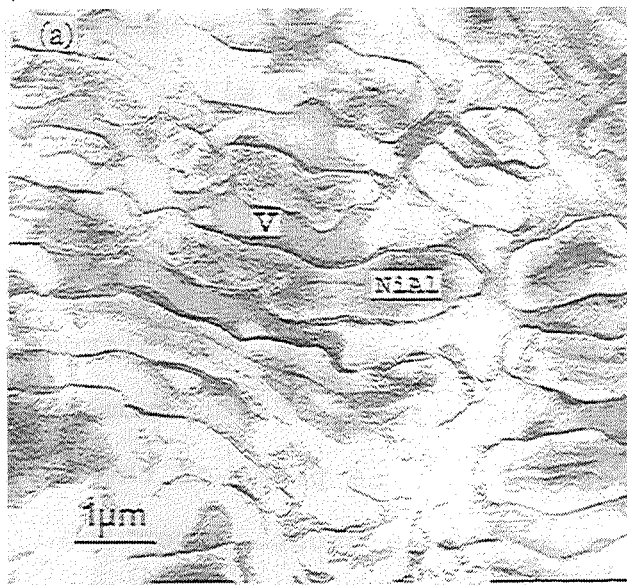
#### 4.3 TEM Observations

Figure 52(a) is a typical TEM micrograph of the as-processed NiAl-40V eutectic taken from the free end of a 4-point bend specimen. The plane of the foil is (001), which is perpendicular to the growth direction. The selected area diffraction pattern (Fig. 52(b)) shows that the lamellar NiAl phase has a cube-on-cube orientation relationship with the continuous vanadium matrix.

#### 4.4 Mechanical Properties

##### 4.4.1 Fracture Toughness

Results of the screening tests are given in Table 11. The room temperature fracture toughness of NiAl-40V is  $32.9 \pm 3.6 \text{ MPa}\sqrt{\text{m}}$  [16] making this alloy the toughest of the NiAl-based eutectics at room temperature. The volume fraction of reinforcement is the largest of the alloys studied and is a major reason for the large increase in fracture toughness. The fracture toughness of NiAl-40V is about a factor of three times higher than binary single crystal NiAl of similar orientation, also produced by the



**Figure 52:** (TEM) Micrograph and diffraction pattern of NiAl-40V. a) Micrograph of as-processed NiAl-40V along the  $\langle 001 \rangle$  direction (growth direction) showing NiAl lamellae in a continuous V phase, b)  $[111]$  diffraction pattern showing the cube-on-cube orientation relationship between NiAl and V.



CELZ process [20]. The mechanisms responsible for the fracture behavior will be discussed later in PART VII.

#### 4.4.2 Elevated Temperature Properties

The properties of NiAl-40V at elevated temperatures are shown in Figs. 46 and 47. The compressive yield strength and 1300 K creep strength are greater than [001] NiAl at intermediate and higher temperatures [16]. There is an anomalous peak in yield strength near 850 K for this alloy. The strength decays much faster than any of the other composites due to catastrophic oxidation of V (all elevated temperature testing is performed in air). As a result, the steep decline in strength can not be attributed solely to a DBTT as it is for NiAl. Further characterization of this phenomenon was not pursued because of the poor oxidation resistance of NiAl-40V. The low creep strength is primarily due to the oxidation of the V phase, but a lower value is also expected due to the lower melting temperature of this eutectic compared to the others. The 1300 K creep strength at 1% true strain and a strain rate of  $10^{-6} \text{ s}^{-1}$  is only 39.8 MPa, Table 12 [20] and is represented by the equation:

$$\dot{\epsilon} = (1.56 \times 10^{-14}) \sigma^{4.88}$$

Creep testing in an inert atmosphere would be an interesting topic for further study.

## 5. DISCUSSION

### 5.1 Microstructure

The previously reported orientation relationship and lattice parameter mismatch between the NiAl matrix and the reinforcement phase were confirmed for both the NiAl(0.1Zr)-9Mo and NiAl-40V alloys. As expected, the CELZ process does not affect these alloy parameters. However, volume fraction of reinforcement for the NiAl-40V alloy and the morphology of the Mo rods in the NiAl-9Mo vary slightly from those of previous investigations. The difference in volume fraction may be due to the technique used in determining the value. Two techniques were used in this investigation, image analysis of binary digitized images and weight fraction of SEM photographs cut along phase boundaries. The results from these two techniques concur.

The difference in processing technique may account for the variation in morphology of the reinforcement due to the dynamic nature of the CELZ process. The orientation relationship is cube-on-cube for the NiAl-(0.1Zr)-9Mo eutectic. The preferred growth direction is [001] as

evidenced by the diffraction pattern shown in Fig. 43(b). However, the rods must grow perpendicular to the solid/liquid interface. Hence, the boundary between the matrix and the reinforcement phase is forced off of the preferred  $\langle 011 \rangle$  planes, leading to the non-faceted rod morphology observed in some areas of the CELZ processed ingots. Other areas confirm the previously observed preference for the boundaries to lie on  $\langle 110 \rangle$  type planes.

No new slip systems were observed for the NiAl(0.1Zr)-9Mo or NiAl-40V alloys. In both cases, the NiAl was observed to deform by  $\langle 001 \rangle$ -type dislocations and the metallic phase by  $\langle 111 \rangle$  or  $\langle 110 \rangle$ -type dislocations typical of BCC metals. Hence, the theoretical prediction of slip system modification by vanadium additions is not observed experimentally for NiAl at the eutectic composition, i.e., NiAl saturated with V. However, this does not rule out changes in the mobility or ease of generation for  $\langle 100 \rangle$ -type dislocations in the NiAl(V) solid solution phase of the composite. Further discussion concerning dislocation generation as a mechanism for improving the fracture toughness is contained in PART VII.

## 5.2 Fracture Toughness

Compared to previous reports, the fault free growth and faceted morphology of the Mo reinforcement is not as evident for the CELZ processed ingots. However, the fracture toughness of CELZ processed NiAl(0.1Zr)-Mo concurs with previous investigation of NiAl-9Mo. Banding was noted in the microstructure regardless of processing technique and for both Zr-free and Zr-doped alloys. However, the observed banding was in the immediate vicinity of the notch for the Zr-free alloy, resulting in the lower fracture toughness values measured for this alloy. The Zr addition does not detract from the fracture toughness over single phase NiAl.

Although no fracture toughness data was reported for directionally solidified NiAl-40V prior to this investigation, previous investigation of hypo-eutectic V additions predict a limited increase in fracture toughness for composites containing vanadium as a reinforcement due to solid solution hardening effects [7]. In that investigation, the microhardness of the vanadium phase nearly triples and becomes greater than that of the NiAl phase for the two phase alloys. Based on this data, the outlook for vanadium as a potential ductile reinforcement was not good despite the high volume fraction of a metallic phase. However, the actual fracture toughness for the directionally solidified eutectic is quite high, 32 MPa $\sqrt{m}$ .

The active toughening mechanisms does not rely exclusively on the ductility of the V phase, as will be discussed in Part VII.

Comparison between the NiAl(0.1Zr)-9Mo and NiAl-40V illustrates the effects of the various second phase additions. These effects include the volume fraction, morphology, and mechanical properties of the reinforcement, as well as the effects of the alloy addition on the NiAl phase. The fracture toughness of NiAl-40V is about a factor of three times higher than binary single crystal NiAl produced by the CELZ process and two times greater than the NiAl(0.1Zr)-9Mo. However, the volume fraction of the reinforcing metallic phase is five times higher for the NiAl-40V eutectic alloy (0.50) than the NiAl(0.1Zr)-9Mo eutectic alloy (0.11). Therefore, when the fracture toughness values are compensated for volume fraction of reinforcing phase, Mo is over 2.5 times more effective than V at toughening NiAl. The difference in effectiveness between reinforcing phases lies in the mechanisms responsible for the increased toughness, which are ultimately determined by the elastic and plastic constraint and flow properties of the matrix and the reinforcing phase. The mechanisms involved in fracture of the composite alloys are discussed in detail in PART VII.

### 5.3 Elevated Temperature Properties

Creep testing was not performed on the hyper-eutectic alloys because the density is increased over that of the eutectic composition with no additional improvement in fracture toughness. Since the creep strength has been attributed to the fine scale of the composite microstructure, the hyper-eutectic compositions are not expected to show improvement in elevated temperature strength. The large Mo particles are presumed to weaken the composite based on the larger scale of the microstructure in the banded regions where these particles are found.

The mechanisms controlling creep behavior of NiAl are similar to those of disordered alloys [22]. Comparison of the stress exponents for the NiAl(0.1Zr)-9Mo and NiAl-40V alloys indicates a slight difference in creep behavior at 1300 K and a strain rate of  $10^{-6} \text{ s}^{-1}$ . The stress exponent for the Mo-eutectic is nearly identical to single crystal NiAl of the same orientation. However, the V-eutectic exhibits a slightly lower stress exponent. For pure metals, a stress exponent of approximately 4 to 5 generally indicates that creep behavior is controlled by dislocation climb. The stress exponents for both alloys are within the range of values expected for climb controlled creep behavior. The lower value for NiAl-40V may reflect the fact that V is both the continuous phase and the dominant phase

in the banded regions. A stress exponent of 3 generally indicates viscous glide controlled creep and is characteristic of alloyed metals. The vanadium phase in the NiAl-40V eutectic is certainly alloyed with Ni and Al.

#### 5.4 Comparison With Other Two-Phase Composites

Other binary eutectic alloys based on NiAl are presented here for comparison. The transverse microstructures are shown in Fig. 53. Table 13 lists the alloys, phases present, and properties of two-phase alloys recently processed using the CELZ technique at the University of Tennessee. A performance plot of the 1300 K creep strength versus the room temperature fracture toughness is shown in Fig. 54. Density compensated values are shown in Fig. 55. From this data, effects of the type of reinforcement phase on the key properties (fracture toughness and creep strength) can be easily ascertained. The NiAl-Laves phase eutectics exhibit good creep strength compared to other NiAl alloys, but unfortunately have a fracture toughness on the order of  $5 \text{ MPa}\sqrt{\text{m}}$ . However,  $5 \text{ MPa}\sqrt{\text{m}}$  is about the average fracture toughness for most polycrystalline NiAl alloys and soft oriented single crystals. Therefore, the large increase in creep strength for the NiAl-Laves phase alloys compared to binary NiAl is

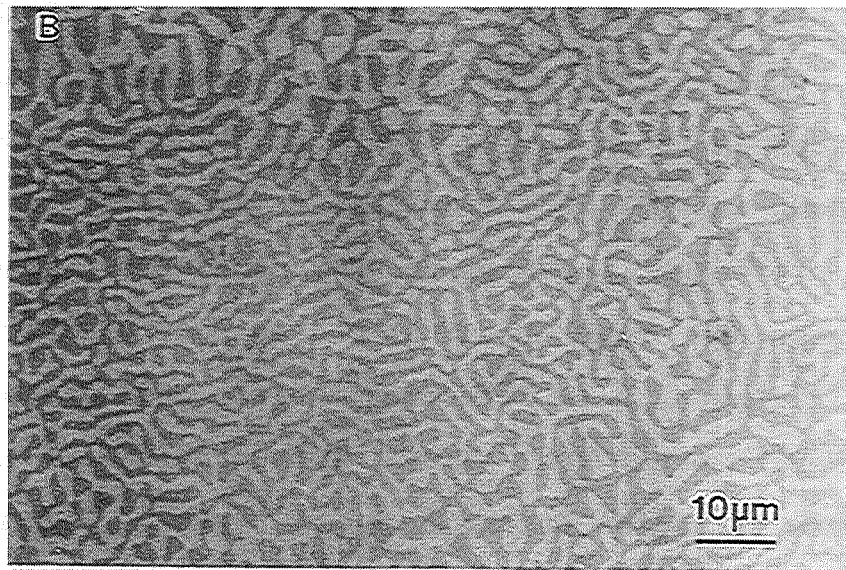
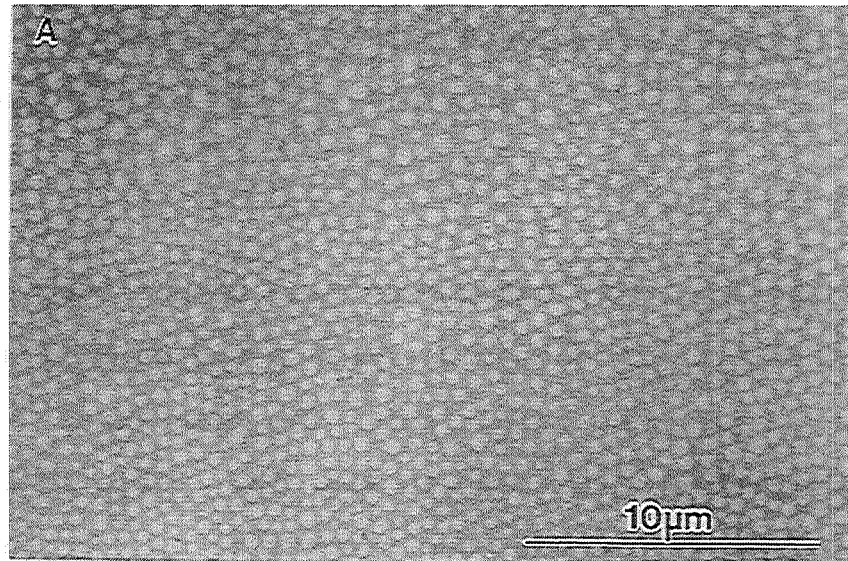


**Figure 53:** (SEM-4QBS) Transverse microstructures of NiAl-34Cr and NiAl-15.5Ta. a) NiAl-34Cr, showing Cr rods in a NiAl matrix, b) NiAl-15.5Ta, showing NiAlTa lamellae in a NiAl matrix.



Table 13: Summary of two-phase alloys

Eutectic (atomic %)	Phases	T <sub>Eut.</sub> (K)	Creep <sup>a</sup> (MPa)	K <sub>I</sub> (MPa√m)
β-9Mo	β-α	1778	80	15
β-34Cr	β-α	1723	140	20
β-28Cr-6Mo	β-α	1723	160	22
β-40V	β-α	1633	40	32
β-16.5Nb	β-L	1710	150	5
β-15.5Ta	β-L	1833	280	5

<sup>a</sup> Creep strength (compression): strain rate 10<sup>-6</sup> per second at 1% true strain, 1300 K.

β: NiAl α: solid solution metal phase L: Laves

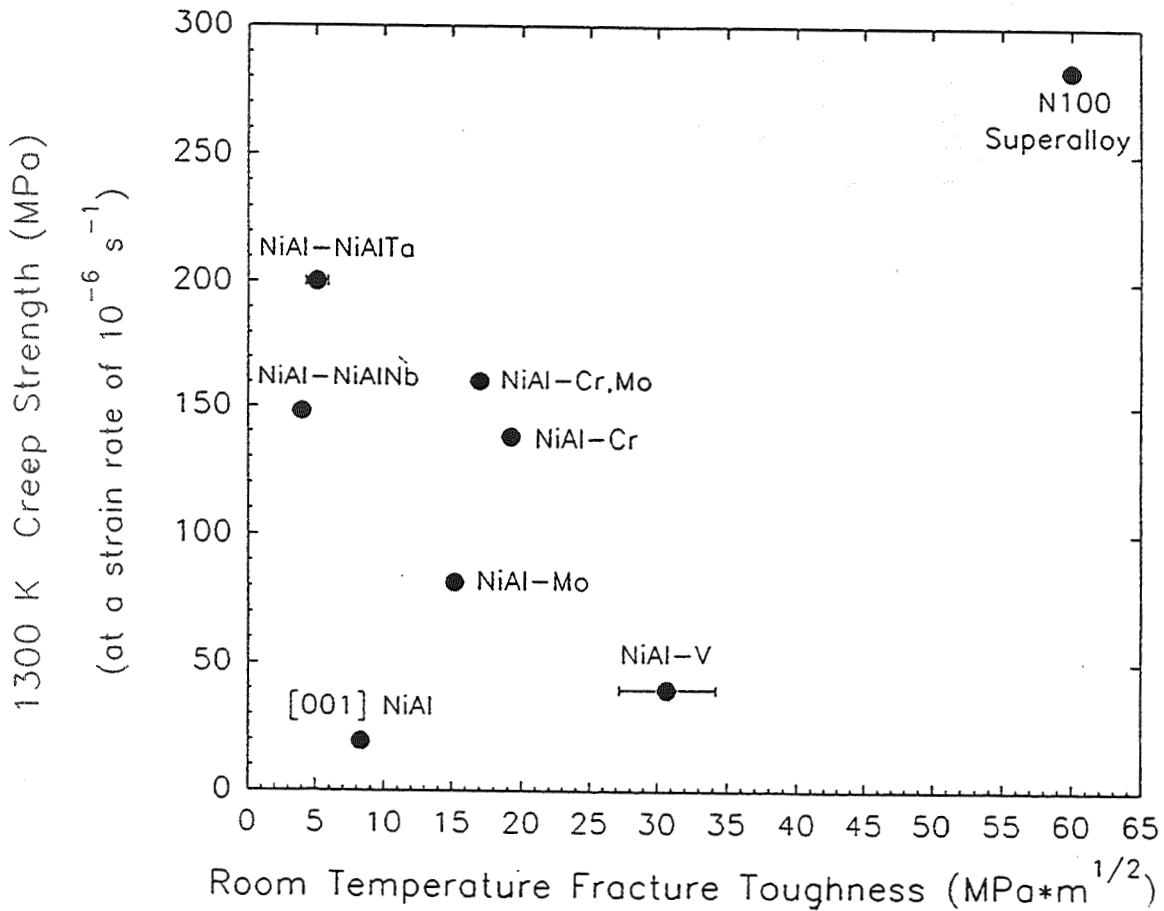
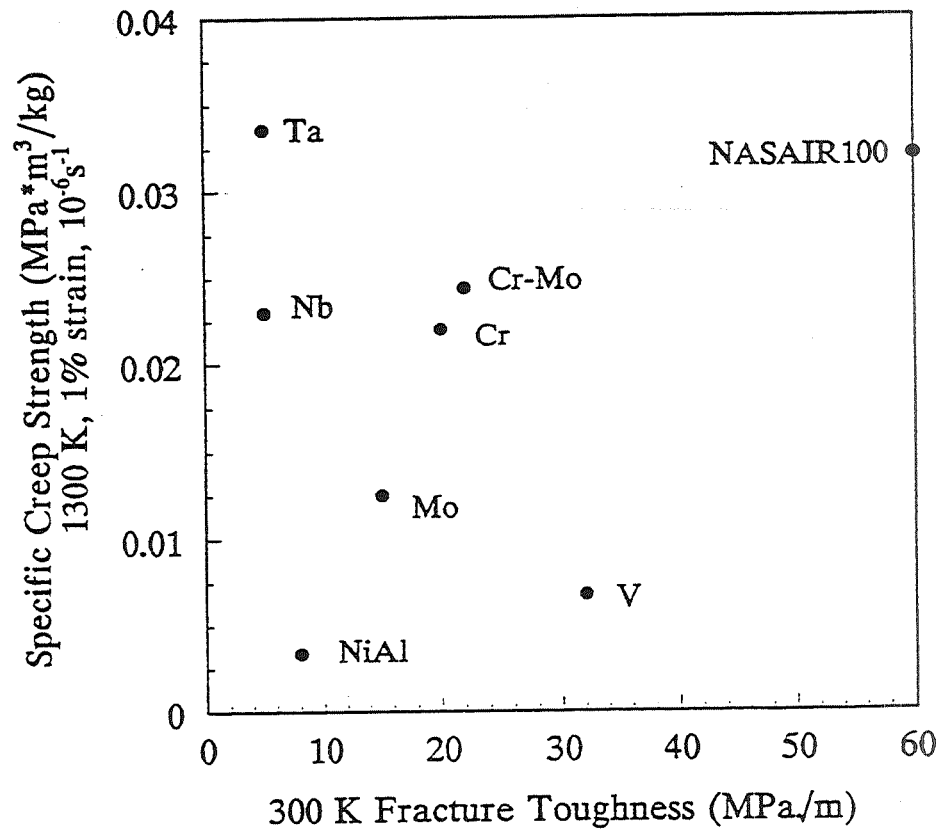


Figure 54: Performance plot of the two-phase eutectic alloys. Shown is a combination of 1300 K compressive strength (at 1% strain and a strain rate of 10<sup>-6</sup> s<sup>-1</sup>) and room temperature fracture toughness.



**Figure 55:** The specific performance plot (same as Fig. 26) showing the combination of density compensated 1300 K strength and room temperature fracture toughness.

not gained at the expense of fracture toughness. The NiAl-metal phase alloys, on the other hand, exhibit a factor of two or three increase in fracture toughness, but generally possess only moderate improvement in creep strength over that of binary NiAl. An NiAl-28Cr-6Mo alloy has the best combination of properties of any two-phase eutectic composite studied to date.

It should be noted that there are significant differences in the melting temperatures of these eutectic alloys. While the homologous temperature varies with alloy composition for the 1300 K screening test, the absolute, density compensated values are more directly applicable to structural design. Furthermore, the choice of air for the screening test atmosphere was chosen as a secondary check for oxidation resistance. Therefore, the two major drawbacks to modification of NiAl by eutectic alloying, i.e., melting temperature depression and changes in oxidation resistance, are addressed in this investigation.

## 6. SUMMARY

Two very important observations were made from the results of the early eutectic studies [16,20,23]. First, Laves phases are most effective at improving the creep

strength. Second, metal phases are best for improving the room temperature fracture toughness.

The results of the screening tests are summarized in the performance plot shown in Figure 54. This type of plot clearly shows the ability of the reinforcing phase to enhance both fracture toughness and creep strength. When compensated for material density, the eutectic alloys compare more favorably with the super alloy, Fig. 55.

Many aspects concerning the microstructure of NiAl-based, eutectic alloys have been confirmed or established. The CELZ process provides higher purity material with slight deviations in microstructure compared to Bridgman processed material. Fewer variations in the microstructure are found in Bridgman processed material because of the dynamic, interactive nature of the CELZ process; the ingot is an integral part of the power supply in the CELZ process. The effects of these deviations are severe for the elevated temperature properties. Under four point bending conditions, the effect depends on the proximity of the banding to the notch in the specimen (as it does for the Bridgman material). Further comparison between processing techniques for the eutectic alloys is difficult because mechanical property data for Bridgman processed NiAl-9Mo and NiAl-40V is sparse.

Room temperature fracture toughness values are considered representative of the alloys tested, unless banding coincides with the notch in the four point bend specimens. The composite structures exhibit superior creep strength. However, the elevated temperature yield strength and creep strength values determined in this investigation are considered minimum values because of the banding present in the microstructures. The banded regions are primarily single phase and are weaker than the composite material.

...  
...  
...  
...  
...  
...  
...  
...  
...

**REFERENCES**

- [1] H.E. Cline, J.L. Walter, E. Lifshin, and R.R. Russell, *Met. Trans.*, 2(1971)189.
- [2] V.Ya Markiv, V.V. Burnashova, L.I. Pryakhina, and K.P. Myasnikova, *Izv. Akad. Nauk SSSR, Met.*, 5(1969)180.
- [3] P.R. Subramanian, M.G. Mendiratta, D.B. Miracle, and D.M. Dimiduk, in "Intermetallic Matrix Composites", D.L. Anton et al., eds., *MRS Symp.Proc.*, 194(1990)147.
- [4] P.W. Pellegrini and J.J. Hutta, *J. Crystal Growth*, 42(1977)536.
- [5] E. Stover, Rep. #WADC TDR60-184, Part VII, 2, General Electric Co., (1966).
- [6] R. Darolia, D.F. Lahrman, R.D. Field, J.R. Dobbs, K.M. Chan, E.H. Goldman, and D.G. Konitzer, in "Ordered Intermetallics-Physical Metallurgy and Mechanical Behavior", C.T. Liu et al., eds., The Netherlands, Kluwer Academic., (1992)679.
- [7] J.D. Cotton, M.J. Kaufman, and R.D. Noebe, *Scripta Metall. Mater.*, 25(1991)1827.
- [8] V.A. Raman and K. Schubert, *Z. Metallkde.*, 56(1965)99.
- [9] K.S. Kumar, *Int. Mat. Rev.*, 35(1990)293.
- [10] R. Darolia, D.F. Lahrman, R.D. Field and A.J. Freeman, *MRS Symp.Proc.*, 133(1989)113.
- [11] E. Tietz and W. Wilson, *Behavior and Properties of Refractory Metals*, Stanford University Press, (1965)334.
- [12] W.A. Tiller, "Liquid Metals and Solidification", ASM Cleveland, OH, (1958)276.
- [13] R.R. Mollard and M.C. Flemings, *Trans. AIME*, 239(1967)1534.
- [14] X.F. Chen, S.M. Joslin, B.F. Oliver, and C.R. Brooks, *Scripta Metall. Mater.*, 29(1993)1439.
- [15] D.R. Johnson, NASA Contr. Rep. 195333, (1994).
- [16] D.R. Johnson, S.M. Joslin, R.D. Reviere, B.F. Oliver, and R.D. Noebe, in "Processing and Fabrication of Advanced Materials for High Temperature Applications-II", V.A. Ravi and T.S. Srivatsan, eds., TMS, (1993)77.

- [17] R.D. Noebe Tech. Memo. 106534, (1994).
- [18] G. Sauthoff, in "Proceedings of International Symposium on Intermetallic Compounds-Structure and Mechanical Properties", JIMIS-6, Jap. Inst. Met., (1991)371.
- [19] G. Sauthoff, in "Structural Intermetallics", R.Darolia et al., eds., TMS, (1993)845.
- [20] D. R. Johnson, S. M. Joslin, B. F. Oliver, R. D. Noebe and J. D. Whittenberger, in "Processing Materials for Properties", H. Henein and T. Oki, eds., TMS, Warrendale, PA, (1993) 865.
- [21] D.R. Johnson, S.M. Jolsin, B.F. Oliver, R.D. Noebe, and J.D. Whittenberger, in "Intermetallic Matrix Composites II", D. Miracle, J. Graves, and D. Anton, eds., MRS Symp. Proc. 273(1992)87.
- [22] I. Jung, M. Rudy, and G. Sauthoff, in High-Temperature Ordered Intermetallic Alloys II, MRS Symp. Proc. 81(1987)263.
- [23] J.D. Whittenberger, R.D. Reviere, R.D. Noebe, and B.F. Oliver, Scripta Metall. Mater., 26(1992)987.



**PART VI: POLYPHASE IN-SITU COMPOSITES**

## 1. INTRODUCTION

Based on the mechanical property data for the binary eutectic alloys, a new direction was taken in an effort to produce ternary eutectic composites which combine both metallic and intermetallic reinforcements with an NiAl matrix. The intended combination of phases is not always thermodynamically feasible. Hence, combining known binary eutectic alloys to form a ternary eutectic does not guarantee success, but it is a good place to start. Quaternary phase diagram information would be invaluable, but does not exist for the composition ranges of interest. Available phase diagram information usually covers only the nickel-rich corner of the alloy system, i.e., for superalloy development. However, existing binary and the few ternary phase diagrams have proven useful in the choice of alloy systems and compositions to pursue.

The choice of Zr and Nb as alloying additions in this study is based on known phase relationships with the matrix phase. For example, sufficient Zr additions are known to cause precipitation of the Heusler phase  $\text{Ni}_2\text{AlZr}$ . The crystal structure of this phase may be considered a further ordering of the B2 structure on the Al sub-lattice, Fig. 56. Zirconium is also selected because of its beneficial effect on the high temperature properties and oxidation resistance of NiAl [1,2]. A Laves phase results from addition of Nb or

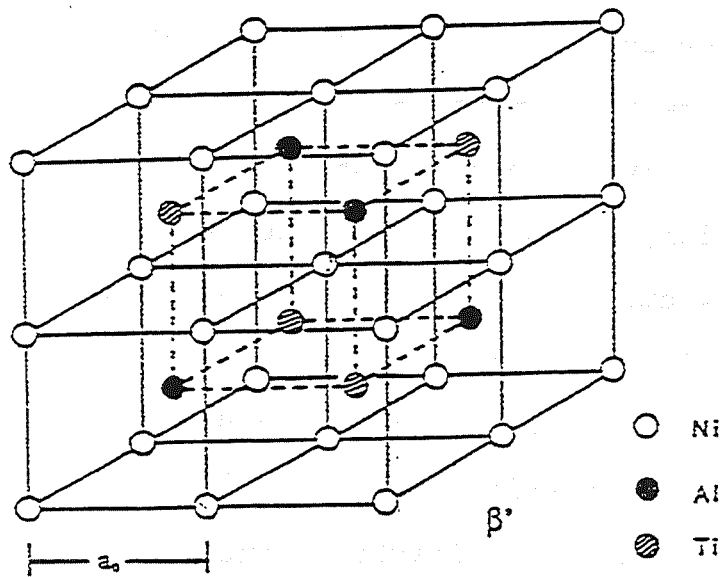


Figure 56: The crystal structure of  $\text{Ni}_2\text{AlZr}$ , Heusler-type phase.

Ta to NiAl [3-7]. Both types of intermetallic phases have shown the potential to significantly improve the creep strength over that of single phase NiAl.

The known eutectics based on NiAl and a disordered metallic solid solution include: NiAl-34Cr, NiAl-28Cr-6Mo, NiAl-40V, NiAl-9Mo, and others with Re and W. The NiAl-Re and NiAl-W eutectics contain a low volume fraction of metallic reinforcement and are not considered in this research. In the absence of specific phase diagram information, a logical first approach for identification of a ternary eutectic alloy is to combine a known NiAl-intermetallic eutectic with a known NiAl-metallic eutectic. As mentioned, thermodynamic considerations dictate the actual phase relations independent of experimental intent. Variations in volume fractions and phase constitution of the new alloy are to be expected. To determine the location of an eutectic, a series of arc melted buttons were made with the choice of each new composition based on the knowledge gained from the microstructures of previous alloys. Once a promising microstructure/composition had been found, a precursor ingot was vacuum induction melted, cast in a chilled copper mold, and directionally solidified.

In all, six three-phase alloys have been identified and processed at the University of Tennessee. Only the NiAl-15Zr-15V, NiAl-12Nb-36V, and three NiAl-Nb-Mo alloys are

presented here; the other polyphase composites have been presented by Johnson [4]. The focus of this part is identification, directional solidification, and mechanical property evaluation of polyphase in-situ composites based on NiAl.

## 2. EXPERIMENTAL PROCEDURE

Each directionally solidified alloy has been characterized on the basis of density, microstructure, phase constitution, and room temperature fracture toughness. The 1300 K creep strength was determined for selected alloys. Elevated temperature testing was performed in air as a check for oxidation resistance and was described in PART III. Density measurements were made using an immersion technique at NASA-LeRC. The room temperature fracture toughness was determined using the single edge-notched 4-point bend test also described in PART III. The NiAl-15Zr-15V alloy was further characterized using differential thermal analysis and X-ray analysis for phase identification; both were performed at NASA-LeRC.

## 2.1 Processing

Table 14 is a summary of the processing conditions used for directional solidification of each alloy. All of the NiAl-based alloys are processed using the same induction coil/eddy current plate assembly as for the two-phase eutectic alloys and NiAl. As expected, the ternary eutectic alloys require less power to establish and maintain the liquid zone due to their lower melting temperatures. The lower power levels and slightly higher density of these alloys combine to reduce the tendency to over levitate. Hence, the ingots are generally processed at full diameter (25.4 mm) to increase the yield of material from each run.

Table 14: Processing conditions for three-phase alloys.

COMPOSITION (NiAl-)	GROWTH RATE (cm/hr)	ROTATION (rpm)	# OF PASSES
15Zr-15V	1.9	100	1
15Zr-15V	1.9	100	1
15Zr-15V	10.2	100	1
12Nb-36V	1.9	90	2
3Nb-10Mo	2.0	120	1
5Nb-10Mo	1.9	75	1
13.6Nb-18Mo	1.9	100	2

Based on the purity levels of the binary eutectics, the higher concentrations of alloying elements in the ternary eutectic alloys are expected to decrease the purity. A high emissivity phase invariably precipitates on the surface of the zone for the alloys containing vanadium, even after

grinding and reprocessing. However, the interior regions of the ingots appear to be free of the high emissivity phase.

## 2.2 Microstructure and Mechanical Property Testing

The microstructure of each alloy was characterized using both optical and scanning electron microscopy. Standard metallographic techniques were used to prepare the specimens. Volume fractions of the constituent phases were determined using digital image analysis when the phase contrast was sufficient. Otherwise, a line intercept method was used to estimate the volume fractions.

The 1300 K creep tests were performed at NASA-LeRC for the NiAl-15Zr-15V (ZrV) eutectic and the non-eutectic NiAl-Nb-Mo alloys only. The Zr-V eutectic was tested first and performed poorly due to catastrophic oxidation of the V phase. Therefore, the NiAl-12Nb-36V alloy was not tested at elevated temperatures, leaving more material for room temperature bend testing.

The 4-point bend test described in PART III was used to measure the room temperature fracture toughness of each composite. Specimen dimensions were the same as those for NiAl and the binary eutectics allowing direct comparison of the data between alloys. It is unfortunate that the interesting microstructures of the vanadium alloys are

subject to catastrophic oxidation at elevated temperatures. However, they are interesting from the perspective of understanding the mechanisms which contribute to the room temperature fracture toughness of NiAl-based in-situ composites.

### **2.3 Differential Thermal Analysis and X-ray Diffraction Analysis**

The NiAl-15Zr-15V alloy was characterized using differential thermal analysis (DTA) and X-ray diffraction analysis. The DTA technique was used to obtain information concerning the nature of the solidification event which produced the observed microstructure. The X-ray diffraction analysis was used to identify the constituent phases of the composite alloy.

Differential thermal analysis involved the controlled heating and cooling of both a small sample of the alloy and an empty crucible. Both were heated at constant power input resulting in a heating rate of about 10 K/min for the alloy specimen. The energy of phase transformation and differences in heat capacity cause a difference in temperature between the crucibles. The difference in temperature was recorded as a function of specimen temperature. A peak in the temperature difference curve



indicates that a transformation occurred at that temperature. On cooling, the thermal arrest associated with a phase transformation creates an inverted spike in the temperature difference curve. If the alloy is on the ternary eutectic composition, only one peak will occur (at the melting point). Otherwise, interpretation of the position and number of peaks provides useful information as to the true nature of the microstructural development of the composite.

An APD1700 automated diffractometer system was used to identify the phases present in a representative sample of the NiAl-15Zr-15V alloy. Peak angles in the range of  $10^\circ$  to  $100^\circ$  were determined using Cu  $K\alpha$  radiation. Peak positions were determined by locating the top of the smoothed data peaks. The peak angles were used to calculate the lattice spacings which were then used to identify the phases present.

Energy dispersive spectrometry (EDS) was used to analyze the phase compositions when the scale of the microstructure permitted. Often the eutectic structure was too fine, such that beam spreading prevented the acquisition of a representative spectrum from only one phase.

### 3. MICROSTRUCTURES

The microstructures of the ingots used in mechanical property evaluation are shown in Fig. 57. Based on the microstructure, the NiAl-15Zr-15V alloy is very near the eutectic composition. The alignment of the microstructure is excellent for this alloy. A few regions of primary phase are observed in the microstructure, representing ~2% of the cross-sectional area as determined by digital image analysis of a backscattered electron image. The volume fraction of each phase is presented in Table 15.

The NiAl-15Zr-15V alloy consists of  $\text{Ni}_2\text{AlZr}$  and NiAl lamellae with  $\text{ZrV}_2$  rods aligned in the growth direction at the lamellar interfaces. The lamellar spacing is on the order of  $2\mu\text{m}$ . The  $\text{ZrV}_2$  rods are approximately  $1\mu\text{m}$  in diameter. Accurate determination of the phase compositions is hindered by the fine scale of the microstructure. Large single phase areas and the coarsest eutectic areas were targeted for EDS analysis. The EDS results are shown by the estimated phase boundaries in the quaternary phase diagram (Fig. 58(a)).

The NiAl-12Nb-36V ingot contains a significant amount of blocky two-phase regions and is therefore not precisely on the eutectic composition. The most intriguing aspect of this microstructure is the fact that all three phases make contact in nearly equal proportions. Furthermore, the phase

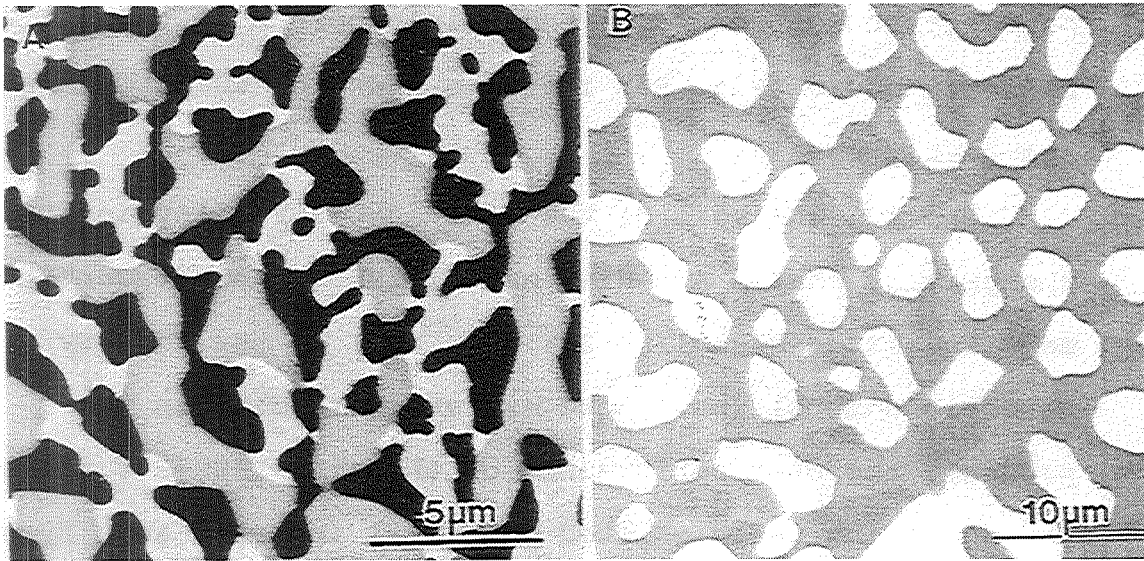


Figure 57: Transverse microstructures of a) NiAl-15Zr-15V and b) NiAl-12Nb-36V.

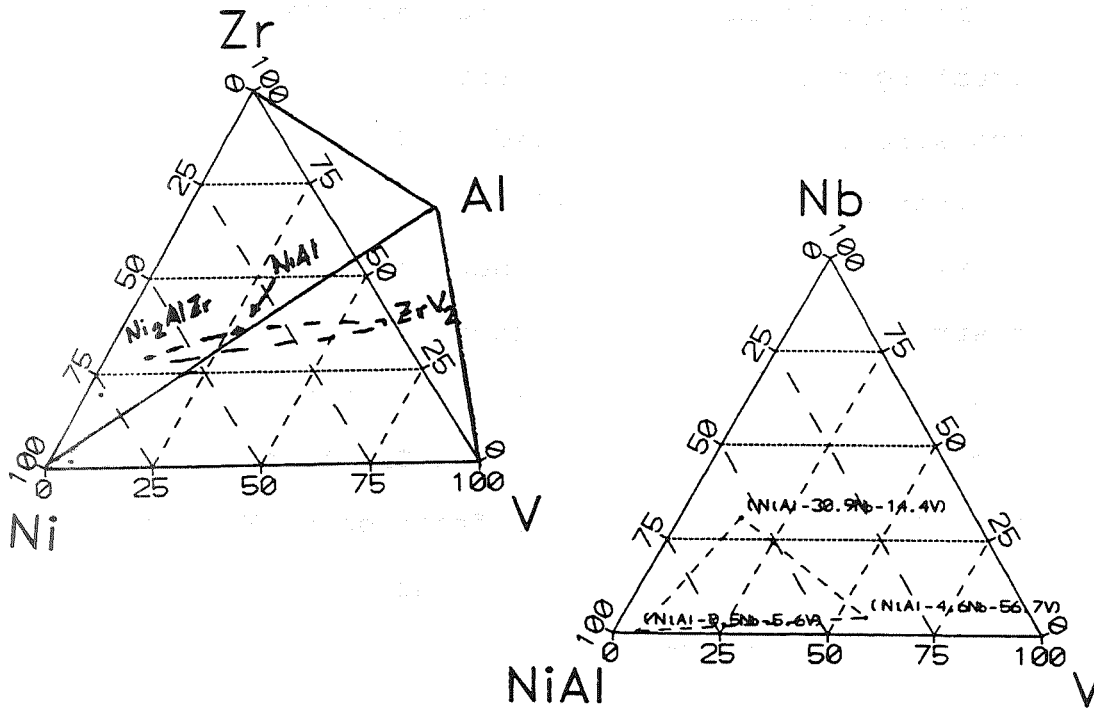


Figure 58: Schematic phase diagrams for the Ni-Al-Zr-V and NiAl-Nb-V systems.

boundary angles formed at the triple points in the microstructure (Fig. 59) indicate that the surface energies are nearly equal.

The EDS analysis of the NiAl-12Nb-36V alloy indicates the primary phases are NiAl and NiAlNb. A subsequent button melt indicates NiAl-11Nb-33V is closer to the ternary eutectic composition. However, at this point in the program, the poor performance of the NiAl-15Zr-15V alloy in the screening tests shifted practical interest away from vanadium containing alloys. Therefore, further investment in the NiAl-Nb-V system was determined to be imprudent.

The NiAl-Nb-Mo alloys are not eutectic, but exhibit an interesting three-dimensional network of Mo dendrites. These alloys were directionally solidified in order to ascertain the effect of a 3-dimensional, ductile phase network on fracture toughness. On the other hand, the rest of the microstructure is very heterogeneous and complicates the data interpretation. Three different compositions were characterized: NiAl-3Nb-10Mo, NiAl-5Nb-10Mo and NiAl-13.6Nb-18Mo. As expected, the volume fraction of Mo dendrites increases with increasing Mo content, Table 15.

In the NiAl-Nb-Mo system, the original intent was to locate a ternary eutectic containing NiAl, a metallic Mo-based solid solution, and the Laves phase NiAlNb. Although these three phases are present in each of the alloys, they

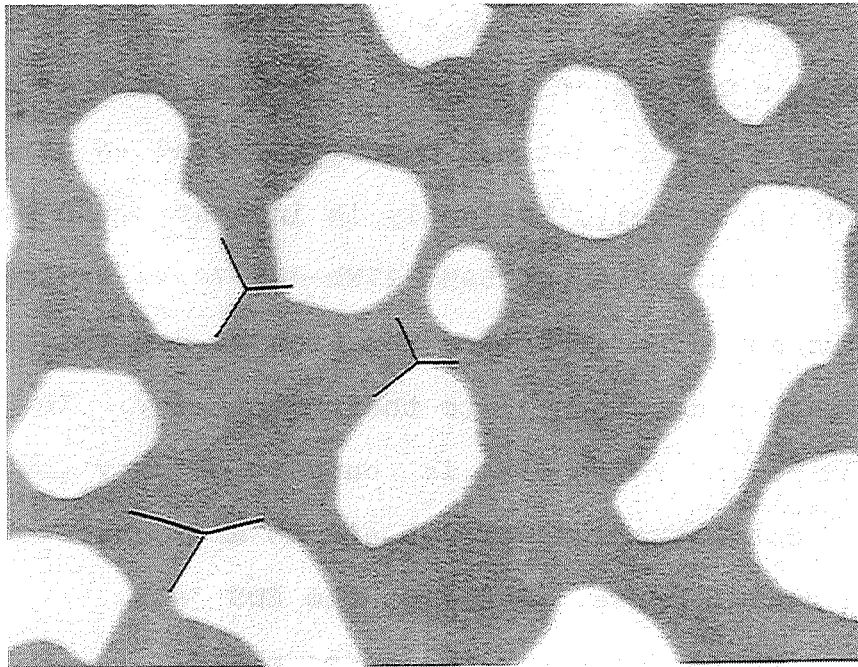


**Figure 59:** Phase boundary angles in NiAl-12Nb-36V indicating the similarity of the surface energies between the three phases.

**Table 15: Volume fraction of phases for polyphase alloys.**

PHASE	15Zr-15V	12Nb-36V	3Nb-10Mo	5Nb-10Mo	13.6Nb-18Mo
NiAl	0.49	0.27	0.81	0.57	0.20
Laves	0	0.49	0.04	0.37	0.54
Heusler	0.35	0	0	0	0
Metallic	0	0.24	0.14	0.06	0.23
Other	0.16	0	0.01	0	0.03

exist as single and two-phase dendrites. The two phase dendrites consists of either NiAl and Mo or NiAl and NiAlNb. A ternary eutectic has not been identified in this system.

More precisely, EDS analysis indicates the Mo dendrites are a solid solution of 59Mo-27Nb-7Ni-7Al. Analysis of the fracture surfaces indicates the high Nb content in the Mo dendrites is detrimental to their ductility. The solubility of both Nb and Mo in NiAl is found to be very low, less than 1 at%. Concentrations of 8.5 at% Mo are consistently found in the NiAlNb phase. Based on the EDS data, it appears that Mo substitutes for Nb in the Laves phase. The EDS results are also shown in Fig. 58(b).

It should be noted that only one of the three-phase alloys listed in Table 15 contains a Heusler (H) phase. The creep strength of the Heusler phase is the highest of those listed in Table 15 [8]. However, the fracture toughness of NiAl-15Zr-15V is one of the lowest. In terms of creep strength, the identification and characterization of NiAl-H-Metal ternary eutectic alloys represents a promising area for future development.

#### 4. FRACTURE TOUGHNESS

The room temperature fracture toughness of each three-phase alloy is listed in Table 16. The NiAl-12Nb-36V alloy contains a well distributed metallic phase, but unfortunately the high volume fraction of brittle NiAlNb dominates the fracture toughness. In addition, the microstructure contains a large volume fraction of non-eutectic regions. Thus, the resulting fracture toughness ( $6.8 \pm 0.7$  MPa $\sqrt{m}$ ) is less than that of single phase HP-NiAl by approximately 40%. Even though the microstructure is composed entirely of brittle intermetallic phases, the NiAl-15Zr-15V alloy has a fracture toughness of  $6.9 \pm 2.3$  MPa $\sqrt{m}$  and is essentially independent of heat treatment and the growth conditions listed in Table 16. The NiAl-Nb-Mo alloys show a decrease in fracture toughness of 19 to 50% compared

Table 16: Room temperature fracture toughness,  $K_{Ic}$ .

COMPOSITION (NiAl-)	$K_{Ic}$ (MPa $\sqrt{m}$ )	CONDITION
15Zr-15V	$6.9 \pm 2.3$	AP
	6.5	1300 K/2hr/WQ
	6.9	1300 K/2hr/FC
	$5.8 \pm 0.4$	AP@1.9cm/h (HIGH R)
	$4.9 \pm 0.8$	AP@10cm/h (HIGH R)
12Nb-36V	$6.8 \pm 0.7$	AP
3Nb-10Mo	$9.1 \pm 0.9$	AP
5Nb-10Mo	$5.6 \pm 1.7$	AP
13.6Nb-18Mo	$6.0 \pm 0.7$	AP

AP - as-processed

HIGH R - high thermal gradient (cooling jacket used)

WQ - water quenched

FC - furnace cooled at 5 K/min.

to HP-NiAl. In terms of fracture toughness, the importance of a ductile, metallic phase is clear, but the ductility of the Mo phase within this composite suffers with the addition of Nb. Further discussion concerning fracture toughness is contained in Part VII.

## 5. ELEVATED TEMPERATURE PROPERTIES

Of the V-containing alloys, only the NiAl-15Zr-15V (ZrV) eutectic was tested at elevated temperature. The poor oxidation resistance of vanadium in general, together with the poor performance of the ZrV eutectic, suggest that further high temperature testing of alloys containing vanadium is not warranted. The results of the elevated temperature testing is presented in Table 17 and in Fig. 60. Though the V-containing alloys are not suitable for high temperature structural applications, characterization of their creep behavior in an inert atmosphere would be an interesting topic for future research.

All of the NiAl-Nb-Mo alloys were tested in air at 1200 and 1300 K. The results indicate that the creep strength increases with increasing Nb content, Fig. 60. Therefore, additional tests were performed at 1400 K on the alloys with higher Nb content. The superalloy compression platens deformed during testing of the NiAl-13.6Nb-18Mo alloy over



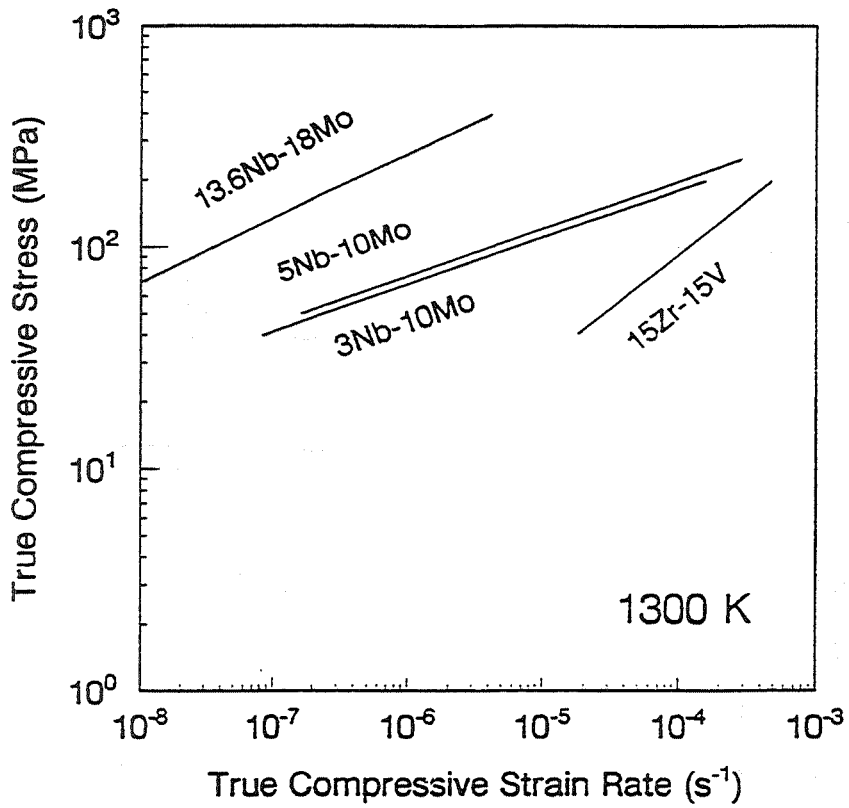


Figure 60: The 1300 K compressive strength as a function of strain rate for the three-phase alloys.

Table 17: 1300 K true compressive yield strength at 1% true strain. Initial strain rate:  $2 \times 10^{-6} \text{ s}^{-1}$ .

COMPOSITION (NiAl-)	CREEP BEHAVIOR	CREEP STRENGTH (MPa)
15Zr-15V	$\dot{\epsilon} = (8.79 \times 10^6) \sigma^{2.05}$	9.8
3Nb-10Mo	$\dot{\epsilon} = 2.44 \times 10^{-15} \sigma^{4.70}$	74
5Nb-10Mo	$\dot{\epsilon} = 2.08 \times 10^3 \sigma^{4.66} \exp\left(\frac{-448.7}{RT}\right)$	89
13.6Nb-18Mo	$\dot{\epsilon} = 40.9 \sigma^{3.45} \exp\left(\frac{-397.2}{RT}\right)$	262

1200 K to 1400 K. The stress exponents are at the lower end of the range of values expected for dislocation climb controlled behavior, Table 17. The same is observed for the NiAl-40V alloy. The change in stress exponent indicates a change in the deformation mechanism. The two most likely reasons for this behavior are the change in homologous test temperature with the addition of solute and the effect of the solute on dislocation mobility. Both of these will affect which deformation mechanism dominates the creep behavior and the value of the stress exponent. The NiAl-13.6Nb-18Mo alloy has a large volume fraction of NiAlNb in the microstructure. In fact, the stress exponent and activation energy are similar to that of the two-phase eutectic, NiAl-16.5Nb (lamellar NiAl and NiAlNb). The

activation energies are higher for the NiAl-Nb-Mo alloys than binary NiAl.

## 6. DIFFERENTIAL THERMAL ANALYSIS (DTA)

The DTA results for the NiAl-15Zr-15V alloy are shown in Fig. 61. There are four peaks evident on both heating and cooling. Thus, four phase transformations or ordering reactions occur over the temperature range 1273 K to 2073 K.

The temperature differential peaks are more clearly defined for the cooling curve (Fig. 61). On heating, a small peak occurs at 1475 K (1202°C) prior to the largest peak at 1513 K (1240°C), followed by a shoulder (~1533 K, 1260°C), and finally another small peak at ~1648 K (1375°C). On cooling, a small peak occurs at 1621 K (1348°C), followed by another small peak at 1503 K (1230°C), and the largest peak at 1474 K (1201°C). The lowest temperature peak is nearly masked entirely by the large 1474 K peak. Hence, all four peaks are evident on both heating and cooling. Slight differences in peak height and position are expected between these curves due to undercooling and the dynamics involved in thermodynamic equilibrium.

The Zr-V phase diagram is shown in Fig. 62. A peritectic reaction occurs in the binary Zr-V system between  $ZrV_2$  and V at 1573 K (1300°C) [9]. The solubility of Zr in

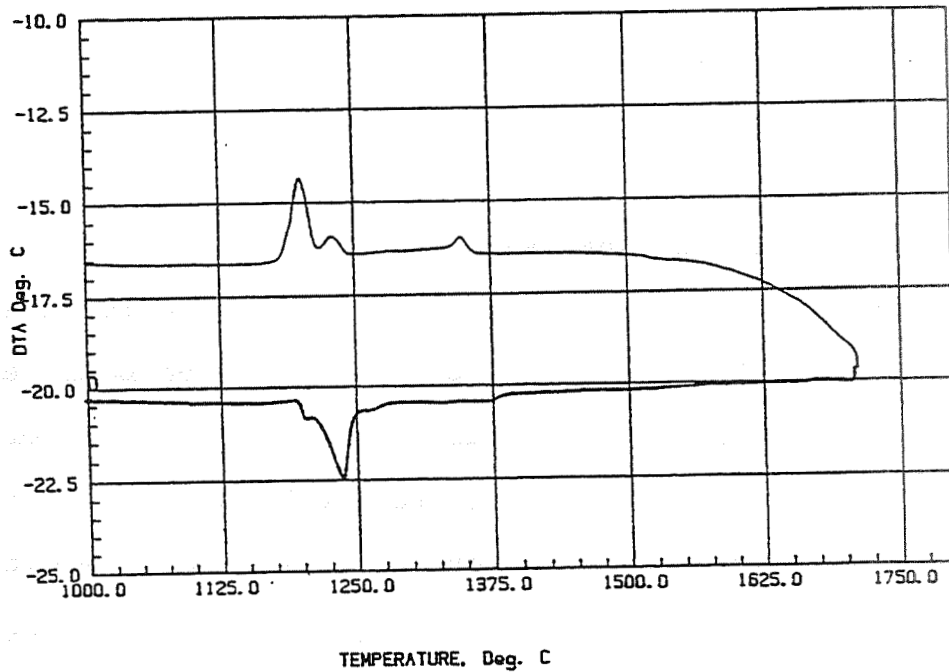


Figure 61: Results of DTA for NiAl-15Zr-15V. The eutectic temperature is 1493 K.

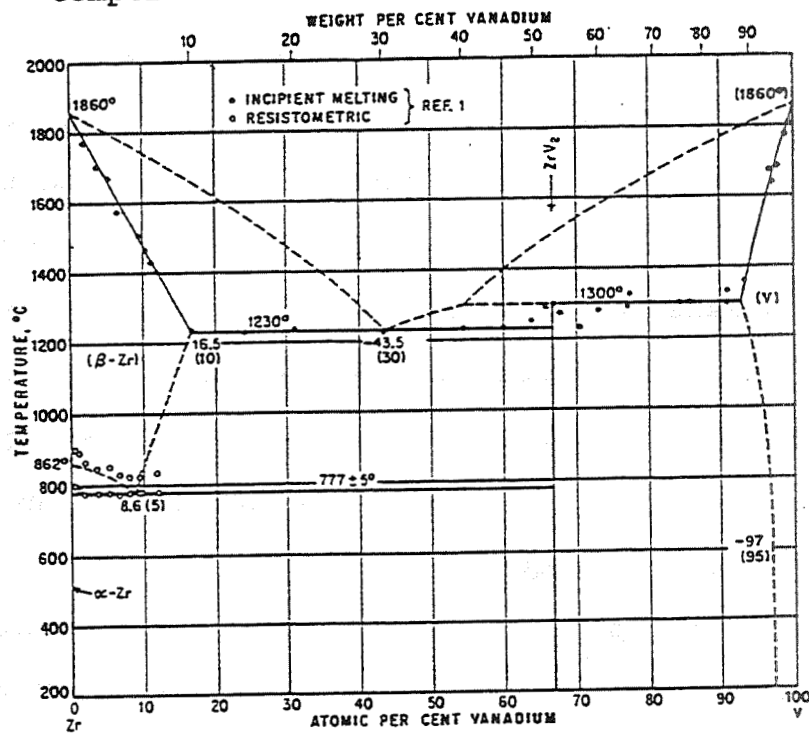


Figure 62: The Zr-V phase diagram [9].

NiAl is low. Both a Heusler-type phase ( $\text{Ni}_2\text{AlZr}$ ) and a Laves phase ( $\text{NiAlZr}$ ) exist in the Ni-Al-Zr system as shown in the 1073 K isotherm (Fig. 63). Vanadium has considerable solubility in NiAl and forms an eutectic with a disordered vanadium solid solution at 1633 K and 40 at% V.

From the microstructural, X-ray, and available phase diagram information, the DTA peaks may be attributed to solidification of a primary single phase, followed by two-phase dendrites, and finally the ternary eutectic. Based on EDS data the composition of the primary dendrites is V-24Al-11Ni. Thus, the 1613 K peak may be attributed to solidification of primary vanadium solid solution which accounts for only 2% of the total volume.

On cooling, the next peak must be due to the solidification of two-phase dendrites. Such dendrites are easily observed in the as-cast precursor ingots, but not in the directionally solidified (DS) ingot. This observation supports the fact that the peak is better defined in the cooling curve. Alternatively, a band of  $\text{Ni}_2\text{AlZr}$  is observed between the primary NiAl dendrites and the ternary eutectic in the DS ingot, which may also give rise to the small shoulder observed just above the largest peak in the DTA curves.

The largest peak is associated with the ternary eutectic reaction which is responsible for 98% of the

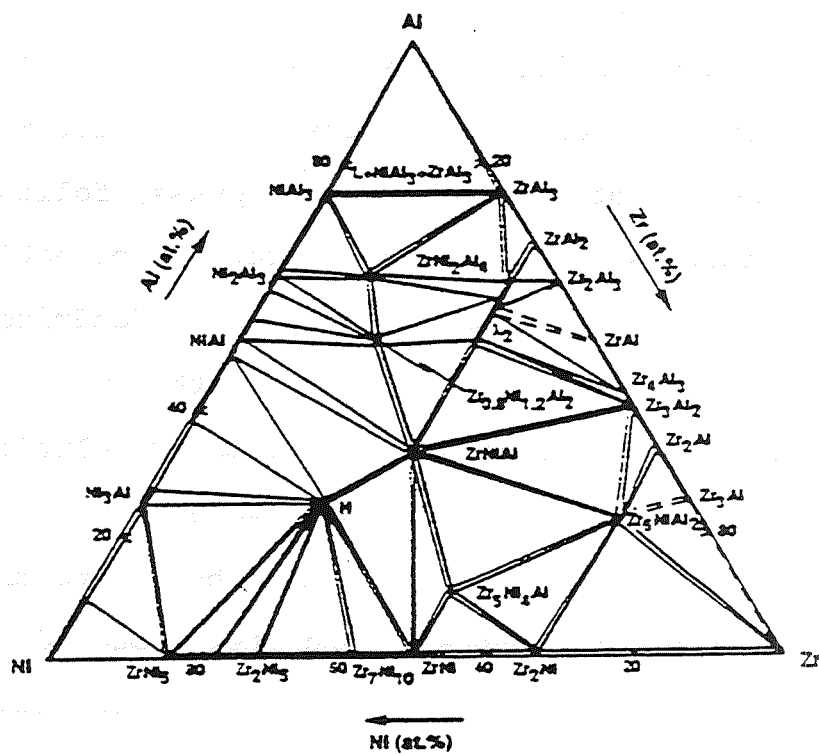


Figure 63: The Ni-Al-Zr isotherm at 1073 K [10].

microstructure. Though no ordering reactions are reported for any of the phases observed in the DS ingot from their melting point to room temperature, other single phase regions are observed in small quantities in the as-cast structure of the precursor ingot. An allotropic phase transformation occurs for pure Zr near 1050 K. Hence, the small peak below the presumed eutectic temperature may possibly be associated with a small amount of Zr solid solution precipitating or going into solution.

The ternary eutectic temperature is therefore 1493 K (1220°C). Further characterization of this alloy was not pursued because it does not fit the characteristics defined in the scope of this research, i.e., it lacks a ductile metallic phase.

## 7. SUMMARY

The room temperature fracture toughness of each three phase alloy has been determined to be inferior to that of HP-NiAl, with the fracture toughness of each falling in the range of 5 to 7 MPa√m. The reason for their poor toughness is most likely a combination of solid solution strengthening of the NiAl and metallic phases (if present) and the relatively high volume fraction of brittle Laves phase reinforcement.

The 1300 K creep strength has been determined for NiAl-15Zr-15V. The poor oxidation resistance of this eutectic is degrading to its high temperature performance. Based on that result, consideration of the NiAl-12Nb-36V alloy for high temperature testing was determined to be unwarranted. The stress exponent for NiAl-15Zr-15V is lower than the other alloys, but the melting temperature is also much lower, i.e., 1300 K is roughly 90% of its melting temperature.

Elevated temperature testing of NiAl-3Nb-10Mo, NiAl-5Nb-10Mo and NiAl-13.6Nb-18Mo has been performed over 1200 to 1300 K. The stress exponent decreases and the strength increases with increasing Nb content in the alloy. The NiAl 5Nb-10Mo and NiAl-13.6Nb-18Mo alloys were also tested at 1400 K. The strength of NiAl-13.6Nb-18Mo approaches that of the superalloy compression platens over the range of test conditions and is near that of NiAl-14.5Ta. Based on the stress exponents, the dominant deformation mechanism is controlled by dislocation climb.

Figure 64 is the performance plot shown in PART VI with all of the three phase alloys developed at the University of Tennessee superimposed for comparison. The poor oxidation resistance of the NiAl-15Zr-15V alloy is evident. Elevated temperature testing of NiAl-12Nb-36V and NiAl-10Ta-33V was not attempted on the basis of performance of the NiAl-15Zr-



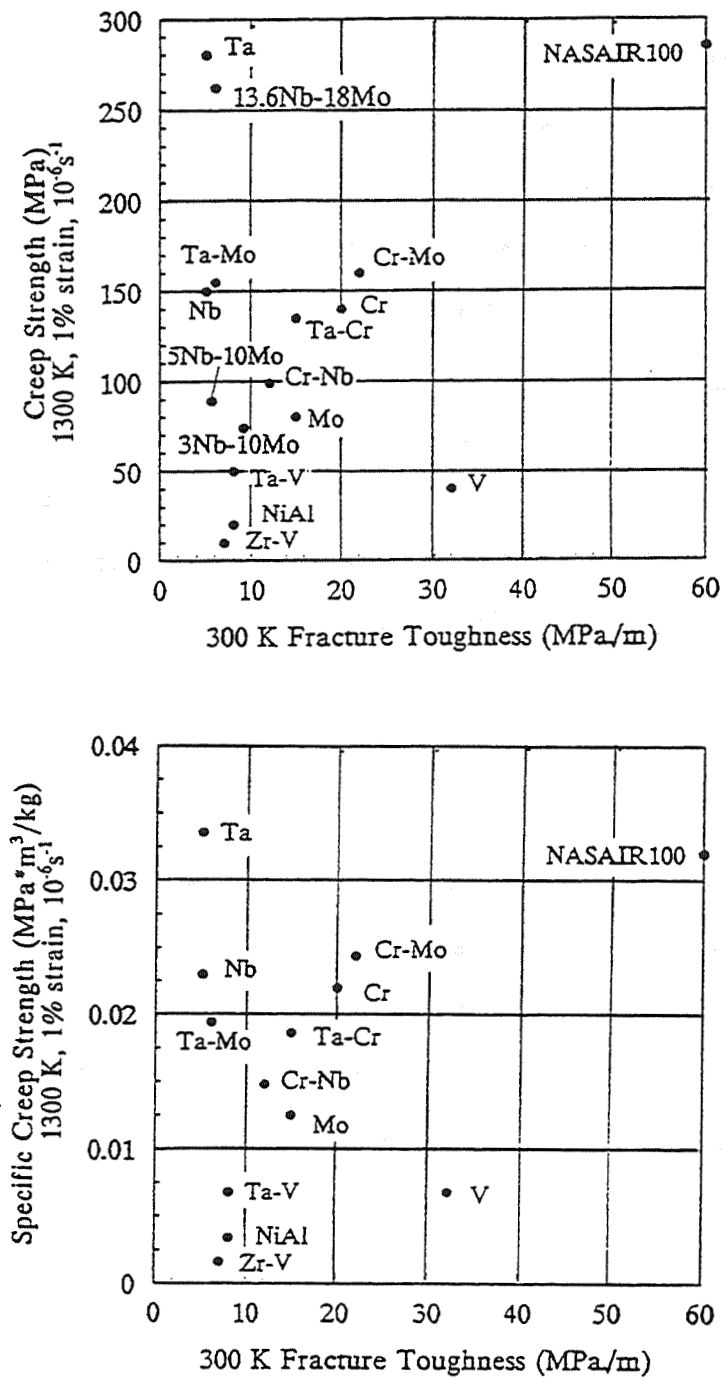


Figure 64: Performance plot and specific performance plot for three-phase alloys. a) 1300 K strength and room temperature fracture toughness and b) specific 1300 K strength and room temperature fracture toughness. (1300 K strength at 1% strain at a strain rate of  $10^{-6} s^{-1}$ ).

15V alloy. The addition of either Laves phase (NiAlTa or NiAlNb) to the two-phase NiAl-V eutectic decreases the fracture toughness compared to both NiAl-40V and NiAl. Furthermore, the melting temperatures of the NiAl-V-X alloys are the lowest of the eutectic alloys identified to date.

A Heusler-type phase has not been successfully incorporated with NiAl and a ductile metallic phase into a ternary eutectic alloy. The closest attempt is the NiAl-15Zr-15V alloy, which unfortunately does not contain a metallic phase. This class of alloys deserves further investigation.

#### **8. CAVEATS CONCERNING MICROSTRUCTURAL OBSERVATIONS**

Laves-type phases such as NiAlNb and NiAlTa form an in-situ composite with NiAl and V where all three phases contact each other in nearly equal proportions. On the other hand, the NiAlTa phase tends to show limited contact with Cr, such that Cr phase is nearly contained within the NiAl lamellae (NiAl-6Ta-33Cr). For Mo, the microstructure consists of NiAl-NiAlTa lamellae with the Mo completely encapsulated within the NiAl. The order of increasing solubility in NiAl for the refractory metal additions is  $V \gg Cr \geq Mo$ . However, the lattice parameter mismatches, determined from selected area diffraction patterns at room

temperature, increase in magnitude as V>Mo>Cr relative to NiAl. The surface energy plays a significant role in determining the relative contact areas between phases. It is odd that the metallic phase with the largest lattice parameter mismatch with NiAl exhibits the largest contact area with both NiAl and Laves phases. However, the lattice parameters may differ at the melting temperature of each alloy. Of the two-phase eutectic alloys, only the Cr phase shows evidence of mismatch dislocations at the interface with NiAl. The interface between NiAl and the Mo phase shows a preference for <110> planes.

... ..  
... ..  
... ..  
... ..  
... ..  
... ..  
... ..  
... ..  
... ..  
... ..

**REFERENCES**

- [1] C.A. Barrett, *Oxidation of Metals*, 30(1988)361.
- [2] R.D. Noebe, *NASA Tech. Memo. 106534*, (1994).
- [3] J.D. Whittenberger, R. Reviere, R.D. Noebe, and B.F. Oliver, *Scripta Metall. Mater.*, 26(1992)987.
- [4] D.R. Johnson, *NASA Contractor Rep. 19533*, (1994).
- [5] G. Sauthoff, *Z. Metallkde.*, 81(1990)855.
- [6] G. Sauthoff, in "*Intermetallic Compounds - Structure and Mechanical Properties*", O. Izumi, ed., *Japan Inst. Metals, Sendai, Japan* (1991)371.
- [7] G. Sauthoff, in "*Structural Intermetallics*", R. Darolia et al., eds., *TMS, Warrendale, PA* (1993)845.
- [8] R. Darolia, *JOM*, March(1991)44.
- [9] M. Hansen, "*Constitution of Binary Alloys*", *McGraw-Hill, NY*, (1958).
- [10] K.S. Kumar, *Int. Mat. Rev.*, 35(1990)293.

**PART VII: FAILURE ANALYSIS**

## 1. INTRODUCTION

The fracture behavior of each in-situ composite is determined by the combination of several individual mechanisms. The magnitude of the contribution from each mechanism depends on the morphology, constraint, and flow characteristics of the constituent phases. In order to characterize the composite fracture toughness the mechanical properties and microstructure of the individual components must be determined. In general, the increase in fracture toughness of the NiAl-metallic phase composites has been attributed to a combination of crack bridging, crack trapping, and crack renucleation, depending on the eutectic morphology [1-8].

The focus of Part VII is to identify which fracture mechanisms are active for each of the directionally solidified composite alloys and evaluate the contribution of crack bridging in each case. Fracture surfaces and microstructures of each alloy were characterized by scanning electron microscopy (SEM). Observations from SEM and, in some cases, transmission electron microscopy (TEM) were used to determine which fracture mechanisms dominate.

Assessment of the crack bridging contribution is accomplished using a small scale bridging model [1-3]. A significant difference between this and previous work is the input parameters used in the model. Previous work on NiAl-

based composites is based on pure, bulk component mechanical properties, primarily because the in-situ properties are unknown. An attempt has been made in this work to measure the elastic properties of the composite and its component phases using a load and displacement sensing indentation technique.

## 2. FRACTURE MECHANISMS

There are several possible fracture mechanisms for brittle matrix composites, including crack bridging, blunting, splitting, trapping, and renucleation [1-8]. In addition, an increase in mobile dislocation density due to the presence of the phase boundaries may contribute to the fracture toughness through enhanced flow processes. For example, both the improved ductility of NiAl due to film softening [9] and the improved fracture resistance of both NiAl [10, 11] and Ni-Al-Fe alloys [12] by prestraining have been attributed to an associated increase in mobile dislocation density.

In terms of crack propagation events, there are two morphological classes of binary composites: rod and lamellar [1,2,13]. In a rod eutectic, the crack has continuous access to the matrix, while in a lamellar eutectic it does not. Crack bridging can increase the



fracture toughness for both eutectic morphologies, provided the flow strength and ductility of the reinforcing phase and the debonding characteristics at the interface are appropriate [1-3]. Crack bridging also occurs when multiple cleavage cracks on parallel planes create a ligament between the cracks [14]. This ligament then requires additional energy to deform and fracture as the crack faces open.

The fracture initiation contribution to the composite toughness depends on the composite morphology [2]. For a rod eutectic, crack trapping increases the resistance to crack initiation by interaction of the reinforcing rods with the matrix [2]. For a lamellar eutectic, a crack in the brittle phase must renucleate in the next brittle layer in order to propagate [2]. The advancing crack may follow the phase boundary leading to crack deflection or may renucleate more than one crack (crack splitting). Both scenarios reduce the crack tip stress intensity, requiring an increase in applied load to further propagate the crack and increase the fracture toughness.

### **3. EXPERIMENTAL PROCEDURE**

The four point bend test described in Part III was used to determine the room temperature fracture toughness of each composite alloy. The resulting fracture surfaces were

characterized by scanning electron microscopy of both the fracture surface and the sides of the bend bars at the failure. The bend bars were polished using standard metallographic techniques prior to testing to allow subsequent observation of the crack path.

The elastic properties of the composite and the individual phases were determined using a NANO<sup>TM</sup> Indenter II, i.e., a load displacement sensing indentation technique (NANO-indentation) [15]. A large indent depth, corresponding to the maximum load, was used to determine the elastic modulus of the composite material. A indenter displacement of 100 $\mu$ m was used to determine the modulus of the individual phases; the size of the resulting indent was too small to resolve optically. As a baseline, the modulus of HP-NiAl was also determined using both maximum load and 100 $\mu$ m indenter displacement tests and compared to the modulus values determined by other means.

The position of each indent was selected manually and verified after testing. The fine scale of the composite microstructures necessitated careful and frequent calibration of the indenter tip positioning because the target areas were often on the order of 5 $\mu$ m or less in diameter. Though the positioning of the indenter was remarkably accurate, thermal expansion caused an inevitable and unpredictable drift in the accuracy with time. For this

reason, the largest areas of each phase were targeted. The variation in modulus with the size of the single phase area was negligible provided the indent was at least two diameters from the nearest phase boundary.

The NANO Indenter II uses a well characterized diamond Berkovich indenter. The load and displacement are recorded during indentation. The geometry and elastic properties of the indenter must be known accurately and precisely. Oliver and Pharr have developed an experimental procedure to determine the indenter shape factor and machine compliance that does not require imaging of the indent [15]. Once these parameters are known, the hardness and modulus of the material are calculated using the load-displacement data. Data from the unloading portion of the load-displacement curve is used to calculate the modulus because the initial unloading is primarily elastic. The actual data represents  $E/(1-\nu^2)$ . The elastic modulus values may be extracted from this data provided Poisson's ration is known. The default value of  $\nu$  is 0.25. For further explanation of the technique and apparatus, the reader is referred to Oliver and Pharr [15].

#### 4. MICROSTRUCTURAL OBSERVATIONS

The binary eutectic composites have been characterized by TEM as well as SEM and NANO-indentation. The ternary eutectic alloys and three phase NiAl-Nb-Mo alloys were characterized by SEM and NANO-indentation only.

##### 4.1 NiAl-Mo Alloys

###### 4.1.1 NiAl(0.1Zr)-9Mo Eutectic

Selected area diffraction patterns confirmed the cube-on-cube orientation relationship between the NiAl matrix and the Mo rods. The volume fraction of the reinforcing Mo rods is 0.11. Figure 65(a) represents the as-processed condition. Figures 65(b) and (c) are from material near the fracture surface, showing dislocation tangles and a much higher dislocation density in the NiAl matrix than for the as-processed condition. Only a few dislocations can be found in the Mo phase. The observed dislocation distribution indicates that the Mo rods deform locally, only within the crack plane. On the other hand, the NiAl matrix phase has a very broad plastic zone as evidenced by the high dislocation density outside of the crack plane. The dislocation Burgers vector was determined to be  $\langle 100 \rangle$  in the NiAl matrix and  $\langle 111 \rangle$  in the Mo phase [16].

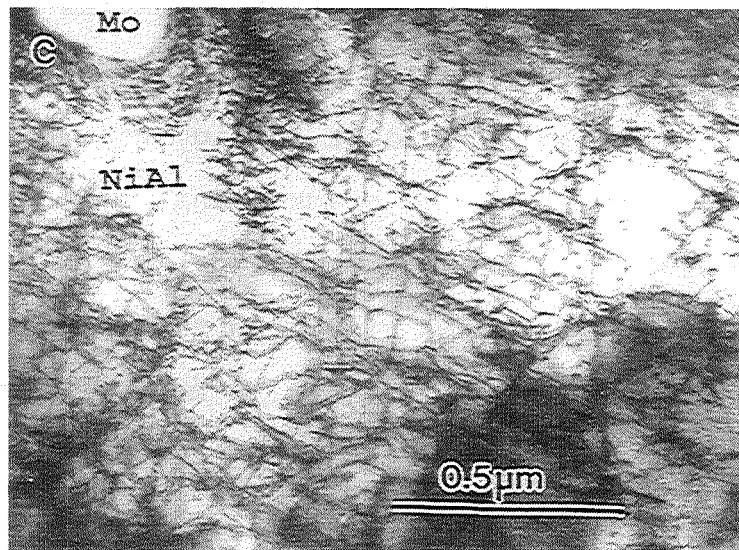
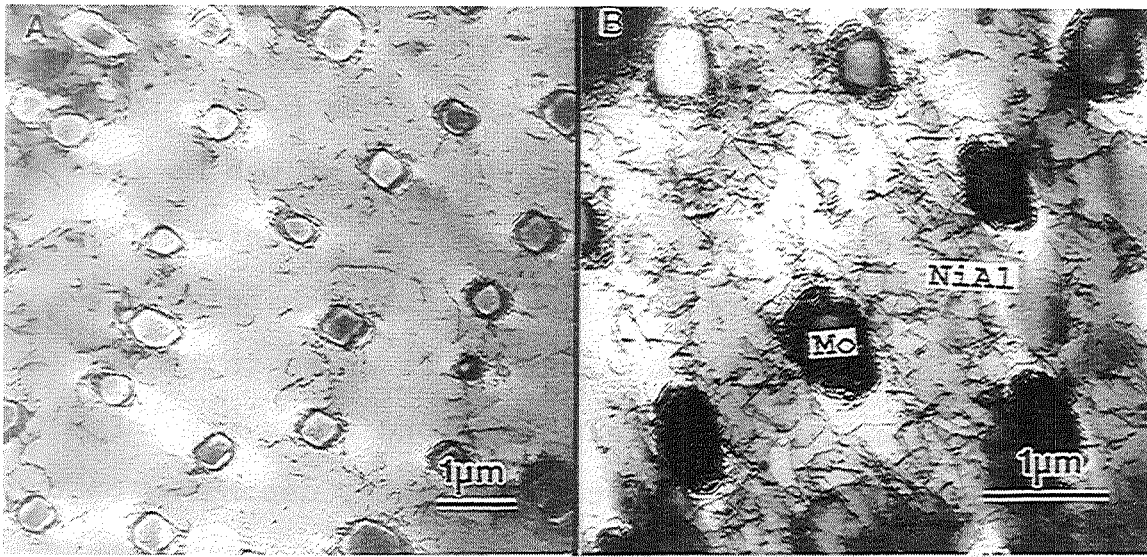


**Figure 65:** (TEM) Typical transverse microstructure of NiAl(0.1Zr)-9Mo showing dislocations in the NiAl matrix. a) in the as-processed condition and b) after 4-point bend testing.

Fractographs of the NiAl-9Mo alloy are shown in Fig. 66. Failure of the Mo rods occurs by partially constrained ductile rupture. Necking of the Mo rods is evidence of an active crack bridging mechanism (Fig. 66(a & b)). In isolated regions considerable debonding between the matrix and the rods has occurred as shown in Fig. 66(c & d). More typically, the extent of debonding is estimated to be at least one fiber diameter in length, depending on the orientation of the fiber relative to the crack path. Therefore, debonding as a mechanism does not contribute significantly to the toughness enhancement of the composite. Further evidence of ductility in the Mo rods is shown by the partially extracted and bent rod in Fig. 66 (d).

Crack trapping is evident in Fig. 66(e-g). This is shown by the bowing of the crack front markings between fibers in the crack growth direction. Crack trapping can also be identified by the ridges in the matrix observed as tails associated with each fiber in many of the fractographs shown in Fig. 66. Consistent with the crack bridging and trapping mechanisms, deformation of the Mo rods occurs only in the immediate region of the matrix cracks. Thus, the TEM sections do not contain the highly deformed regions of the Mo rods.

Furthermore, a high dislocation density is observed in the NiAl phase, which is indicative of enhanced plasticity

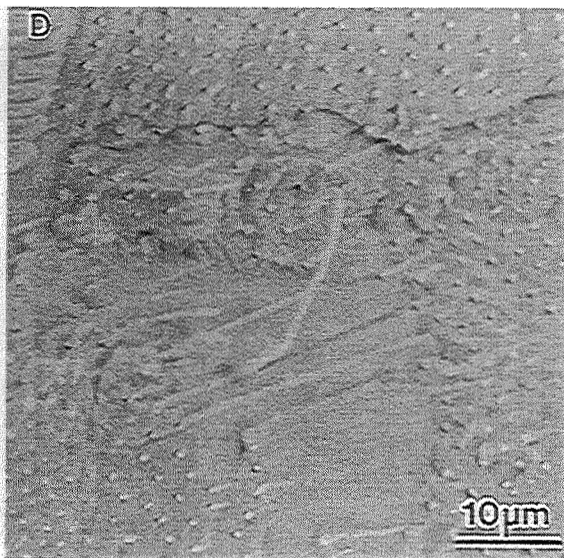
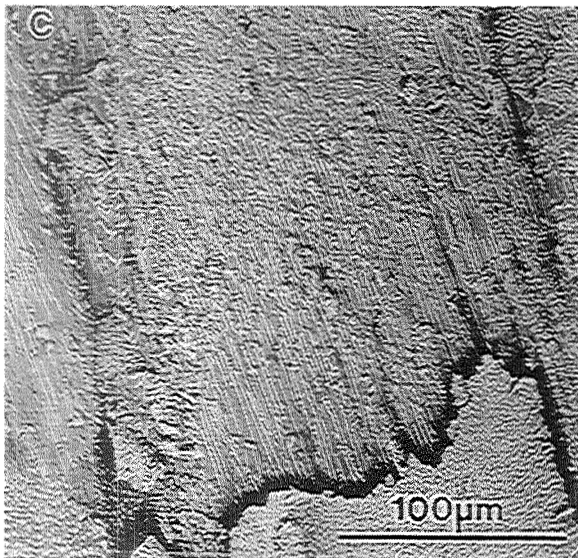
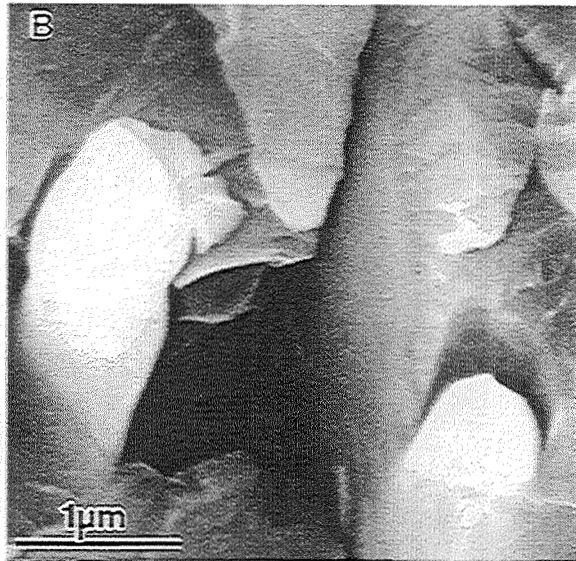
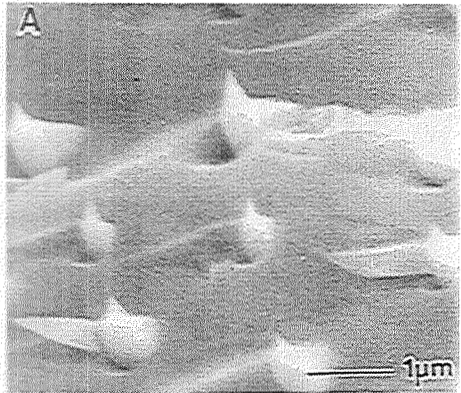


**Figure 66:** (SEM) The fracture surface of NiAl(0.1Zr)-9Mo. Shown are crack bridging in a-g, crack trapping in a,e-g, and debonding between the Mo rods and the NiAl matrix in a-g.

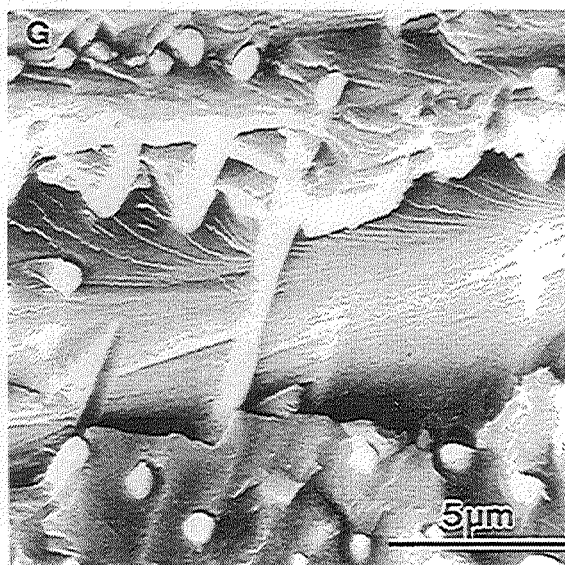
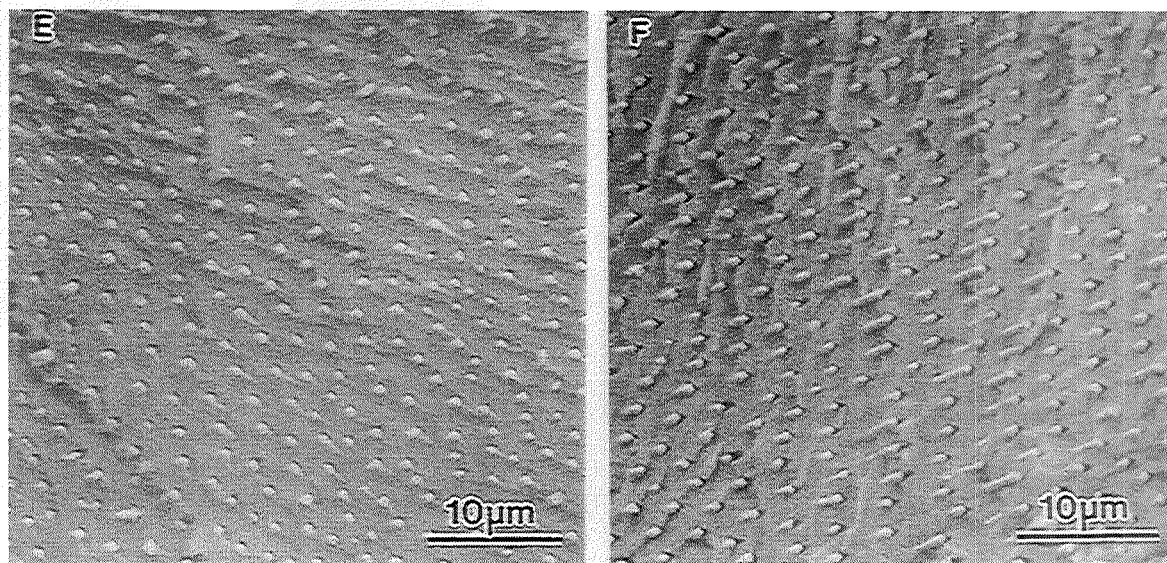


Figure 66 continued.



of the normally brittle matrix. Comparison between Fig. 65(a) and Fig. 65(b & c) illustrates the increase in dislocation density resulting from the bend test. Thus, in addition to crack trapping and bridging mechanisms, slip within the NiAl phase probably contributes to the overall toughness of the NiAl-Mo eutectic.

#### 4.1.2 NiAl-9Mo Eutectic

The mechanisms involved in failure of the NiAl-9Mo eutectic alloy are the same as for the Zr-doped alloy. Both crack bridging and trapping are observed, Fig. 67(a-c). The lower fracture toughness values measured for the Zr-free alloy result primarily from the lack of microstructural homogeneity. The volume fraction of Mo-rods within a eutectic colony is the same for both alloys. However, the degree of necking appears to differ slightly between the eutectic-based alloys. The rods in the NiAl-9Mo alloy neck down to a finer point, Fig. 67(c). The debonding characteristics are essentially the same. The observed failure indicates an increase in the elongation of the rods, but the work of rupture does not necessarily follow directly. Additions of 0.1 at% Zr and 0.5 at% Ti to Mo are used to improve the strength and ductility of commercially pure Mo [17]. Therefore, the Mo rods in the Zr-doped alloy

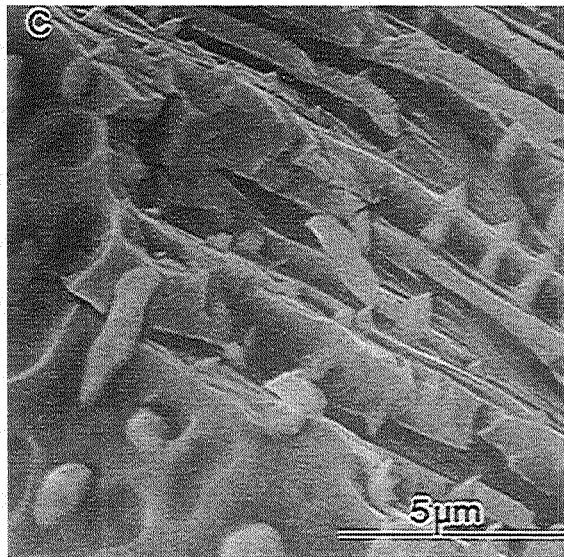
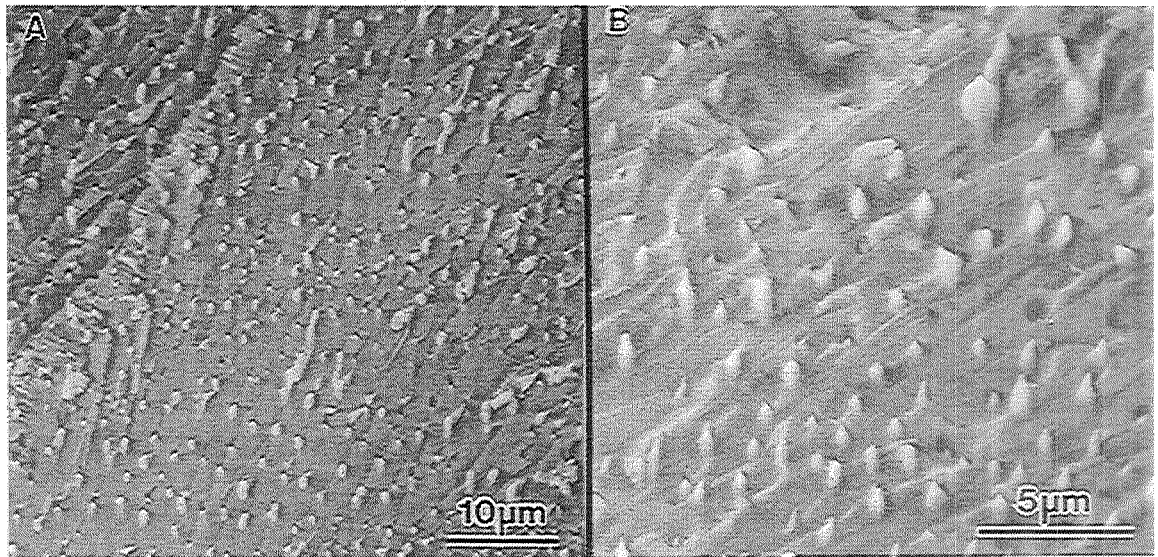


**Figure 67:** (SEM) The fracture surface of NiAl-9Mo. Shown are crack trapping in a-c, crack bridging in b and c, and debonding between the phases in b and c.

may require more energy to rupture because of a higher yield strength with only a slight decrease in elongation.

The distribution of the Mo rods is not as uniform in the NiAl-9Mo ingot. In addition, failure by ductile shearing is observed (Fig. 68(a-c)). In these regions, mixed mode fracture alters the loading conditions on the crack bridging fibers. Knowledge of the shear deformation behavior of the Mo rods is required to determine the contribution to the fracture toughness. Such a contribution is expected to be less than that of tensile rupture for the same ligaments, because the shear modulus is roughly one third the tensile modulus and typically the shear strength is less than the tensile strength.

#### 4.1.3 NiAl(0.1Zr)-12Mo and NiAl(0.1Zr)-15Mo

Within the eutectic colonies, the hypereutectic alloys contain the same volume fraction of Mo phase. The excess Mo is dumped in banded or inter-colony regions where the coupled growth is lost. Hence, under the imposed growth conditions, the volume of material having the preferred fiber reinforcement morphology decreases as the composition deviates further from eutectic. The failure of the eutectic colonies is the same as the NiAl(0.1Zr)-9Mo eutectic alloy. The blocky inter-cellular regions fail primarily by cleavage in the NiAl phase and debonding along the NiAl-Mo

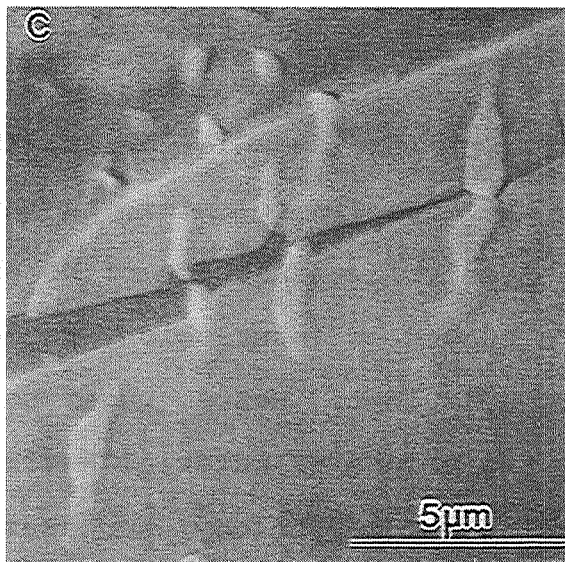
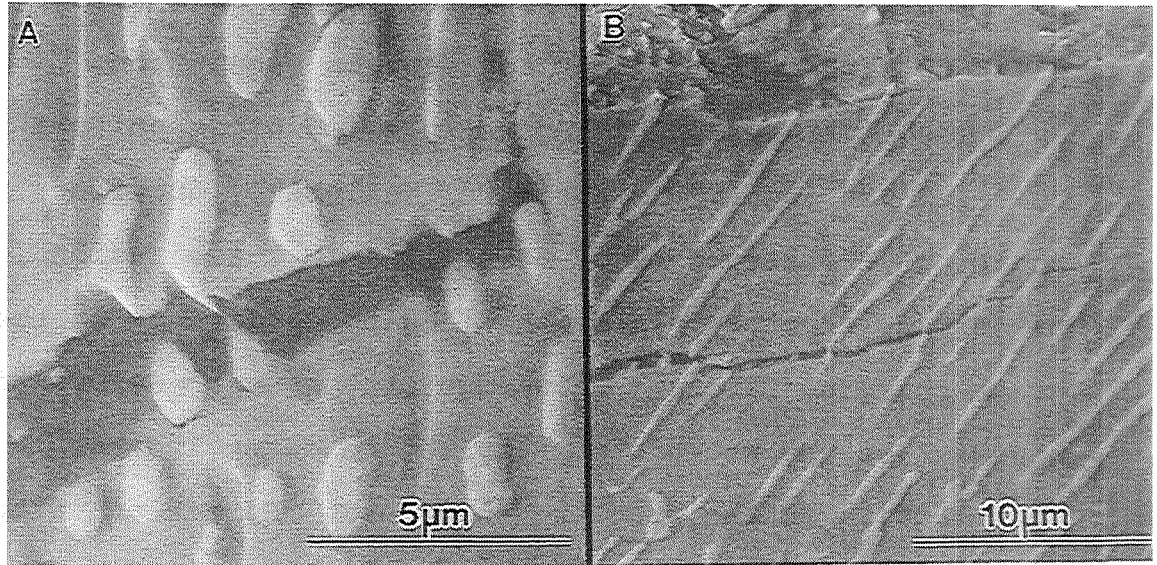


**Figure 68:** (SEM) Failure by combined axial extension and shearing of the Mo rods. Such failures are evident in some areas and reduce the energy required to rupture the Mo rods. a) within the specimen, b and c) at the specimen surface.

interfaces. Mode II or III type failures are also observed in NiAl(0.1Zr)-12Mo as in the NiAl-9Mo alloy.

#### 4.1.4 Summary of NiAl-Mo Alloys

The microstructure of the ingot has the largest effect on the mechanical properties. Most importantly, if the notch coincides with a banded region, the measured fracture toughness is decreased by more than 50%. The fracture in the banded regions is essentially cleavage of the NiAl matrix with some debonding along the interface between NiAl and the blocky Mo phase. Contribution from crack trapping or bridging within these regions is negligible. On the other hand, all of the NiAl-Mo alloys contain regions of coupled growth, i.e., aligned Mo rods within a NiAl matrix. These regions all exhibit evidence that crack trapping and bridging mechanisms contribute to the fracture behavior. In addition, the TEM analysis of NiAl(0.1Zr)-9Mo indicates an increase in matrix plasticity. Although no direct evidence of slip transfer was observed, the increase in dislocation density in the matrix suggests an effect due to the presence of the Mo rods. Since this intrinsic mechanism is associated with the interfaces between the phases it is not expected to contribute significantly to the fracture toughness or ductility in the banded regions.

#### 4.2 NiAl-40V Eutectic

The volume fractions of the NiAl and V phases are nearly equal. Figures 69(a-c) were taken far from the fracture surface of a tested sample. The dislocation density for the NiAl phase is much greater than that of the V-phase. In fact, very few dislocations were observed in the V-phase. For two phase NiAl-V alloys, the strength of the V solid solution is greater than that of the NiAl solid solution [18]. Hence, the NiAl-phase deforms before the V-phase. Figures 69(b) and 69(c) show the high density and uniformly distributed dislocation tangles, loops and fragments in the NiAl phase. This indicates that the NiAl-phase undergoes significant plastic deformation before any significant flow occurs in the V-phase. This would suggest that a significant portion of the fracture toughness in the NiAl-V system may result from intrinsic toughening of the NiAl due to enhanced flow processes.

Figure 70 is a TEM micrograph taken very near the fracture surface and shows uniformly distributed dislocation tangles in the NiAl phase but also coarse slip bands in the continuous V phase. The overall dislocation density in the NiAl phase is not increased much as compared to the dislocation density in the NiAl away from the crack plane (Fig. 69). This suggests that the NiAl phase has work hardened nearly to the point that deformation of the V phase can take place at a lower stress than the hardened NiAl.

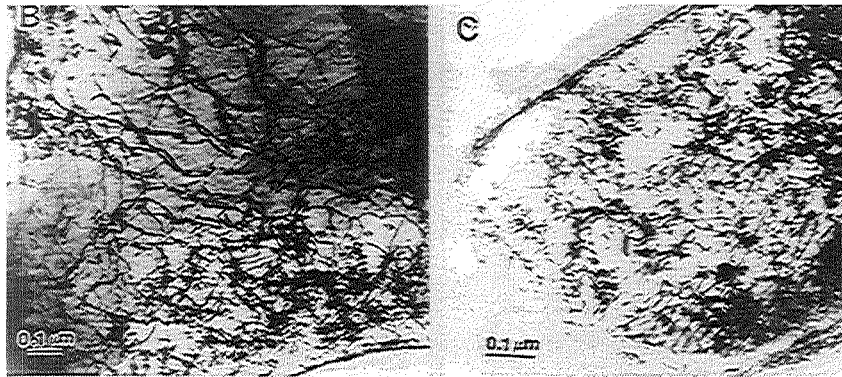
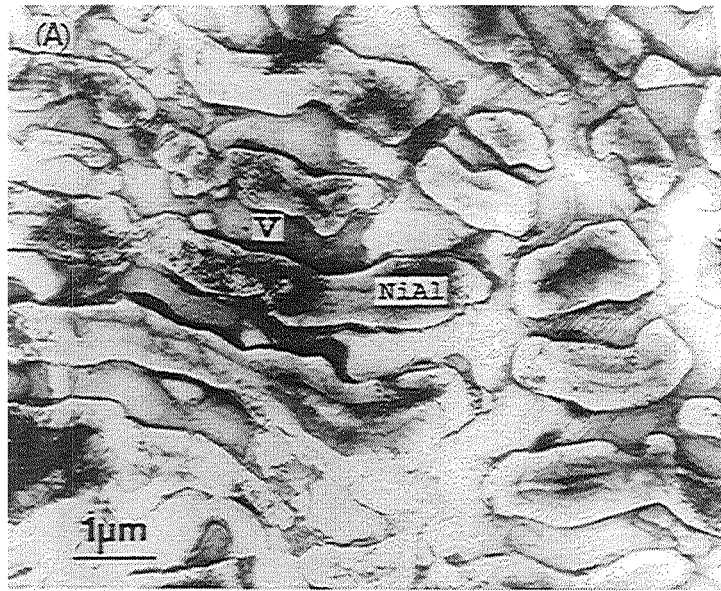


**Figure 69:** (TEM) As-processed NiAl-40V. a) NiAl lamellae in a continuous V matrix, b and c) the dislocation distribution in the NiAl phase.

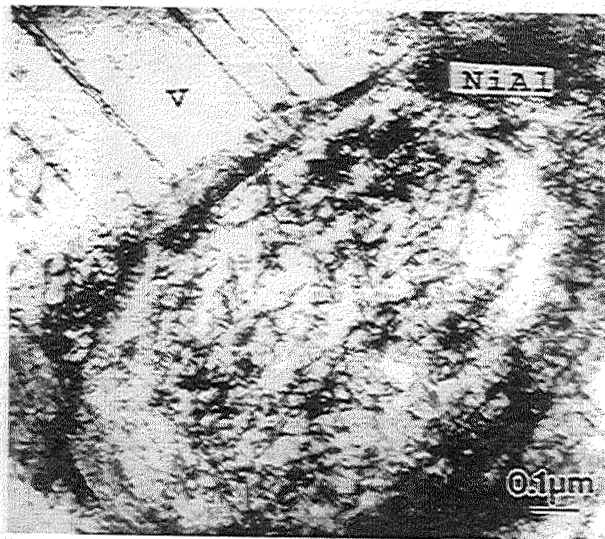


**Figure 70:** (TEM) Uniform dislocation tangles in the NiAl and coarse slip bands in the V phase in NiAl-40V after bend testing.



Once deformation of the V phase has been initiated, stress concentrations are generated at the interface between the phases. Continued deformation of the composite results in fracture of the NiAl. Figure 71 shows the various types of dislocation distributions observed within the V phase. These are coarse slip bands (Fig. 71(a)), dislocation pile ups (Fig. 71(b)) and duplex slip (Fig. 71(c)). Coarse slip bands are the main method of deformation in the V phase. Such slip bands are observed in both the as-processed condition and after bend testing, but more are found near the fracture surface. The fact that the V deforms in highly localized regions suggests that severe stress concentrations will develop wherever these regions intersect a boundary between phases.

Although the high dislocation density in NiAl indicates high stress at the interface, dislocation slip transfer between the two phases was not directly observed. Detailed observation of the interface boundary between the V-phase and NiAl phase was not successful because the interface is not coherent and is highly stressed. Generation of coarse slip bands in the V-phase is dictated by development of stress concentrations occurring at local regions of the interface, Fig. 72.

Shown in Fig. 73 are SEM backscattered electron images of secondary cracks in NiAl-40V. Both crack bridging and

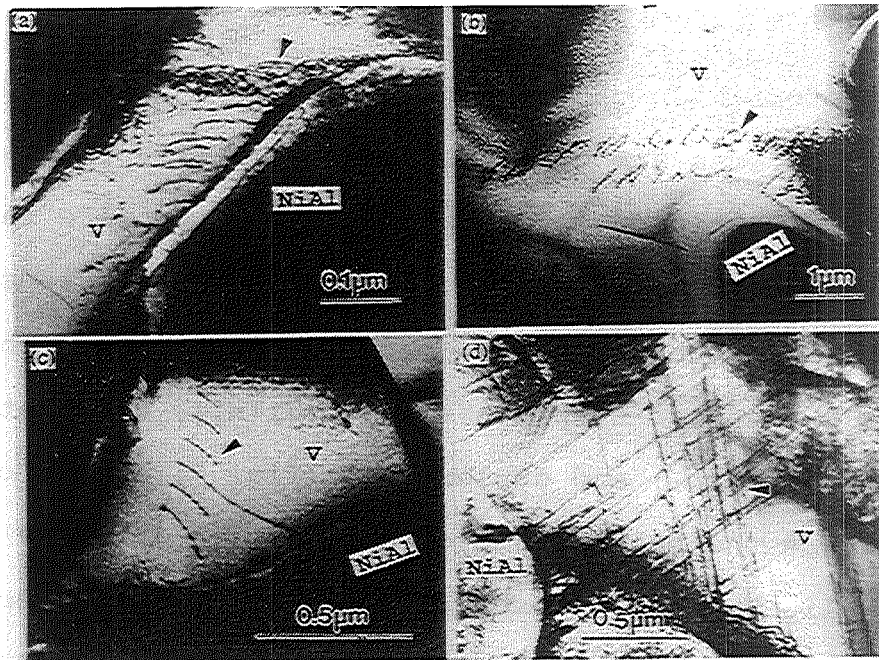


**Figure 71:** Types of dislocation distribution in the V-matrix of NiAl-40V. a) coarse slip bands, b and c) dislocation pile up, and d) duplex slip (see arrow).

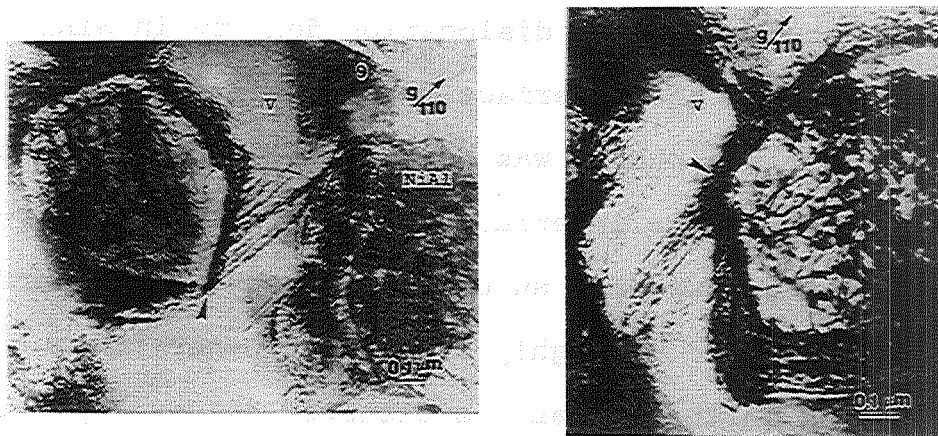


**Figure 72:** (TEM) Micrographs taken near the fracture surface of a NiAl-40V bend specimen. Shown is the dislocation distribution on both sides of the phase boundary (see arrow). Dislocation tangles in the NiAl and coarse slip bands in the V phase.

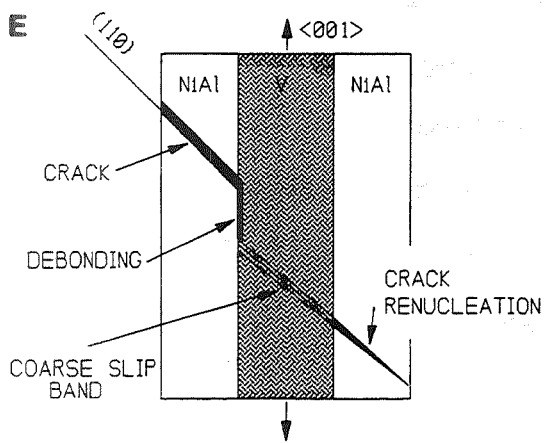
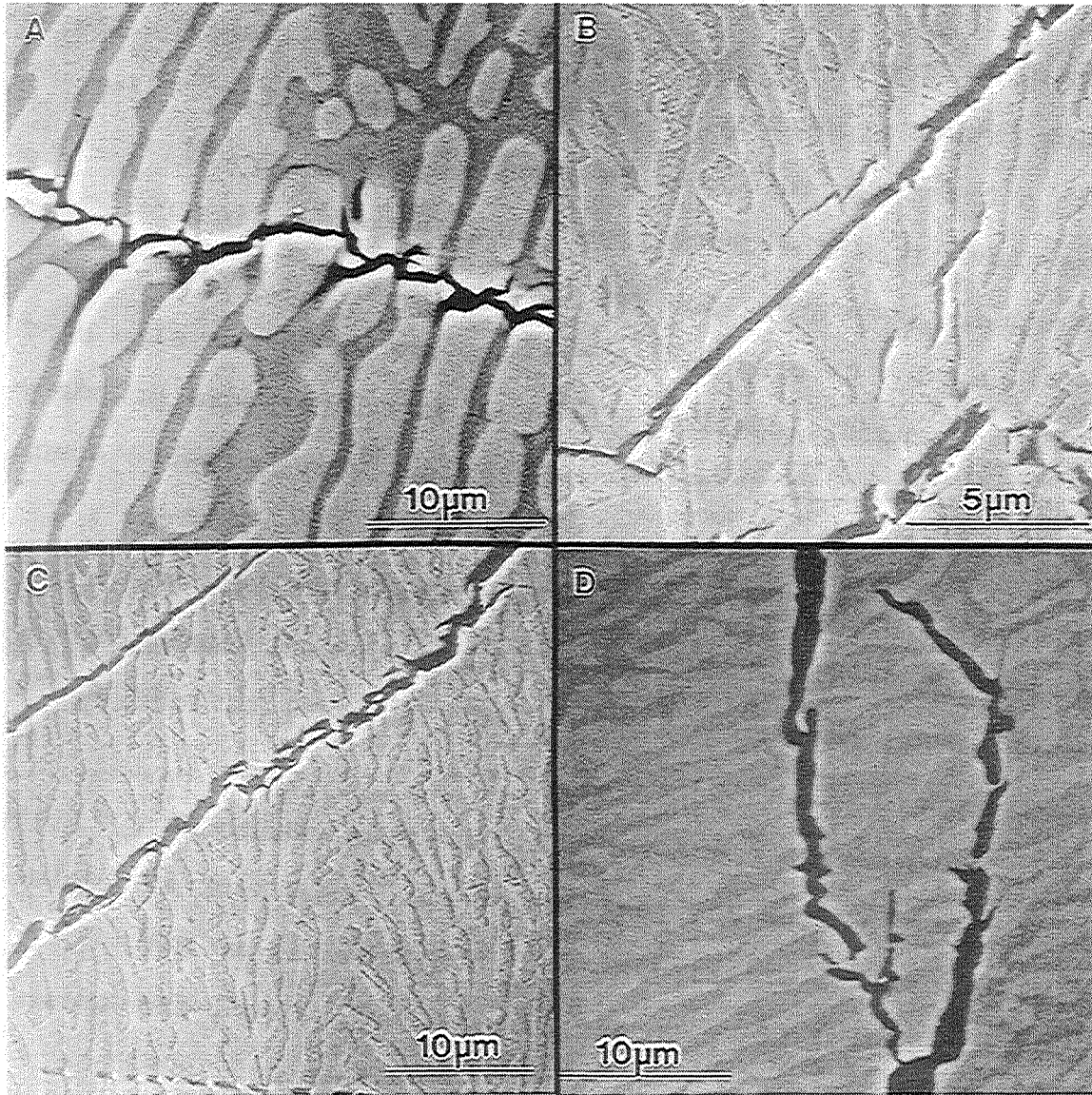


**Figure 73:** (SEM-4QBS) Secondary cracking in NiAl-40V observed on the surface of as-polished bend specimens showing evidence of crack bridging and crack renucleation.

renucleation mechanisms are evident in Figs. 73(a-d). The crack growth process is shown schematically in Fig. 73(e). Once a crack has initiated in the NiAl phase, it will propagate until the crack front intersects the NiAl/V interphase boundary. The crack front can then be blunted by the V phase. Deformation of the V phase by coarse slip band formation and dislocation pile up at the interphase boundary may then result in stress concentrations which promote crack renucleation in the adjacent NiAl phase. The state of stress at the NiAl/V interface is complex due to the anisotropy of NiAl, differences in the thermal expansion coefficients between the phases, and the applied loading conditions.

The cleavage plane for NiAl is  $\{110\}$ , which is a likely slip plane for the BCC vanadium phase. With such a complex state of stress existing at the interface, it is not unlikely that  $\{110\}$  planes will have both normal and shear stress components of considerable magnitude. A possible failure mechanism for the composite is localized shearing of the V phase on a  $\{110\}$  plane leading to cleavage of the NiAl phase on a  $\{110\}$  plane. The difference in the ratio of the critical resolved shear stress and the critical normal stress for cleavage between the phases may create the difference in failure mechanism of the individual components.

A crack bridging mechanism is also shown in Figure 73. Bridging lamellae of the V phase are visible as shown by the arrows in Fig. 73(c & d). Once the crack has renucleated in the adjacent NiAl lamella, the plastic work needed to deform the bridging V phase provides a resistance to crack growth, further increasing the toughness of the composite.

Figures 74(a-d) are fractographs of the NiAl-40V eutectic alloy. There is limited evidence of shear ligament formation, Fig. 74(a) (see arrow). Knife edge necking is not observed due to localized shearing of the V phase. Instead, the crack path appears to step from one layer to another with significant debonding between the phases, Fig. 74(a-d).

#### 4.3 NiAl-15Zr-15V

On a macroscopic scale, the fracture surface of the NiAl-15Zr-15V eutectic alloy is very uniform. The region shown in Fig. 75(a) contains well aligned lamellae of NiAl and Ni<sub>2</sub>AlZr with ZrV<sub>2</sub> dispersed along the boundary. Fracture generally occurs in the notch direction, i.e., 90° to the specimen axis. In this region, the microstructure is in a crack arrestor orientation and should therefore provide the maximum contribution to fracture toughness. However, all three phases fail by cleavage. The observed fracture surface reflects the fact that the cleavage planes of each

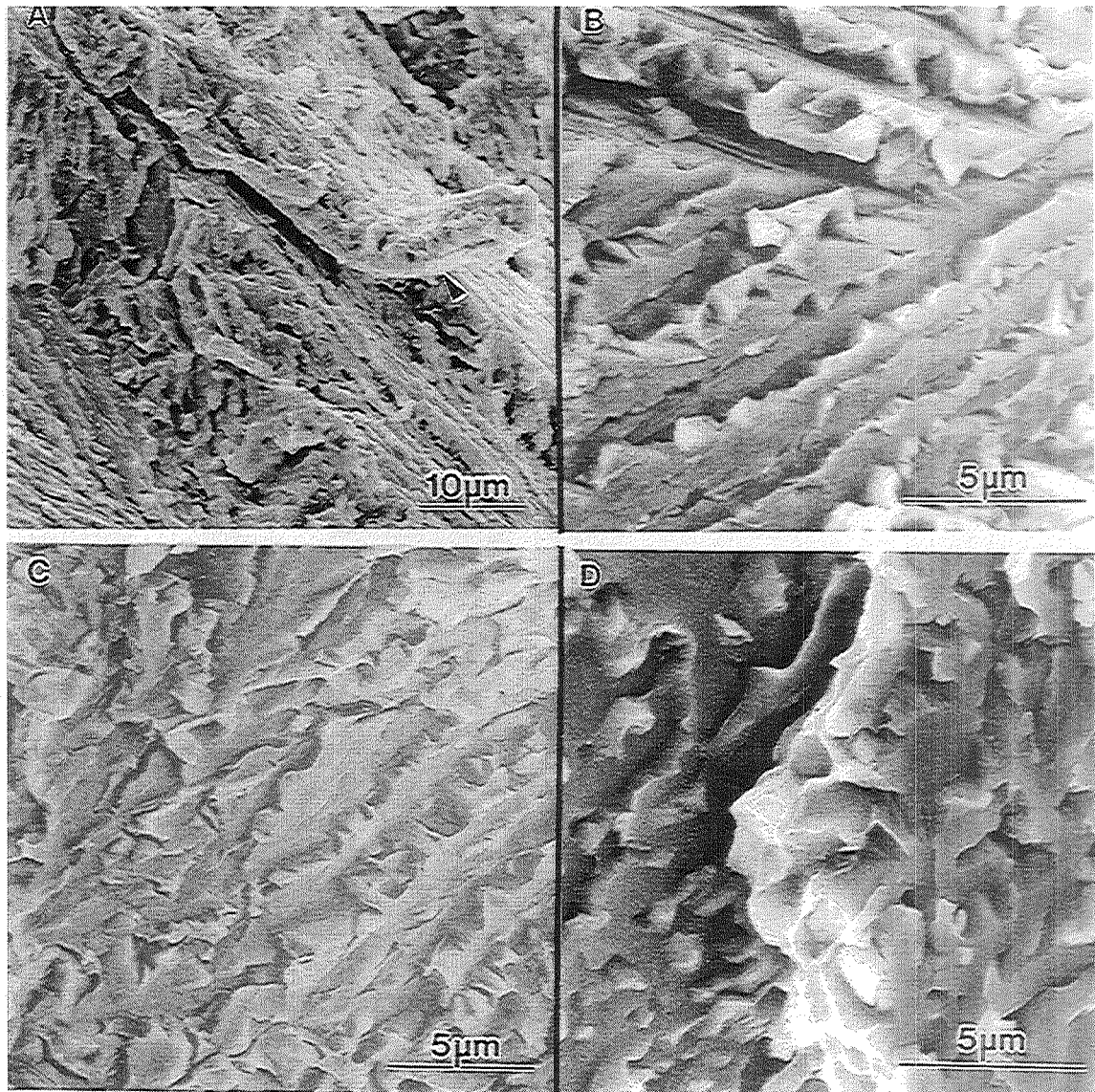


**Figure 74:** (SEM-4QBS) Fractographs taken from NiAl-40V bend specimens. Shown are a) limited occurrence of shear ligament formation, b c, and d) more typical cleavage and debonding leading to steps on the fracture surface.

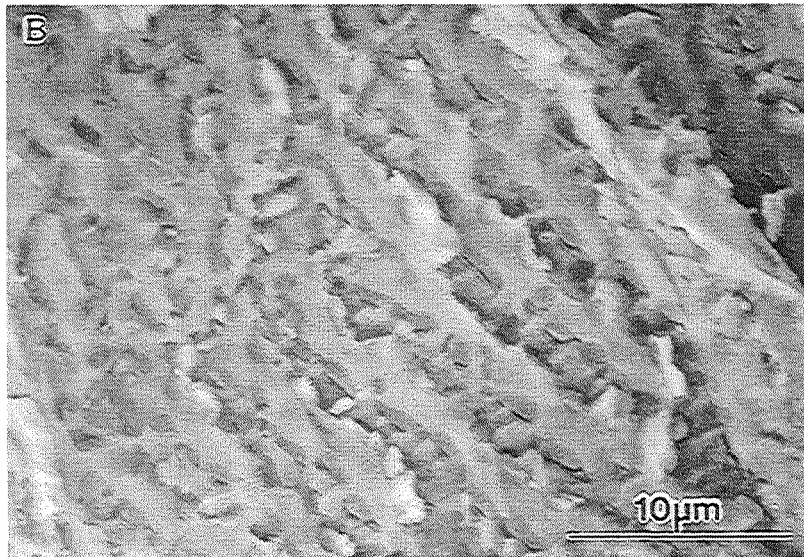
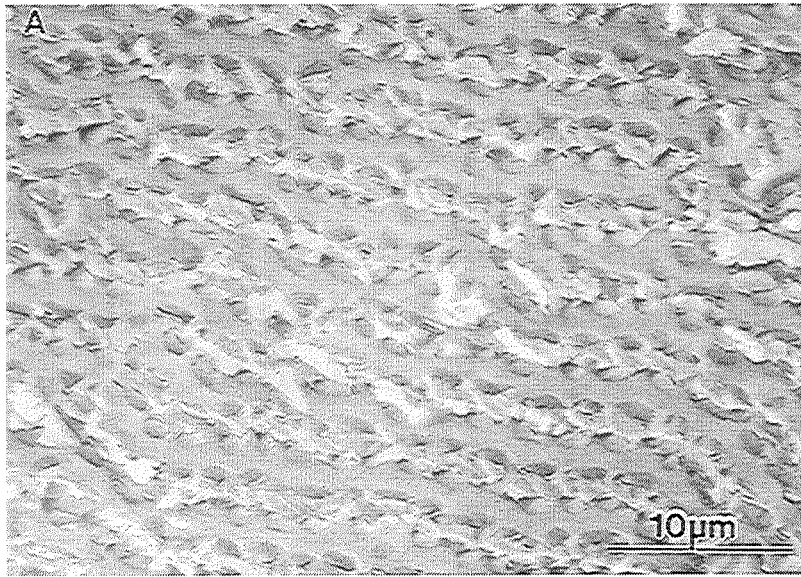


**Figure 75:** (SEM-4QBS) The fracture surface of NiAl-15Zr-15V. a) low and b) high magnification showing cleavage of all three phases.

phase are not coplanar. The combination of the individual cleavage planes and the microstructure results in very smooth cleavage of the NiAl and ZrV<sub>2</sub> phases while cleavage of the Ni<sub>2</sub>AlZr phase is on multiple planes. At the boundary between the ZrV<sub>2</sub> rods and the Ni<sub>2</sub>AlZr lamellae, some debonding is observed. Cracking within the ZrV<sub>2</sub> phase in the rod direction is also found in some regions, Fig. 75(b).

While crack bridging is not evident, the debonding, cracking of the ZrV<sub>2</sub> rods, and multiple cleavage planes in Ni<sub>2</sub>AlZr require additional energy to form. Hence, a small increase in toughness may be attributed to the microstructure.

#### 4.4 NiAl-12Nb-36V

The fracture toughness of the NiAl-12Nb-36V alloy is also poor. The failure mode for each phase is predominantly transgranular cleavage, Fig. 76(a-c). Evidence of debonding is limited and secondary cracking within the individual phases is just as scarce. No evidence of crack bridging is observed. Large regions of the fracture surface are essentially featureless. The crack front propagates continuously from one phase to the next with river patterns present in one of the phases. The dendritic nature of the microstructure indicates a lack of coupled growth and the



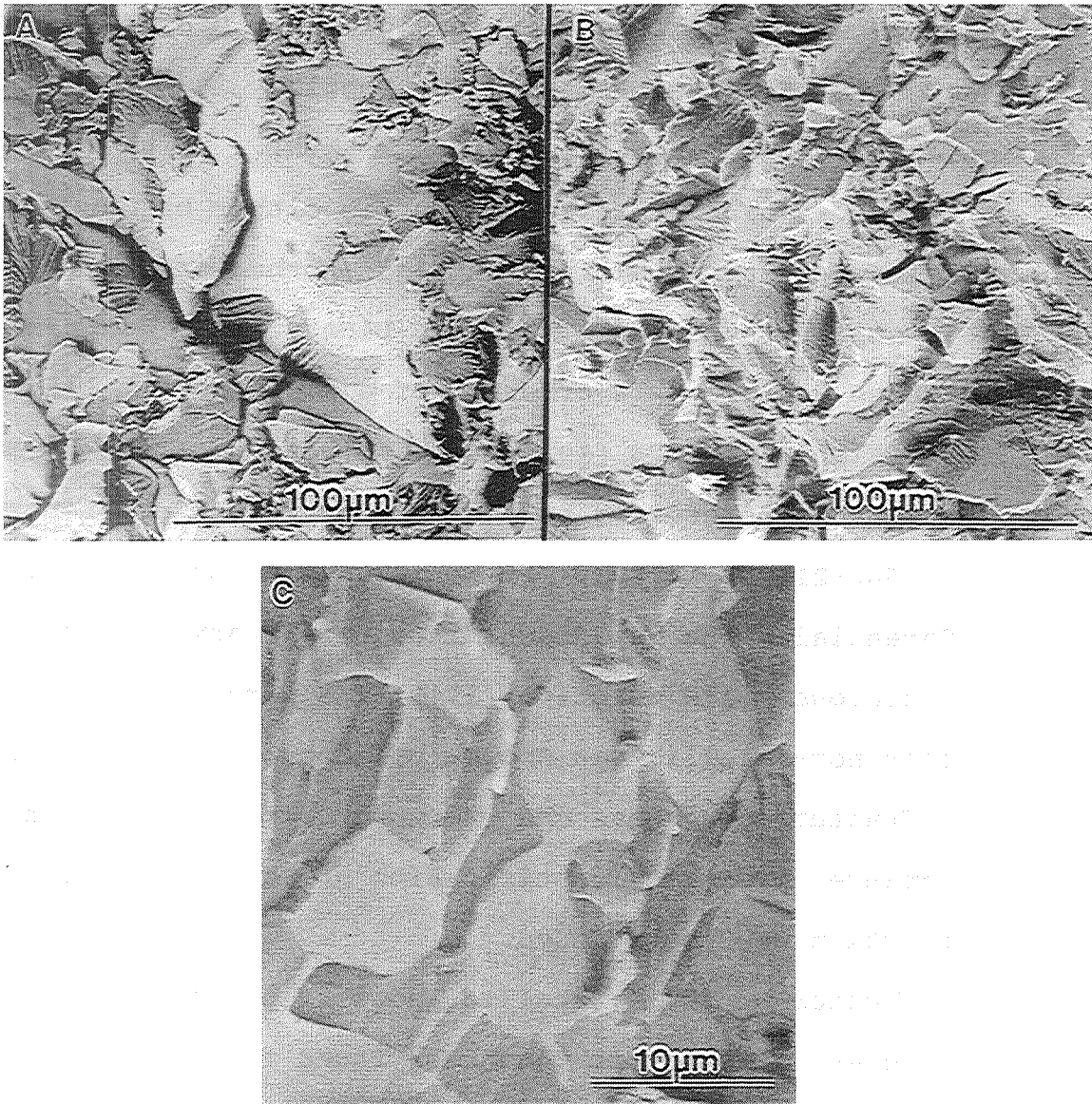


**Figure 76:** (SEM-4QBS) The fracture surface of NiAl-12Nb-36V. a) and b) show typical cleavage of all three phases. c) shows fracture that is typical of a well developed three-phase eutectic region.

possibility of significant deviations in the orientation of the grains. In regions where the cleavage planes are near that of the fracture surface, the topology is smooth. Other areas exhibit a more tortuous crack path.

The vanadium "solid solution" is either hardened beyond the cleavage strength or is instead another ordered intermetallic compound. The Ni-V binary phase diagram indicates the possible ordering of a sigma phase alloy of a composition near  $NiV_3$  [19]. The composition of the "V-solid solution" as determined by energy dispersive spectrometry is 60V-3.5Nb-21.9Ni-14.6Al. If Nb is assumed to substitute preferentially for vanadium (since the binary Nb-V system is a continuous solid solution [19]), the possible formation of another non-metallic can not be ruled out. In light of the poor fracture toughness and presumed lack of oxidation resistance, positive identification of this phase by X-ray diffraction was not pursued.

Whether or not a metallic phase is present, there is no improvement in fracture toughness found for this alloy as compared to HP-NiAl. Debonding is observed at some of the interfaces. However, the V-NiAlNb interface appears to be stronger because the fracture surface is often continuous across those boundaries. This is seen more clearly in the 3-phase region where debonding creates small steps in the plane of the fracture. Secondary cracking is observed to a

lesser extent. The fracture toughness is increased only slightly by the creation of the fracture surface area associated with the observed debonding and secondary cracking. The difference in morphology does not appear to affect the fracture toughness; both are  $6.8 \text{ MPa}\sqrt{\text{m}}$ .

#### 4.5 NiAl-Nb-Mo Alloys

The large volume fraction of Mo phase dendrites in the NiAl-Nb-Mo alloys is attractive because of their potential for increasing the fracture toughness. Unfortunately, the ductility of the Mo phase is lost upon addition of as little as 3 at% Nb to the nearly eutectic alloy, NiAl-10Mo.

##### 4.5.1 NiAl-13.6Nb-18Mo

Failure of the NiAl-13.6Nb-18Mo alloy occurs predominantly through the NiAl and NiAlNb phases. When the crack front encounters a Mo grain, it follows the phase boundary unless the grain has a very large aspect ratio, in which case the Mo cleaves, Fig. 77. Generally, the large single phase regions on the fracture surface are Mo-phase dendrites. The darkest phase of the two-phase regions is NiAl; the other is NiAlNb.

None of the crack bridging ligaments observed in this alloy exhibit significant ductility. However, crack

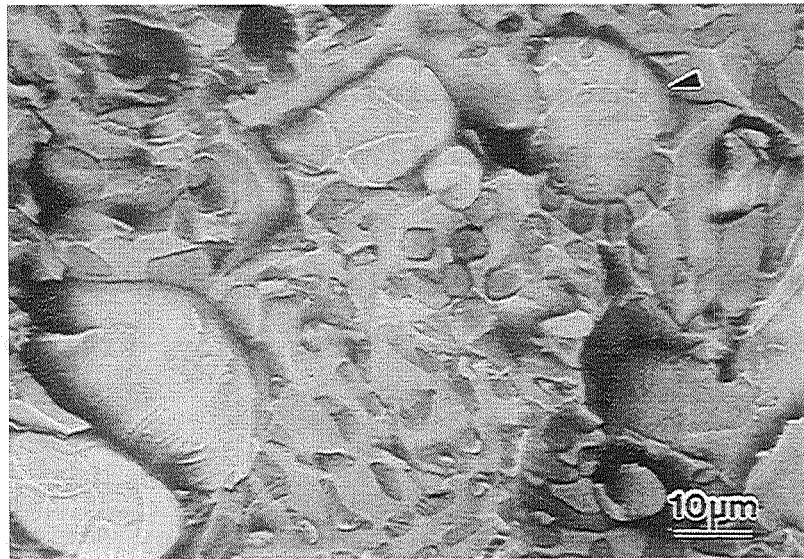


**Figure 77:** (SEM-4QBS) Fracture surface of NiAl-13.6Nb-18Mo. Shown are debonding at the Mo dendrites (see arrow) and cleavage of the NiAl-NiAlNb matrix.

bridging of the NiAlNb phase by NiAl is observed (Fig. 78), indicating a higher fracture toughness for the NiAl phase as compared to that of NiAlNb ( $\sim 2 \text{ MPa}\sqrt{\text{m}}$  [20]). In addition, debonding occurs between the NiAlNb and NiAl phases. A limited contribution to the fracture toughness results from crack splitting as shown in the low magnification micrograph, Fig. 79.

The presence of large Mo-solid solution dendrites does not enhance the fracture toughness of this alloy because they have very limited ductility. Fiber pull-out in this alloy is a possible alternative mechanism to ductile failure of the Mo, particularly since significant debonding between the Mo and the other phases is observed, Fig. 77. However, cleavage of the Mo appears to severely limit the occurrence of fiber pull-out as well. Only the rounded tips or cleaved cross-sections of the dendrites are observed on the fracture surface.

#### 4.5.2 NiAl-5Nb-10Mo

The primary difference in the NiAl-5Nb-10Mo alloy and NiAl-13.6Nb-18Mo is the lower volume fraction of NiAlNb and an increase in the presence of river patterns on the cleavage surfaces. Macroscopically, the crack plane lies near that of the notch. Microscopically, the fracture path follows the phase boundary between NiAl and Mo, Fig. 80.

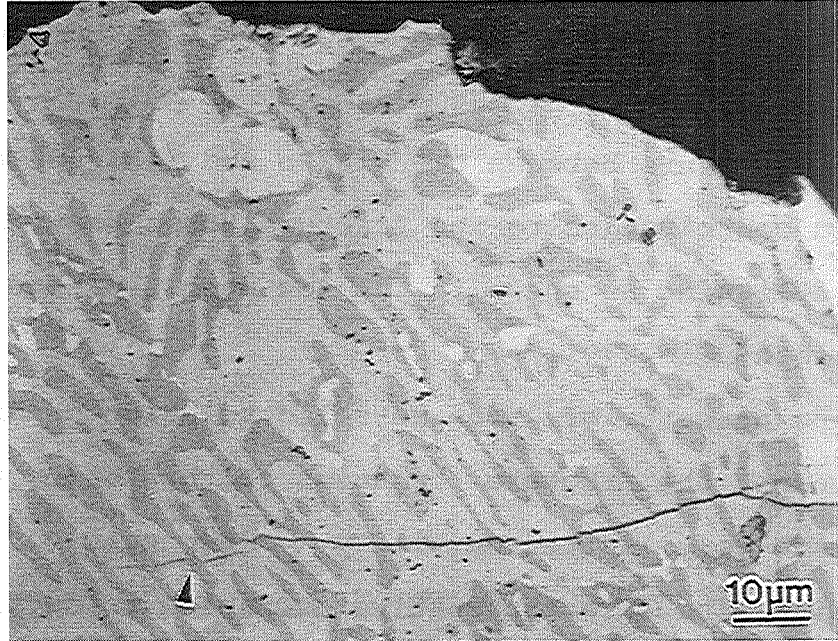


**Figure 78:** (OPT) Surface of NiAl-13.6Nb-18Mo bend specimen. Very limited evidence for crack bridging of the NiAlNb phase by NiAl and debonding at the NiAl and NiAlNb interface is observed.

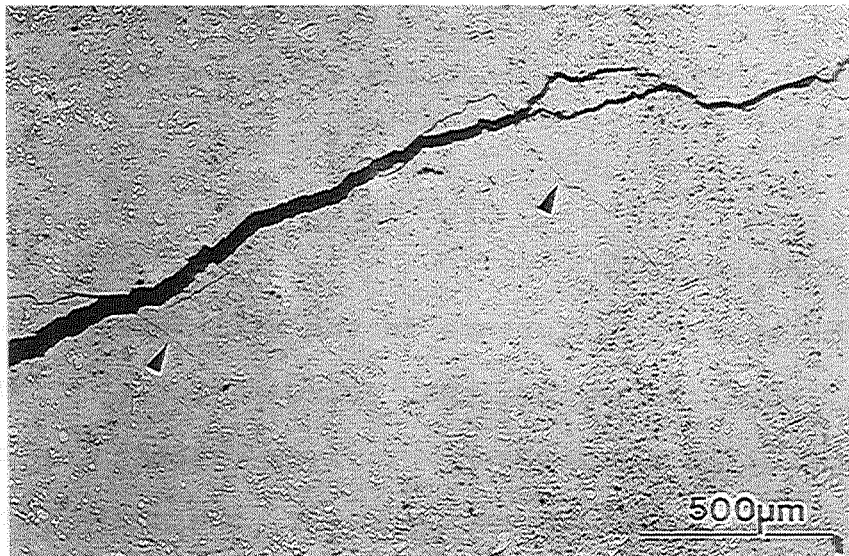


**Figure 79:** (OPT) Low magnification micrograph showing secondary cracking in NiAl-13.6Nb-18Mo (see arrows).

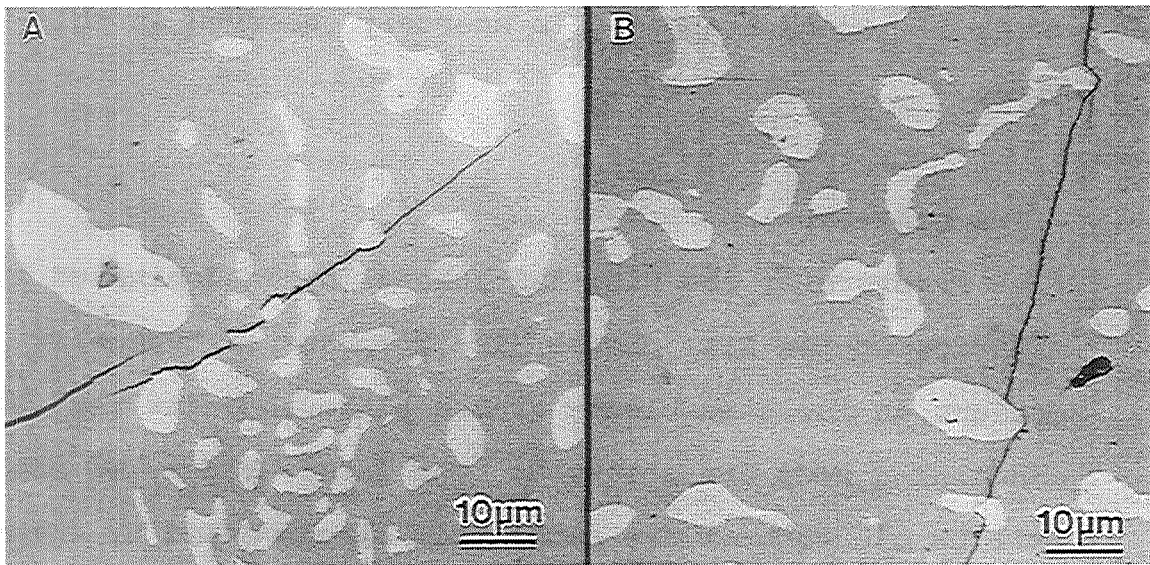


**Figure 80:** (OPT) Secondary crack at the surface of a NiAl-5Nb-10Mo bend specimen. a) debonding between the Mo and the NiAl matrix and b) fracture of the Mo when debonding is hindered by the morphology of the Mo phase.

The coupled growth of the NiAl-9Mo eutectic is lost with the addition of 5 atomic percent Nb as is the ductility of the Mo phase. As in the NiAl-13.6Nb-18Mo alloy, river patterns are observed in the NiAl phase, but the higher volume fraction makes them more prevalent, Fig. 81. Cleavage fracture is the dominant mechanism for all three phases. Again, no ductile ligaments are observed on the fracture surface. Crack branching is scarcely observed in this alloy.

#### 4.5.3 NiAl-3Nb-10Mo

Fracture of the NiAl-3Nb-10Mo alloy is dominated by cleavage of the NiAl phase. The Mo-phase is typically present as isolated blocky grains although a few regions containing rods are observed. The large, blocky Mo grains fail by cleavage or are completely circumvented by interface debonding, Fig. 82(a). The eutectic-like rods appear to be ductile and show limited debonding from the matrix as shown in Fig. 82(b). The NiAl fracture surface exhibits river patterns characteristic of cleavage. Again, the crack plane is very near that of the notch. Coupled growth between the NiAl and Mo phases is observed only in localized areas. The addition of only 3 atomic percent Nb is sufficient to both prevent coupled growth and embrittle the Mo phase.



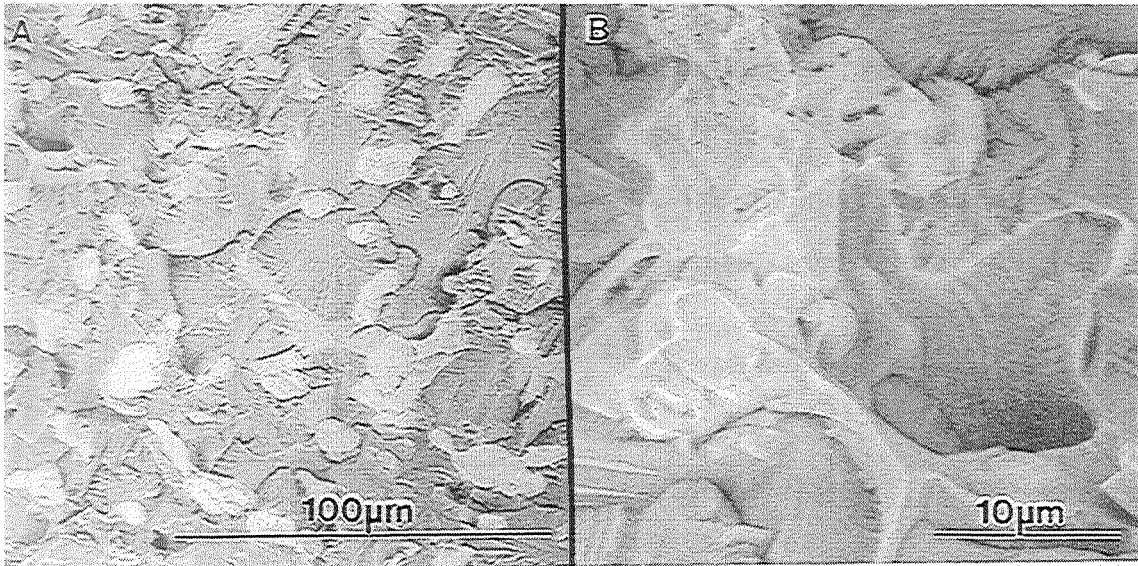


**Figure 81:** (SEM-4QBS) The fracture surface of NiAl-5Nb-10Mo. a) low and b) high magnification images showing typical cleavage, limited debonding, and secondary cracking.

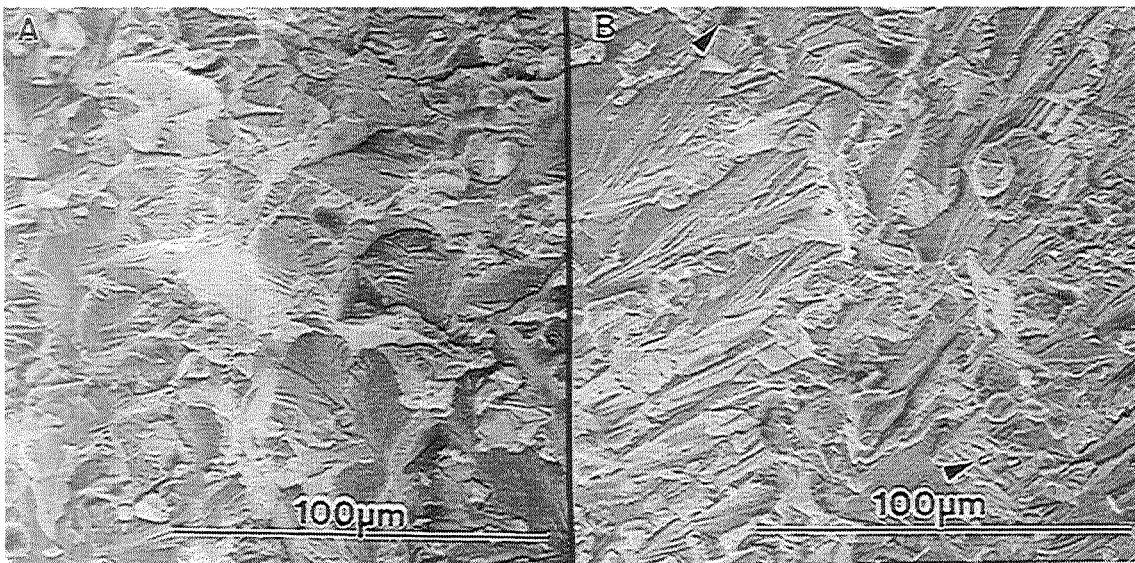


**Figure 82:** (SEM-4QBS) Fracture surfaces of NiAl-3Nb-10Mo. a) cleavage of all three phases and b) debonding between Mo and the NiAl matrix (see arrow) and limited evidence for ductility of the fine, eutectic-like Mo rods.

## 5. BRIDGING CONTRIBUTION TO FRACTURE TOUGHNESS

The work of rupture parameter,  $\chi$ , is an indication of the geometric constraint and the plastic flow characteristics of the ductile phase reinforcement [1,3,21]. A value of  $\chi$  is calculated using the small scale bridging (SSB) equation [3]:

$$\chi = \int_0^{\alpha^*} \frac{\sigma}{\sigma_0} d\alpha$$

$$\chi = \frac{1}{f\sigma_0 a_0} \left[ \frac{(1-\nu^2)K^2}{E} - \frac{(1-f)(1-\nu_m^2)K_m^2}{E_m} \right]$$

where:

- f = volume fraction of reinforcing phase
- $\sigma_0$  = yield strength of reinforcing phase (MPa)
- $a_0$  = radius of the reinforcing phase (nm)
- $\nu$  = Poisson's ratio
- K = fracture toughness ( $\text{MPa}\sqrt{\text{m}}$ )
- E = Young's modulus (GPa)
- $\alpha = \frac{u}{a_0}$  and  $\alpha^* = \frac{u^*}{a_0}$
- u = crack opening displacement

No subscript denotes composite values, the subscript m denotes matrix values, and the superscript \* indicates value at failure. The range of values observed by Ashby et al. for lead fibers constrained in a glass matrix is 1.6 (for highly constrained, near perfect interfacial bonding) to 6.5 (for low constraint, weak interfacial bonding) [1]. The property values used in the calculation of  $\chi$  are listed in

Table 18. Only the alloys characterized by the NANO-indentation technique are considered for SSB modeling. The NiAl-Nb-Mo composites show no evidence of ductility in the reinforcement phase. Therefore, only the NiAl-5Nb-10Mo alloy was characterized by NANO-indentation.

The choice of property values has considerable impact on the calculated work of rupture parameter. Ravichandran found a  $\chi$  of 4 to be representative of a wide variety of ductile phase reinforced composites, including NiAl-9Mo [21], but the parameters used in the calculation were significantly different than those in Table 18. Since Poisson's ratio was not available for many of the composites considered, plane stress conditions were used which results in an estimated error of only a few percent [21].

The reinforcement radius was determined by estimating the average area of a ductile phase region using scanning electron microscopy and calculating the radius of a cylinder with an equivalent cross-sectional area. In some cases, the reinforcement diameter varies across the ingot. For example, the average radius of the Mo rods in NiAl(0.1Zr)-9Mo varies between eutectic colonies by about a factor of two (from  $0.087\mu\text{m}$  to  $0.177\mu\text{m}$ ). As discussed previously, the variation in reinforcement diameter is associated with changes in the instantaneous growth rate and the dynamic

Table 18: Parameters used in the small scale bridging model.

Alloy (NiAl+)	$a_0$ (nm) *	Volume fraction	$\sigma_0$ (MPa)	K (MPa $\sqrt{m}$ )	$K_m$ (MPa $\sqrt{m}$ )	$E/(1-\nu^2)$ (GPa)	$E_m/(1-\nu_m^2)$ (GPa)
0.1Zr-9Mo	144	0.11	740	15.7	10	274	251
9Mo	144	0.11	740	7.0	10	274	251
34Cr	300	0.34	990	20.4	17	191	251
28Cr-6Mo**	1000	0.34	990	21.0	17	265	251
40V	500	0.5	646	32.7	8.5	246	254
5Nb-10Mo	16000	0.057	740	5.6	4	351	273
6Ta-33Cr	500	0.35	990	15.0	4	320	289
12Nb-36V	3750	0.22	646	6.8	4	144	302

\* equivalent radius of ductile phase

\*\* <111> growth direction, data from [24]

nature of the CELZ process. The lamellar spacing was used for NiAl-40V and NiAl-28Cr-6Mo.

The volume fraction was determined using digital image analysis in most cases. For low contrast alloys, the value was determined using the relative weight fraction of a photomicrograph cut along the phase boundaries.

For NiAl-40V and NiAl-34Cr, the yield strength values were estimated by a rule of mixtures calculation based on the room temperature yield strength of the composite. However, this approach does not give a reasonable value for the yield strength of the Mo phase in NiAl-9Mo alloys. In this case, the yield strength is taken to be that of pure Mo multiplied by a calculated factor of 1.68 to account for the elastic constraint. For plane strain conditions, experimentally determined values of the multiplication factor range from 1.5 to 2 [22].

The composite fracture toughness values were determined by four point bending as described in Part III, section 3. The fracture toughness of  $10 \text{ MPa}\sqrt{\text{m}}$  used for the matrix value of NiAl-9Mo alloys and  $17 \text{ MPa}\sqrt{\text{m}}$  for the NiAl-34Cr alloy are experimentally determined values of the crack initiation toughness [2]. Since the model concerns the work required to rupture the bridging ligaments in the wake of an advancing crack, the matrix toughness used for the ternary eutectic alloys is approximated by the fracture toughness of

a NiAl-Laves phase binary composite. The fracture toughness of NiAl-16.5Nb (a lamellar eutectic alloy) [23] is used for this purpose. A question arises regarding the treatment of the NiAl-40V alloy. The V phase is continuous in the microstructure, NiAl is not. However, since the volume fractions are same in this alloy and the bridging phase is observed experimentally to be the V phase, NiAl is taken as the matrix. The matrix toughness value is taken to be the average toughness of  $\langle 001 \rangle$  NiAl,  $8.5 \text{ MPa}\sqrt{\text{m}}$ .

The elastic modulus values of the composite and individual phases were measured using the NANO-indentation technique described in section 3. The actual data represents  $E/(1-\nu^2)$ ; therefore the value of Poisson's ratio is inherent to the data. Elastic modulus values may be extracted from this data provided Poisson's ratio is known.

Table 19 lists the results of the SSB model for the CELZ processed materials using the elastic property data taken from the microstructural components in-situ. Two approaches have been taken. First, a value of  $\chi$  is calculated based on the data in Table 18. Second,  $\chi$  is assumed to be 4, as a rough estimate [21], and the resulting fracture toughness calculated. Comparing the results, a large change in  $\chi$  is required to make a small change in the calculated fracture toughness. If the range of values determined by Ashby, Blunt, and Bannister for lead in glass

Table 19: SSB model results using data in Table 18.

Alloy	Calculated $\chi$	Calculated $K_q$ [ $\chi=4$ ] (MPa $\sqrt{m}$ )	Actual $K_q$ (MPa $\sqrt{m}$ )
NiAl(0.1Zr)-9Mo	46	10.5	15.7
NiAl-9Mo	-15	10.5	7.0
NiAl-34Cr	14	14.9	20.4
NiAl-28Cr-6Mo	3	23.6	21.0
NiAl-40V	26	13.9	32.7
NiAl-5Nb-10Mo	0	31.1	5.6
NiAl-6Ta-33Cr	4	15.3	15.0
NiAl-12Nb-36V	1	17.7	6.8

[1] are presumed to be universally applicable to the composites studied here, then values outside this range must indicate that other mechanisms contribute to the fracture toughness as well. If a value of  $\chi$  is chosen within this range, the magnitude of its affect on the calculated toughness depends on the volume fraction of ductile reinforcement. For example, if  $\chi$  is varied from 1 to 6, the respective variation in the calculated fracture toughness of NiAl(0.1Zr)-9Mo is 6.9 to 8.1 MPa $\sqrt{m}$ , or  $\pm 8\%$  of the average value. For NiAl-40V, the range is 8.1 to 16.8 MPa $\sqrt{m}$ , about  $\pm 35\%$  of the average value. In either case, variation of  $\chi$  within the range of 1 to 6 is not adequate to fit the model to the experimental results.

The discrepancy between the calculated  $\chi$  and the value of 4 which has been used to characterize the crack bridging behavior of several brittle matrix composites [21] may be explained by contributions of other toughening mechanisms not considered in this model. For instance, the significantly higher dislocation density observed in the matrix of the NiAl(0.1Zr)-9Mo eutectic alloy after testing suggests the possibility that enhanced plasticity of the NiAl may contribute to the increase in fracture toughness. In addition, there is evidence of an active crack trapping mechanism. In other alloys, crack splitting, renucleation, and debonding also contribute to varying extents.



## 6. DISCUSSION

Although the ductility of each reinforcement phase varies, all of the binary eutectic alloys show some degree of toughening due to crack bridging. A significant contribution from crack trapping is found for the binary rod eutectic alloys. For the lamellar eutectic alloys, crack renucleation and deflection mechanisms contribute to the composite fracture toughness.

The SSB model does not account for the measured increase in fracture toughness for nearly all of the alloys studied. The result for NiAl-28Cr-6Mo is fortuitous. Crack renucleation, crack deflection, and shear ligament mechanisms contribute to the toughness as well, but are not accounted for in the SSB model. Therefore, the SSB model overestimates the contribution due to crack bridging in this case. In most cases, however, the SSB model predicts an increase in toughness less than the observed increment, which allows for contributions from other mechanisms.

The presumption that the relative contribution to fracture toughness is proportional to the deviation of  $\chi$  from a specified range of values (1 to 6) is not supported by experimental observations. This fact indicates that microstructural inhomogeneities at the crack tip play a significant role in the fracture process. From analysis of the fracture surfaces, the contribution from crack bridging

increases in magnitude for the alloys as follows:

NiAl(0.1Zr)-9Mo, NiAl-9Mo, NiAl-34Cr, NiAl-28Cr-6Mo, NiAl-40V, NiAl-Cr-X, NiAl-Mo-X, and NiAl-V-X, where X is Ta, Nb, or Zr.

Nearly all of the three phase composites fail by transgranular cleavage. For alloys containing V as the intended metallic phase, the actual phase is either embrittled by solid solution hardening or is instead a brittle intermetallic phase. The ternary eutectic alloys containing Mo benefit from crack bridging by the Mo rods. However, the three phase NiAl-Nb-Mo alloys contain Mo formed by both dendritic and eutectic solidification. The dendritic Mo exhibits brittle behavior. The Mo rods formed by an eutectic reaction retain sufficient ductility to fail in a ductile manner. As expected, the Laves phases are brittle, but an appropriate choice of metallic reinforcement can offset their effect on the composite toughness (for example, NiAl-6Ta-28Cr). Of the ternary eutectics identified and tested in this work, all of the phases in each alloy fail by cleavage. Finally, only one alloy containing a Heusler-type phase has been identified. Unfortunately, it does not contain a metallic phase and shows very little resistance to oxidation. This type of ternary eutectic alloy deserves further effort to identify a

system containing both Heusler and disordered metallic phases in a matrix of NiAl.

The in-situ yield strength of the reinforcing phase and the actual matrix fracture toughness (initiation toughness) are not measured experimentally and are the two variables most likely to be in error. The ductility of the reinforcement phase does not appear explicitly in the SSB model used herein. The lack of ductility for any of the phases in the NiAl-5Nb-10Mo and NiAl-12Nb-36V alloys severely limits the crack bridging contribution as observed by fractography of the bend specimens.

The SSB model overestimates the crack bridging contribution for the three-phase composites which fail by cleavage of all three phases. When the crack path follows the phase boundaries, the SSB model also deviates from the experimental observations. The applicability of the model is questionable in such cases (NiAl-9Mo and NiAl-5Nb-10Mo). The negative work of rupture parameter for NiAl-9Mo indicates that such a crack path requires less work than propagation through the matrix phase. In this case, the measured fracture toughness is less than the matrix toughness, Table 18. The results for the NiAl-9Mo composite indicates that microstructural factors can dominate the behavior, i.e., the Mo is ductile, but the morphology is not optimal for fracture toughness enhancement.

The following table shows the results of the analysis of variance for the effect of the different factors on the response variable. The results are presented in the form of a table with the following columns: Factor, Sum of Squares, Degrees of Freedom, Mean Square, and F-value. The F-value is compared with the critical value from the F-distribution table to determine the significance of the effect.

**REFERENCES**

1. Smith, J. D., & Jones, M. A. (1998). The effect of temperature and humidity on the growth of *Escherichia coli*. *Journal of Food Science*, 69(2), 215-220.

2. Brown, L. R., & Green, P. Q. (2001). The influence of pH and salt concentration on the stability of a bacterial culture. *Food Microbiology*, 18(3), 235-240.

3. White, K. S., & Black, T. L. (2005). The effect of storage time and packaging material on the shelf life of a food product. *Food Preservation Science and Technology*, 27(4), 315-320.

4. Gray, R. M., & Lee, S. H. (2008). The impact of different preservatives on the growth of *Salmonella enteritidis*. *International Journal of Food Microbiology*, 121(1-2), 155-160.

5. Taylor, A. B., & Hall, C. D. (2010). The effect of different drying methods on the quality of a food product. *Food Research International*, 43(2), 185-190.

6. King, D. E., & Wilson, J. F. (2012). The influence of different packaging materials on the shelf life of a food product. *Food Packaging and Shelf Life*, 1(1), 1-5.

7. Adams, R. J., & Smith, J. P. (2015). The effect of different storage conditions on the stability of a food product. *Food Science and Technology*, 38(3), 215-220.

8. Baker, M. L., & Clark, S. R. (2018). The impact of different processing methods on the quality of a food product. *Food Engineering*, 1(1), 1-10.

9. Evans, G. H., & Roberts, L. A. (2020). The effect of different packaging materials on the shelf life of a food product. *Food Packaging and Shelf Life*, 24(1), 1-10.

10. Davis, K. M., & Miller, T. J. (2022). The influence of different preservatives on the growth of *Salmonella enteritidis*. *International Journal of Food Microbiology*, 178(1-2), 155-160.

- [1] M.F. Ashby, F.J. Blunt, and M. Bannister, *Acta Metall. Mater.*, 40(1992)2727.
- [2] F.E. Heredia, M.Y. He, G.E. Lucas, A.G. Evans, H.E. Déve, and D. Konitzer, *Acta Metall. Mater.*, 41(1993)505.
- [3] P.A. Mataga, *Acta Metall. Mater.*, 37(1989)3349.
- [4] N. Fares, *J. Appl. Mech.*, 56(1989)837.
- [5] H. Gao and J. Rice, *J. Appl. Mech.*, 56(1989)828.
- [6] K.S. Chan, *JOM*, 44(1992)30.
- [7] K.S. Chan, *Metall. Trans. A*, 23A(1992)183.
- [8] P.R. Subramanian, M.G. Mendiratta, D.B. Miracle, and D.M. Dimiduk, *MRS Symp. Proc.*, 194(1990)147.
- [9] R.D. Noebe and R. Gibala, *Scripta Metall.*, 20(1986)1635.
- [10] J.M. Brezeski, J.E. Hack, R. Darolia, and R.D. Field, *Mater. Sci. Eng.*, 170A(1993)11.
- [11] M.A. Morris, J.-F. Perez, and R. Darolia, *Philos. Mag. A*, 69(1994)507.
- [12] A. Misra, R.D. Noebe, and R. Gibala, in *MRS Symp. Proc.* 288(1994)483.
- [13] H.E. Cline, J.L. Walter, E. Lifshin, and R.R. Russel, *Metall. Trans.*, 2(1971)189.
- [14] K.S. Chan, *Met. Trans. A*, 22A(1991)2021.
- [15] W.C. Oliver and G.M. Pharr, *J. Mat. Res.*, 7(1992)1564.
- [16] X.F. Chen, S.M. Joslin, B.F. Oliver, and C.R. Brooks, *Scripta Metall. Mater.*, 29(1993)1439.
- [17] E. Tietz and W. Wilson, *Behavior and Properties of Refractory Metals*, Stanford University Press, (1965)334.
- [18] J.D. Cotton, M.J. Kaufman, and R.D. Noebe, *Scripta Metall. Mater.*, 25(1991)1827.
- [19] M. Hansen, *Constitution of Binary Alloys*, McGraw-Hill Book Co., (1985).

- [20] G. Sauthoff, Z. Metallkde, 81(1990)855.
- [21] K.S. Ravichandran, Scripta Metall. Mater.,  
26(1992)1389.
- [22] D. Broek, Elementary Engineering Fracture Mechanics,  
Martinus Nijhoff Publishers, Boston, MA (1986)115.
- [23] R. Reviere data
- [24] D. R. Johnson, NASA Contractor Report 195333, (1994).

## VITA

Steven Mark Joslin was born in [REDACTED] on [REDACTED]

[REDACTED] He received a Bachelor of Science degree in Metallurgical Engineering from The University of Tennessee, Knoxville (UTK) on March 16, 1984. He then worked for McDonnell Douglas Astronautics Co. in St. Louis, MO until returning to UTK in the Fall of 1986. He received a Master of Science degree in Metallurgical Engineering on December 15, 1989. His major advisor was Dr. K.H.G. Ashbee, Ivan Racheff Chair of Excellence. The thesis was entitled "The Feasibility of Rigid Die Bidimensional Compression for Consolidation of Metal Powders". He then joined High Temperature Materials group at UTK. His major advisor was Dr. B.F. Oliver. A Doctor of Philosophy degree was awarded on December 18, 1994. After completing the requirements for his Ph.D. degree, he received a Staff Engineer position at MEMC Electronic Materials Co. in St. Peters, MO.

# REPORT DOCUMENTATION PAGE

Form Approved  
OMB No. 0704-0188

Public reporting burden for this collection of information is estimated to average 1 hour per response, including the time for reviewing instructions, searching existing data sources, gathering and maintaining the data needed, and completing and reviewing the collection of information. Send comments regarding this burden estimate or any other aspect of this collection of information, including suggestions for reducing this burden, to Washington Headquarters Services, Directorate for Information Operations and Reports, 1215 Jefferson Davis Highway, Suite 1204, Arlington, VA 22202-4302, and to the Office of Management and Budget, Paperwork Reduction Project (0704-0188), Washington, DC 20503.

1. AGENCY USE ONLY (Leave blank)	2. REPORT DATE February 1995	3. REPORT TYPE AND DATES COVERED Final Contractor Report	
4. TITLE AND SUBTITLE NiAl and NiAl-Based Composites Directionally Solidified by a Containerless Zone Process		5. FUNDING NUMBERS  WU-505-63-52 G-NAG3-876	
6. AUTHOR(S)  Steven M. Joslin		7. PERFORMING ORGANIZATION NAME(S) AND ADDRESS(ES)  The University of Tennessee at Knoxville Knoxville, Tennessee 37916	
8. PERFORMING ORGANIZATION REPORT NUMBER  E-9422		9. SPONSORING/MONITORING AGENCY NAME(S) AND ADDRESS(ES)  National Aeronautics and Space Administration Lewis Research Center Cleveland, Ohio 44135-3191	
10. SPONSORING/MONITORING AGENCY REPORT NUMBER  NASA CR-195430		11. SUPPLEMENTARY NOTES This report was submitted as a dissertation in partial fulfillment of the requirements for the degree Doctor of Philosophy to the University of Tennessee, Knoxville, Tennessee. Project Manager, Ronald D. Noebe, Materials Division, NASA Lewis Research Center, organization code 5120, (216) 433-2093.	
12a. DISTRIBUTION/AVAILABILITY STATEMENT  Unclassified - Unlimited Subject Category 26  This publication is available from the NASA Center for Aerospace Information, (301) 621-0390.		12b. DISTRIBUTION CODE	
13. ABSTRACT (Maximum 200 words)  A containerless electromagnetically levitated zone (CELZ) process has been used to directionally solidify NiAl and NiAl-based composites. The CELZ processing results in single crystal NiAl (HP-NiAl) having higher purity than commercially pure NiAl grown by a modified Bridgman process (CP-NiAl). The mechanical properties, specifically fracture toughness and creep strength, of the HP-NiAl are superior to binary CP-NiAl and are used as a base-line for comparison with the composite materials subsequently studied. Two-phase composite materials (NiAl-based eutectic alloys) show improvement in room temperature fracture toughness and 1200 to 1400 K creep strength over that of binary HP-NiAl. Metallic phase reinforcements produce the greatest improvement in fracture toughness, while intermetallic reinforcement produces the largest improvement in high temperature strength. Three-phase eutectic alloys and composite materials were identified and directionally solidified with the intent to combine the improvements observed in the two-phase alloys into one alloy. The room temperature fracture toughness and high temperature strength (in air) serve as the basis for comparison between all of the alloys. Finally, the composite materials are discussed in terms of dominant fracture mechanism observed by fractography.			
14. SUBJECT TERMS  NiAl; Eutectic; Directional solidification processing; Microstructure; Fracture toughness			15. NUMBER OF PAGES 264
16. PRICE CODE A12			17. SECURITY CLASSIFICATION OF REPORT Unclassified
18. SECURITY CLASSIFICATION OF THIS PAGE Unclassified	19. SECURITY CLASSIFICATION OF ABSTRACT Unclassified	20. LIMITATION OF ABSTRACT	



**National Aeronautics and  
Space Administration**  
**Lewis Research Center**  
21000 Brookpark Rd.  
Cleveland, OH 44135-3191

**Official Business**  
**Penalty for Private Use \$300**

**POSTMASTER: If Undeliverable — Do Not Return**